UNIVERSITÀ DI PARMA

DEPARTMENT OF ENGINEERING AND ARCHITECTURE

Doctoral Research in Information and Technology
XXXVII Cycle

Isaac Yorke

INNOVATIVE PHOTONICS-BASED DEVICES AND MEASUREMENT TECHNIQUES FOR MODERN OPTICAL COMMUNICATIONS

DISSERTATION SUBMITTED FOR THE AWARD OF
DOCTOR OF RESEARCH

DECEMBER 2024

UNIVERSITÀ DI PARMA

Doctoral Research in Information Technology

XXXVII Cycle

INNOVATIVE PHOTONICS-BASED DEVICES AND MEASUREMENT TECHNIQUES FOR MODERN OPTICAL COMMUNICATIONS

Coordinator:

Prof. Marco Locatelli

Tutor:

Prof. Federica Poli

Researcher: *Isaac Yorke*

December 2024

Summary

List of Figures

List of Tables

Abstract

The high demand for faster, more efficient, and energy-conscious data transmission systems has fueled significant advancements in optical communication technologies. At the same time, the pressing need to address energy consumption in an energy-constrained world has become a critical priority in information and communication technology. In my PhD activities, I reviewed how photonic analog to digital converters (PADCs) can overcome the performance limitations of electronic analog to digital converters (EADCs). My focus was particularly on spectrally sliced PADC architectures, given their importance in coherent receivers. Additionally, I conducted a review of the energy consumption characteristics of these PADCs as well as numerical study on waveguides and couplers.

Aside the review works done on PADCs, and the numerical study of waveguides and couplers, the main objective of this thesis work is to demonstrate a new method of measuring dispersion in the case of a waveguide with chirped Bragg gratings. It is based on the fact that when coupling light into a waveguide using edge coupling, a fraction of the light will be reflected at the edge of the device and the rest will be transmitted. For this transmitted part of light, different frequencies will be reflected at different positions within the waveguide, due to the chirped Bragg gratings. The reflected light at the edge and within the waveguide will interfere to create a Michelson interferometric effect. By analyzing the combined reflected beams, the group delay can be calculated as the inverse of the spacing between the peaks, and the slope of the group delay is the dispersion of the device. An analytical model is also developed to calculate the dispersion of the device. It is important to note that the results ob-

tained with both the experimental measurements and the analytical approach are in good agreement with the designed dispersion value of the device. The approach proposed during my stay at the Department of Electrical and Photonics Engineering of DTU with Professor Galili's group is fast, relative to the time required for measuring dispersion with the established methods. Moreover, it is a reliable technique based on the step-by-step procedure adopted in data processing. Finally, it is an accurate method because the results obtained are in good agreement with the designed values. This approach can represent an alternative to the established method for measuring dispersion, and its development for further applications will be the object of future work.

Introduction

The relentless demand for faster, more efficient and energy-conscious data transmission systems have driven advances in optical communication technologies [1]. Simultaneously, the growing awareness of living in an energy-constrained world has elevated the importance of addressing energy consumption in information technology and communication systems. It has been demonstrated that enhancing energy efficiency in network elements will partly rely on advancements in the design and performance of underlying optical and electronic components, as well as on their effective deployment. Some of these advancements will naturally result from the ongoing improvements in the energy efficiency of complementary metal oxide semiconductor (CMOS) and other electronic component technologies. However, achieving further progress will require substantial innovation in both the design of individual network elements and the architectures of the networks in which they operate [2].
At the core of Photonic Integrated Circuit (PIC) technology are advanced material platforms and device architectures that harness the properties of light (photons) to process and transmit information. PICs use light to carry data, enabling significantly faster data transfer rates and increased bandwidth. This is due to light's higher frequency compared to electrical signals, allowing more information to be encoded in the same period [3]. Manipulating light for data transmission and processing also reduces energy consumption because photonic devices generally experience less resistive heating and other energy losses compared to electronic components [4]. This approach contrasts with Electronic Integrated Circuits (EICs), which manipulate electrical signals using semiconductor materials and faces limitations due to factors like

resistive losses and electromagnetic interference [3]. Table 1 summarizes the key distinctions between PICs and EICs, detailing their unique characteristics and common applications.

Table 1: PICs versus EICs; adapted from [3]

Aspect	PICs	EICs
Operational mechanism	Utilize photons (light) for signal transmission	Rely on electrons for signal transmission
Medium	Optical fibers, waveguides, and photonic crystals	Si or other semiconductor materials
Speed	Usually, higher speed	Limited by electron mobility and resistance
Energy efficiency	Generally, more energy-efficient	Subject to resistive losses and heat dissipation
Bandwidth	Higher bandwidth capabilities	Bandwidth limited by material properties
Signal loss	Lower signal loss over long distances	Signal loss over distance in conductors
Interference	Less susceptible to EM interference	Susceptible to EM interference
Integration density	Limited by photonic component sizes	Can achieve high integration densities
Overall cost	Typically, higher costs due to fabrication complexity	Lower cost due to mature manufacturing processes
Applications	Optical communication, computing, sensing, imaging	Computing, data processing, control systems

The three major integrated photonics platforms considered nowadays are Silicon Nitride (SiN), Indium Phosphide (InP), and Silicon Photonics (SiPh). InP is the only base material for integrated photonics that can produce light and can "conduct" it. This means InP is the only platform with the inherent ability to integrate active components, such as amplifiers and detectors. On the other hand, SiN is the only platform suitable for visible-light applications, such as biomedical sensing and augmented and/or virtual reality. SiN is also unique for its low losses, which enables more complex circuitry. Lastly, SiPh is the only material that can be manufactured in the same fabs already used to process electronic circuits. This compatibility with established manufacturing facilities gives Silicon Photonics a substantial edge in high-volume markets [5]. While InP, SiN, and SiPh are currently the most advanced integrated photonics platforms, other materials bring unique properties and new possibilities. For instance, materials like barium titanate, lithium niobate, and polymer-based photonics are highly promising for developing ultrahigh-speed modulators, which could enable faster data transmission. Additionally, gallium-based compounds (such as GaN and GaAs) show strong potential in visible-light applications. These emerging materials are poised to expand the capabilities of integrated photonics, offering additional options for specialized functions and further enriching the photonics toolkit [6].
In the realm of integrated photonics, data centers and telecommunications hubs consume staggering amounts of energy to transfer digital information—surpassing even the energy required to move airplanes across the globe. To address this challenge, integration is a critical strategy for improving energy efficiency and reducing costs. Combining electronic integrated circuits and photonic ones on a unified platform, particularly the one based on silicon, enables high-speed data transmission using photons. This integration supports communication over a wide range of distances, from intercontinental links to intra-chip interconnections, while simultaneously maximizing bandwidth and minimizing power consumption. Research in photonic integration and silicon photonics combines theoretical and experimental methodologies. It involves advanced electromagnetic simulations, precise investigations into photon–matter interactions, hybrid integration techniques, nano-photonic design and fabrication, electronic-photonic co-design approaches, as well as cutting-edge al-

gorithms and optical signal transmission and detection methods. These multidisciplinary efforts are essential for overcoming the energy bottlenecks of modern digital communication systems and achieving scalable, energy-efficient photonic solutions. Various on-chip solutions are currently under exploration, including electro-optic modulation and micro-resonator-based Kerr frequency comb generation [7].
During my PhD activities, I concentrated on photonic devices that have a critical role in optical communication systems, both theoretically and experimentally.
Firstly, I focused on the case where photonic analog to digital converters (PADCs) are used to enhance the performance limitations of electronic analog to digital converters (EADCs). Specifically, I concentrated on the spectrally sliced PADC architectures, due to their relevance for coherent receivers. In spectral slicing, the input wideband signal is divided into multiple narrower frequency bands (spectral slices), each slice occupying a specific frequency range [8]. Each slice is mixed with its corresponding reference tone, where frequency down-conversion is performed to shift the spectral slice from its original frequency range to baseband (centered around 0 Hz), while retaining all its information. By shifting each slice to baseband, the sub-EADC can effectively sample and digitize the signal using a manageable sampling rate, as the bandwidth of each slice is now lower and limited to its baseband equivalent [9]. The slicing reduces the bandwidth that each EADC has to handle, allowing standard EADCs to process high-frequency signals that exceed their individual Nyquist limits.
Secondly, I focused on a technique to measure dispersion of integrated waveguide device that contains chirped Bragg gratings. The relevance of this second activity comes from the fact that in optical communication two major techniques are employed to convey information from the central office to the users, that is time division multiplexing (TDM) and wavelength division multiplexing (WDM). In TDM, a single source is used at the transmitter and copies of information is sent to every user, but each user makes use of the time-slot allocated to him/her. This means there is efficiency at the transmitter and inefficiency at the receiver. For WDM, multiple sources are used at the transmitter and only the block of data required by the user is sent to him/her. This means there is inefficiency at the transmitter and efficiency at the receiver. The technique to harness the benefits of TDM at the transmitter and WDM

at the receiver, to improve overall performance, lies in the implementation of on-chip optical Fourier transform (OFT). This chip contains chirped Bragg gratings that serves as a dispersive medium and the dispersion generated needs to be measured, hence the measurement technique I worked on.

The first chapter of this thesis delves into photonic ADCs, a class of devices that exploit the high bandwidth and low latency of optical technologies to overcome the limitations of their electronic counterparts. Among the architectures explored, the spectrally sliced ADC stands out for its ability to enable high-speed signal sampling by dividing the optical spectrum into narrower channels. A critical challenge in these systems is timing jitter, which arises from both optical and electrical sources [8]. By studying the impact of these jitter sources using the models proposed in [8], this work evaluates the performance limits of photonic ADCs, drawing on results from foundational theories. The energy efficiency of photonic ADCs, a key performance metric in energy-sensitive applications, is analyzed using a model proposed in [10] which combines three limiting cases: jitter-limited, shot noise-limited, and thermal noise-limited energy per sample. This comprehensive review analysis sheds light on the viability of photonic ADCs for next-generation communication systems, especially where low energy-per-bit consumption is paramount.

The second chapter of this thesis shifts focus to a different physical phenomenon, which is dispersion—and its measurement in waveguide devices. As part of my PhD program, I visited the Electrical and Photonics Engineering Department at the Technical University of Denmark (DTU) for six months, working with Profesor Michael Galili, who is in charge of the High Speed Optical Communication (HSOC) laboratory. My supervisor Professor Michael Galili, Dr Peter David Girouard and I formulated a new method of measuring the dispersion of a newly fabricated device which was available in the laboratory, which represents an alternative to the established measurement techniques. Dispersion is a critical parameter in optical communication systems as it fundamentally limits the capacity of the network [11]. In particular, this work investigates waveguides incorporating chirped Bragg gratings, which are designed to generate controlled dispersion for applications such as optical Fourier transform (OFT) on a chip. The interplay of reflected light at the waveguide's

edges and within its structure gives rise to a Michelson interferometric effect, a phenomenon harnessed to analyze the reflected spectrum. By developing and validating an analytical model that aligns with experimental results, this study demonstrates a robust methodology for quantifying dispersion in photonic devices. Importantly, the measured dispersion closely matches the designed values, underscoring the precision and utility of the approach and also, the technique is faster than the established ones. The two chapters converge in their relevance to modern optical communication challenges. Photonic ADCs aim to enhance the speed and energy efficiency of signal processing, while dispersion measurement techniques are critical for characterizing and optimizing the components that mitigate signal distortion over optical links. Together, these contributions provide a holistic understanding of the interplay between physical phenomena and device performance, offering insights into how to design photonic systems that balance speed, accuracy, and energy efficiency.

Chapter 3 of this work talks about some of the building blocks of photonic integrated circuits. I used COMSOL Multiphysics software which is based on finite element method (FEM), to do simulations on the main photonic devices at the beginning of my PhD. Parameters, such as effective index, group index, and chromatic dispersion were simulated to understand their dependence on independent variables like wavelength and waveguide dimensions for different types of waveguides. I analyzed also the directional coupler to understand its behaviour, calculating the coupling coefficient using the supermode analysis. Finally, power sharing using the directional couplers is studied to understand the wavelength impact on the coupling condition.

Chapter 1

Photonic Analog to Digital Converters for optical communications

1.1 Introduction

Analog to digital converters (ADCs) play a crucial role in bridging the analog world with digital systems, forming a foundation for much of today's technology. The performance of ADCs—in terms of speed, accuracy, and efficiency—significantly influences the design and effectiveness of diverse systems. Their impact extends across numerous fields, where they enable accurate digital representation of real-world signals. In optical and wireless communications, ADCs are essential for converting signal waveforms for processing and transmission. They are also critical in applications such as electronic defense, medical imaging, and precision instrumentation, where high-quality signal conversion is required for effective data interpretation and analysis. The capabilities of ADCs therefore directly affect system performance, making them fundamental components in modern technological applications [12, 13].

Real-world signals are inherently analog, making analog to digital and digital to analog (DAC) converters—collectively known as data converters—essential components in modern technology. These devices enable seamless interaction between analog signals and digital systems, supporting a wide range of applications [14, 15]. Fig 1.1 shows the numerous application areas of ADCs.

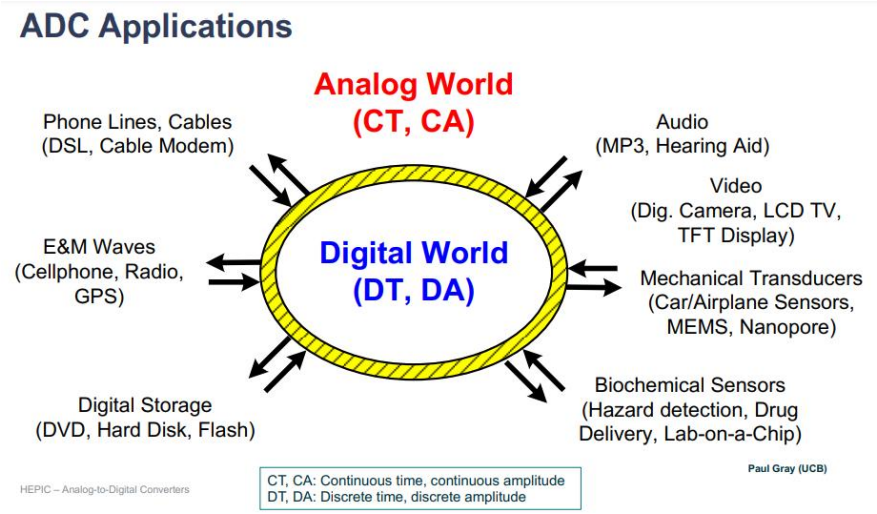

Figure 1.1: The numerous application areas of ADCs, ubiquitous in our modern day technology. [14]

Traditional electronic ADCs exist in different architectures, with changes in resolutions, bandwidth, precision, speed, conversion time and other specifications. The most common electronic ADC architectures include:

1. flash (or parallel comparator);
2. successive approximation;
3. delta-sigma;

4. n-stage pipeline;

5. integrating ADCs with single-slope and multi-slope designs [15].

Basically, all the electronic ADC architectures operate in three main steps: sampling, quantization and encoding [14].

ADC sampling is the process of measuring the amplitude of the continuous analog signal at regular intervals, known as the sampling rate. The frequency of sampling $f_{sampling}$ is usually chosen based on the Nyquist-Shannon criterion, which states that the sampling rate should be at least twice the maximum frequency of the signal to avoid aliasing. Mathematically, the Nyquist-Shannon sampling theorem is given as:

$$f_{sampling} \geq 2 f_{max} \tag{1.1}$$

where f_{max} is the maximum frequency in the input signal [16]. It is critical to adhere to this relation so that all the information contained in the input signal could theoretically be retained during the sampling process. If $f_{sampling}$ is less than twice f_{max}, an undesirable situation displayed in the bottom plot of Fig. 1.2 occurs, where the input signal is undersampled, and so the reconstructed signal (in blue) is having a much lower frequency than the original one (in yellow). This is known as aliasing and is not desired in signal reconstruction.

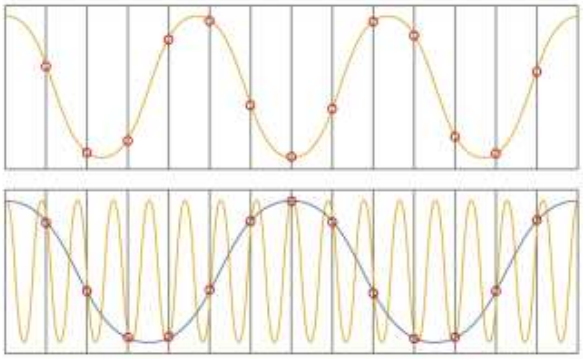

Figure 1.2: (Top) Input signal (in yellow) is oversampled and can be reconstructed from the sampled points (in red). (Bottom) Input signal is undersampled and the reconstructed signal (in blue) has much lower frequency than the input one [16].

In the context of a voltage-time signal graph, the basic operation involved in ADC sampling is to take the values of the voltage at regular time intervals [17]. Fig. 1.3 shows a voltage-time plot with the amplitude of the voltage sampled at regular time intervals.

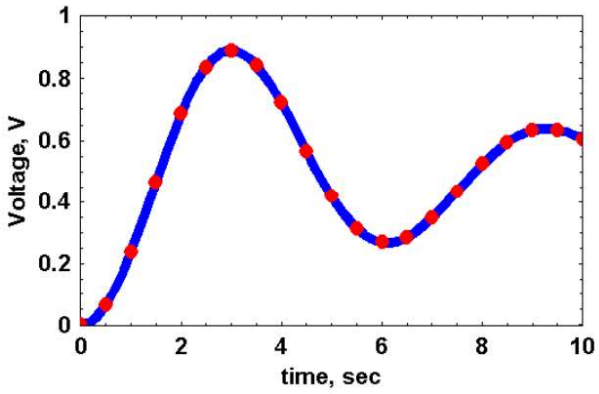

Figure 1.3: Voltage-time graph showing where the input signal is sampled at regular time intervals [17]

After sampling the signal, the ADC assigns each sample to the nearest level in a discrete set of possible values. This process, called **quantization**, involves converting the continuous range of amplitudes into a finite number of levels, introducing quantization error, which is the difference between the actual signal value and the quantized one. The number of quantization steps in the discrete set of possible values is obtained as $2^N - 1$, where N is the number of bits [17, 18]. Fig. 1.4 shows the voltage-time graph, where the sampled voltages are quantized in $2^N - 1$ steps with $N = 3$.

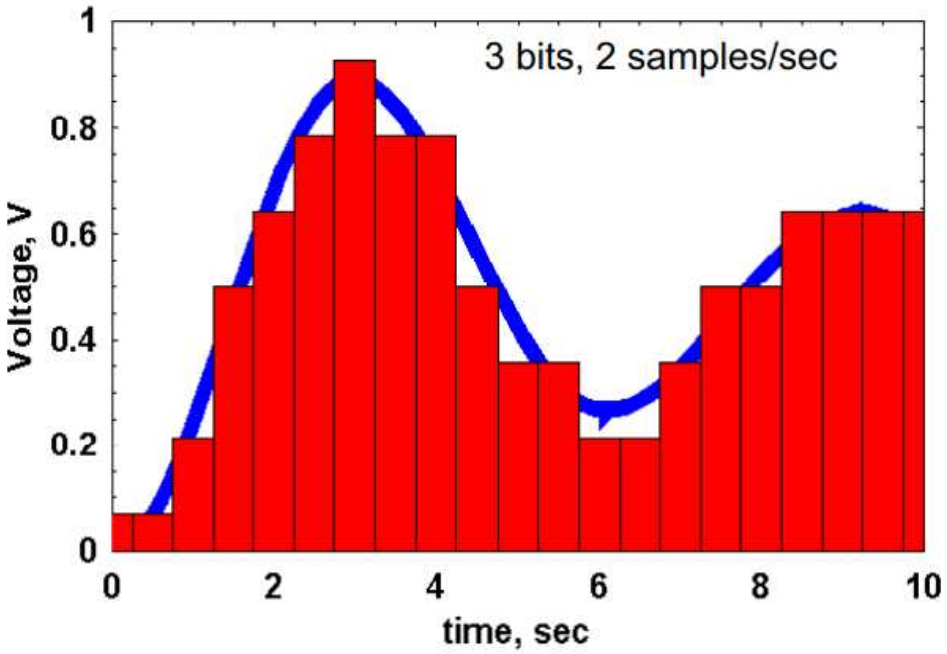

Figure 1.4: Voltage-time graph showing where the sampled voltages are quantized to $2^N - 1$ levels [17].

The quantization error, which is the difference between the original signal and the quantized one, is the only error present in an ideal ADC [19]. Fig. 1.5a shows the voltage-time plot with the input signal in green, quantized signal in red and the quantization error in blue. The quantization step size Δ is the spacing between adjacent levels [18], and it is given as $\Delta = \frac{V_{fs}}{2^N - 1}$, where $V_{fs} = 1$ is the full scale voltage in the context of a sine wave [17]. In the case of uniform quantization step size, the quantization error is uniformly distributed, and therefore the probability distribution function integrates to 1 [20]. Fig. 1.5b shows the graph of the pdf of quantization error.

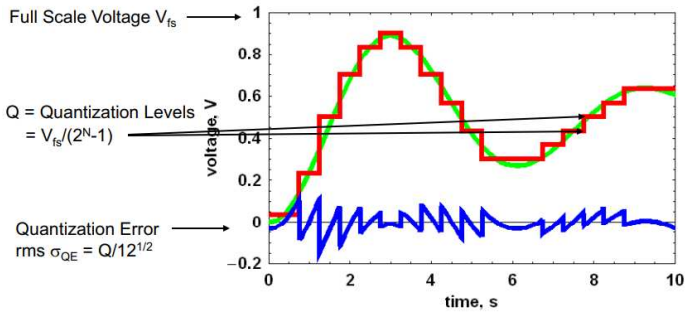

(a) Voltage-time graph showing the input signal in green, the quantized signal in red and the quantization error in blue. [17] .

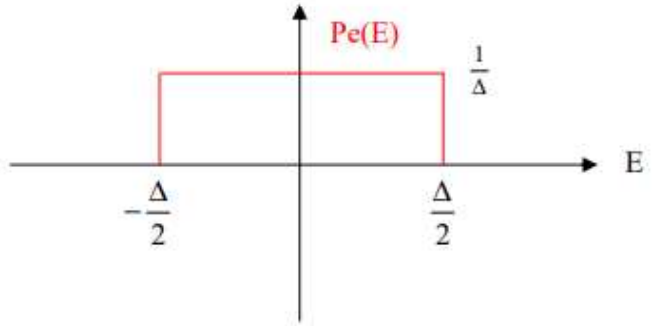

(b) Probability distribution function of the quantization error showing the uniform distribution.

Figure 1.5: (a) Quantization error and (b) pdf of uniform quantization.

In Fig. 1.5b, E represents the quantization error as a random variable. If e is the specific instance of the random variable being evaluated in the expectation, the quantization noise power is given as $E(e^2)$. The quantization noise power is equal to the variance of quantization [21], and from Fig. 1.5b, the variance σ^2 is given as

$$\sigma^2 = E(e^2) = \int_{-\frac{\Delta}{2}}^{\frac{\Delta}{2}} \frac{1}{\Delta} e^2 \, de = \frac{1}{\Delta}\left[\frac{e^3}{3}\right]_{-\frac{\Delta}{2}}^{\frac{\Delta}{2}} = \frac{\Delta^2}{12}$$

The final process is **encoding**. The quantized levels are encoded into a binary format that can be processed by digital systems. This step translates the quantized levels into a digital word, typically represented in binary code, making the information suitable for processing, storage, or transmission in digital form [22].

1.2 Electronic ADC technology trend

The widespread acceptance of Walden's 1999 paper has made it common to refer to resolution (in bits) versus sampling frequency plots as Walden's plots [23]. Fig. 1.6 shows the Walden plot, which is a graph of resolution as a function of sampling rate [13], with a collection of 150 electronic ADCs [23].

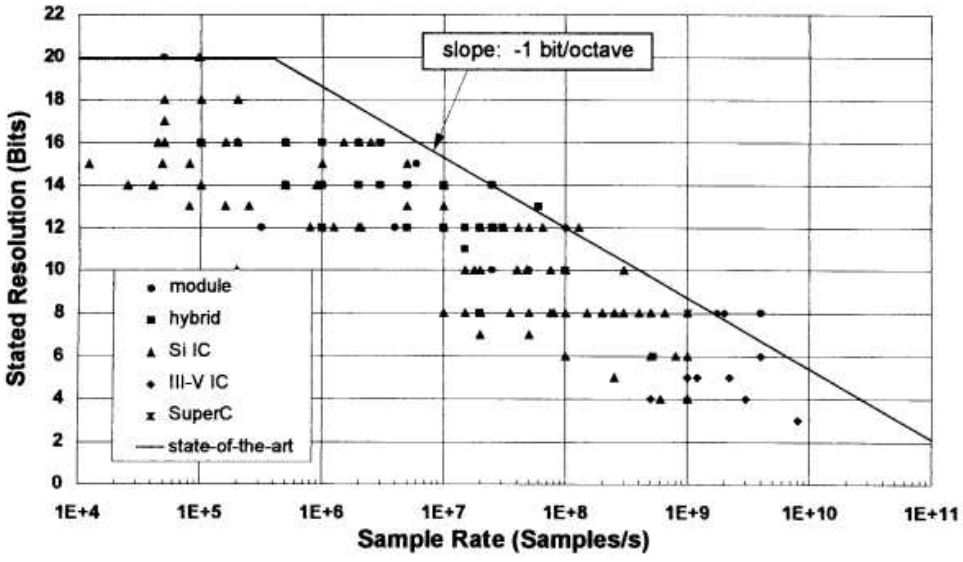

Figure 1.6: The Walden's plot [13]. In this plot from Walden's paper, not all collection of ADCs are indicated

A universal metric for assessing electronic ADC (EADCs) performance is denoted as P, which is defined as the product of the effective number of quantization levels and the sampling rate. Thus, P is given as

$$P = 2^E.f_s \tag{1.2}$$

[13]. Here, E is the effective number of bits (ENOB) and f_s is the sample rate.
The highest-performing ADCs often have significant power dissipation P_{diss}. Consequently, power dissipation can be considered a key aspect of ADC performance. A practical way to evaluate ADC performance is through the use of a figure of merit, F, defined as

$$F = \frac{2^E.f_s}{P_{diss}} \tag{1.3}$$

[24]. In equation 1.2, P assesses the combined effects of speed and resolution whilst in equation 1.3, F assesses the power efficiency with speed and resolution [25]. Based on experimental outcomes [12], Walden derives a new figure of merit (FOM) to represent the energy per conversion step [17] as:

$$FOM_w = \frac{P_{consumption}}{2^E.f_s} \tag{1.4}$$

Here, $P_{consumption}$ is the power consumption. Walden concluded that, while F has increased over time, P has remained relatively stable. He attributed this trend to reductions in power dissipation, driven by increasingly monolithic and power-efficient EADC designs, while resolution and sampling rate remained steady. However, his observations on P and F no longer fully apply to ADC technologies developed after 1997, which marked the end of his data collection. For over two decades, the advancement of EADC technologies has been driven by emerging applications, leading to an exponential rise in power consumption. However, the trends for sampling rate and resolution requirements have followed distinct trajectories [25]. This is depicted in Fig. 1.7, revealing that the demand for higher sampling rate keeps rising. It is also showing that resolution assumes constant value.

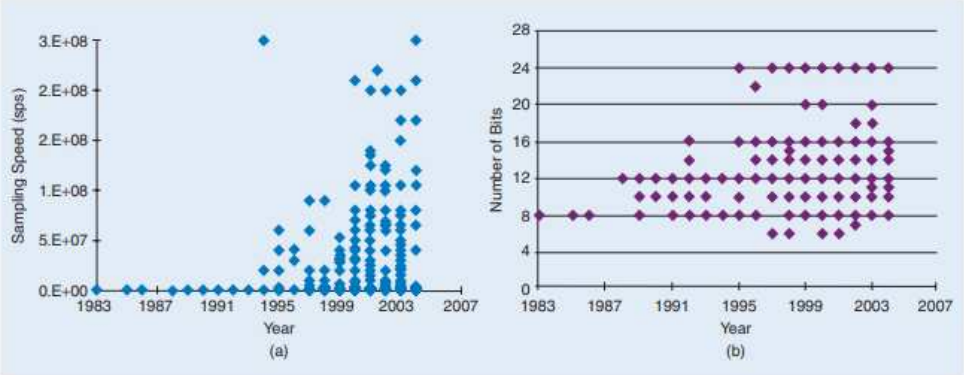

Figure 1.7: EADC trend for (a) sampling speed and (b) resolution/number of bits. [25].

1.2.1 EADC performance metrics and FOMs

The performance metrics of EADCs are critical in evaluating their suitability for specific applications. Some of the key performance metrics used to evaluate EADCs, which are relevant to the subsequent Sections, are listed in Table 1.1.

Table 1.1: Key performance metrics for EADC

Metric	Description
Resolution	The number of bits used by an EADC to represent a signal
Sampling rate	The number of times the analog signal is sampled per second. The higher the sampling rate the better the performance
Signal-to-Noise Ratio (SNR)	Ratio of signal power to noise power
ENOB	It quantifies the actual resolution of an EADC, accounting for noise and distortion. While the EADC may have an 'n-bit' design, ENOB represents the equivalent number of ideal bits that accurately contribute to the output signal.
Bandwidth	The range of input signal frequencies the EADC can accurately convert without significant distortion or loss of fidelity. A higher bandwidth allows ADCs to process faster signals effectively

The various FOMs used to evaluate EADC are given in equation 1.2, 1.3 and 1.4. Another useful FOM is:

$$FOM_S = \frac{SNR.f_s}{2P_{consumption}} \tag{1.5}$$

The parameters in equation 1.5 is called Schreier figure of merit, which is based on the fact that the power consumption of an ADC is directly related to its sampling rate

and SNR. FOMs such as the Schreier and Walden ones are commonly used to evaluate ADCs by relating sampling rate and power consumption. These metrics provide a standardized way to compare EADC efficiency across different designs. Sampling rate reflects the ADC's speed, while power consumption impacts energy efficiency. High FOMs indicate efficient EADC designs optimized for specific applications [12]. Following the analyses from [17], based on equation 1.4, for an ENOB of 10 bits and a sampling rate of 10 GS/s, Table 1.2 shows the power required by an EADC for selected energy per conversion steps (pJ/cs)

Table 1.2: Power required by an EADC for different values of the energy per conversion steps

ENOB [bits]	f_s [GS/s]	Energy per conversion steps [pJ/cs]	Required power [W]
10	10	0.2	2
10	10	10	100
10	10	100	1000

From Table 1.2, the big question here is, as the demand for higher sampling rate keeps increasing (as depicted in Fig. 1.7), what can be done to reduce/maintain the power consumption and also meet the demand for higher sampling rate?

1.3 EADCs for modern optical communication

Modern optical communication systems often employ high-speed EADCs with bandwidths in the tens of Gigahertz. Recent advancements have pushed these bandwidths beyond 100 GHz [12], and higher-resolution EADCs are increasingly required to support advanced modulation formats and maximize channel spectral efficiency [12, 26]. From Fig. 1.6 it is clear that ADCs exhibit resolution-sampling rate trade-off [12], and therefore EADCs with a balance between resolution and sampling rate is the way to go. Fig. 1.8 shows the resolution-sample rate plot and where the EADC

architectures operate. EADCs are utilized across a wide range of applications, with diverse types and performance characteristics. Selecting the most appropriate EADC requires careful consideration of the specific requirements and characteristics of the target application to ensure optimal performance [27]. From Fig. 1.8 the EADC architectures that offer a balance between resolution and sample rate are successive approximation register (SAR) EADC, and Sigma-Delta ($\Sigma - \Delta$) EADC. Analysis and trends indicate that SAR EADCs are commonly utilized due to their high efficiency, excellent speed performance, and strong scalability [28].

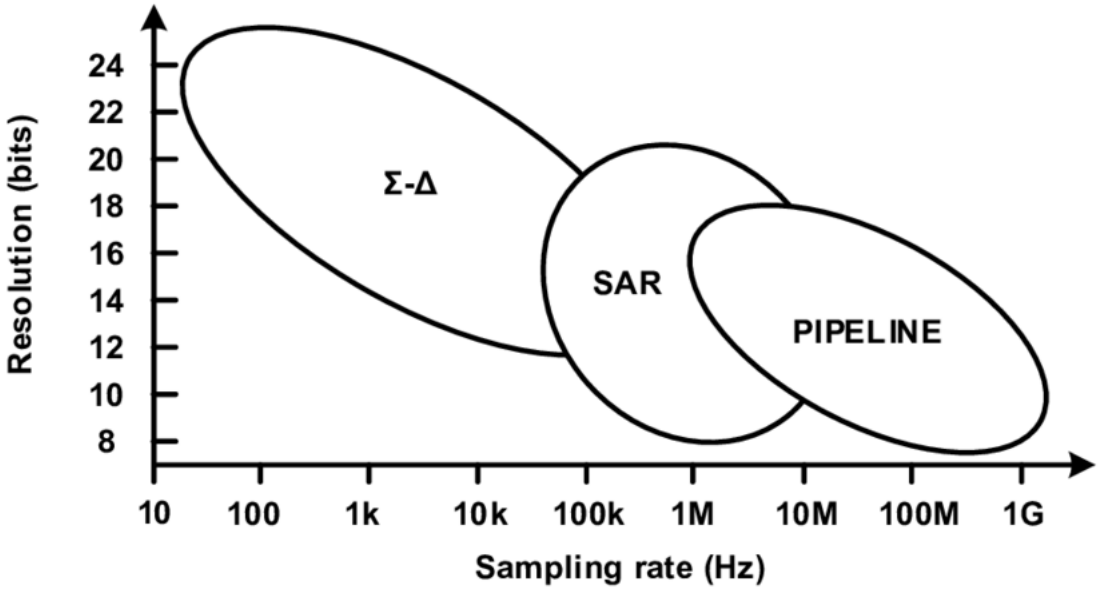

Figure 1.8: Resolution-sample rate graph, with the regions where the different EADC architecutres operate [27].

1.3.1 EADC bottlenecks

In the past (before 1999), the accuracy of high-speed converters was primarily constrained by the switching speeds of integrated circuit technologies, like InP or GaAs based ones. In contrast, lower-speed converters were generally limited by thermal

noise [29]. Advances in converter design have shifted the primary limitations for high-speed EADCs from circuit technology to factors such as sampling clock jitter and comparator ambiguity, which often drive the resolution-sampling rate trade-off [29, 30]. Table 1.3 shows the performance of selected EADCs based on different parameters [28].

Table 1.3: Performance of EADCs based on different parameters, from [28]

Reference No. from [28]	Publication year	Sample rate	Power consumption	Resolution
4	2008	45MS/s	-	-
6	2009	-	130mW	-
12	2015	100MS/s	1.5mW	10bits
17	2005	1MS/s	105mW	16bits
18	2005	-	3mW	4bits
21	2016	100MS/s	0.35mW	-
35	2019	1.6GS/s	163mW	-
36	2019	1GS/s	31.5mW	12bits
37	2018	5MS/s	8nW	-
38	2017	900MS/s	3.5mW	8bits
39	2018	1MS/s	-	14bits
40	2018	-	1mW/element	-
41	2018	-	4.51mW	-
42	2015	178.6KS/s	8uW	6bits
52	2017	900MHz	35mW	8bits
53	2011	1GS/s	26mW	6bits
54	2018	10GS/s	1.5mW	6bits
70	2015	6.14MS/s	6.43uW	-

Table 1.3 provides an interesting insight about the current EADCs and whether they can be able to meet the demands of high sampling rate and bandwidth in today's mo-

bile and internet traffic. Fig. 1.9a and Fig. 1.9b show the growth of global machine to machine (M2M) connection and of the global internet one respectively. With the advent of autonomous vehicles, internet of things (IoT), online gaming, video streaming, etc, the growing need for higher data rates and bandwidth in modern telecommunication technologies has driven EADCs to their fundamental performance limits [12]. As electronic systems approach their physical boundaries, achieving further advancements in high-speed, high-resolution data conversion requires a transformative approach. This paradigm shift is essential for overcoming current limitations and enabling continued progress in meeting the demands of next-generation communication systems. Exploring innovative architectures and leveraging emerging technologies will play a critical role in shaping the future of data conversion.

(a) Global Machine to Machine connection growth.

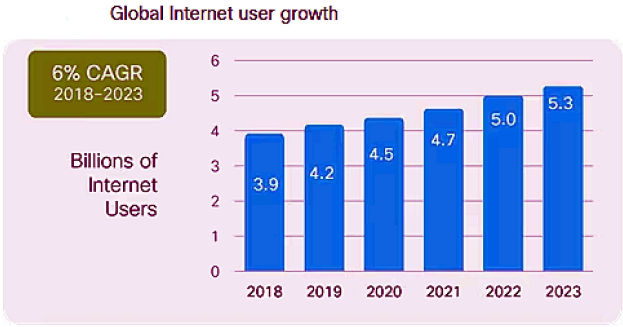

(b) Global growth in Internet users. Source: Cisco Annual Internet Report, 2018–2023.

Figure 1.9: Combined visualization of global growth trends in internet connection.

1.4 Photonics ADC (PADC)

The review summarized in the previous Sections has revealed that the traditional EADCs have limitations in speed (sample rate), bandwidth and sampling clock jitter, as well as power consumption. According to Cisco annual report 2018–2023,

mobile applications drive future consumer, small to medium businesses (SMB) and enterprise application needs. It was estimated that in 2023, 299.1 billion mobile applications were downloaded globally. Social media, gaming and business applications were the main drive in this high volume of traffic. This is depicted in Fig. 1.10, and it is an indication that the need for higher sampling rate, bandwidth and resolution cannot be overemphasized.

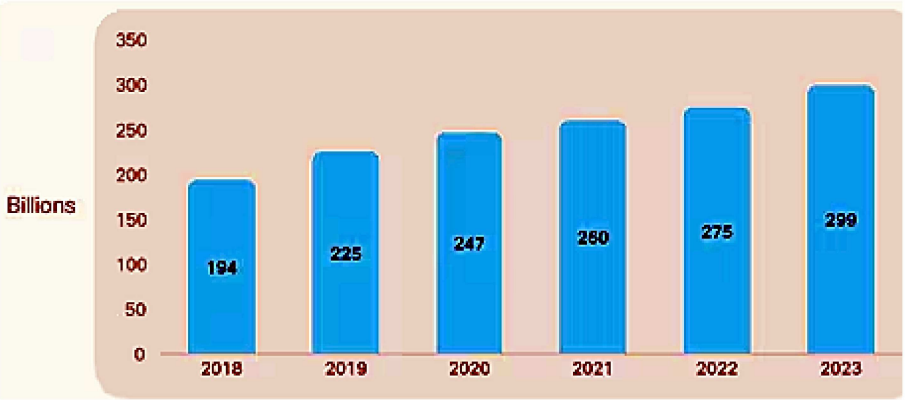

Figure 1.10: In 2023 nearly 300 billion mobile applications were downloaded worldwide. Cisco Annual Internet Report, 2018–2023.

Again, Table 1.4 shows the performance of the best EADCs in [28] and the target for next generation EADCs in [30] as at 2016, in order to keep pace with the increasing demand for higher sampling rate, bandwidth and resolution. Although the target value in [30] originates from a 2016 study, it remains the most recent comprehensive benchmark available and is therefore being used as a reference for evaluating next-generation EADCs. In relation to Table 1.3, the emphasis is on parameters such as resolution, conversion rate (sample rate) and power. From Table 1.4, the sample rate, resolution and power consumption for the next generation as at 2016 are expected to be: 130 GS/s, 6-10 bits and the power is yet to be confirmed (TBC), respectively. These values confirm the bottleneck issue currently being faced by EADCs.

Table 1.4: Best performing EADCs vs target for next generation as at 2016

Parameter	Best performing EADC in [28]	Target for next generation EADC as at 2016
Resolution	6 bits	6-10 bits
Sample rate	10 GS/s	130 GS/s
Power	1.5 mW	TBC

Since optical connections are anticipated to achieve single-channel data rates of 1 Tbit/s in the near future [31–34], a significant obstacle to meeting the demand in processing this 1 Tbit/s lies in the limitations of traditional EADCs in receivers for the data conversion [31, 35–37].

Photonic analog to digital converters (PADCs) have emerged as a transformative technology, leveraging the inherent advantages of photonics to surpass the sampling rates and bandwidth limitations of traditional electronic systems. These devices utilize the speed and parallelism of light to enable high-performance data conversion, meeting the demands of modern high-speed communication and signal processing applications [12, 31, 38].

EADC sampling relies on sample-and-hold circuits, which introduce aperture jitter during the sampling process [31]. Leveraging the low jitter properties of PADCs offers several advantages. Jitter, which refers to timing variations in signal sampling, is a critical factor affecting ADC performance, particularly at high sampling rates. PADCs inherently minimize jitter due to the precision and stability of optical components, such as mode-locked lasers and optical modulators [38, 39]. Fig. 1.11 provides the Walden plot with additional data of the aperture jitter. In this plot, each point represents an ADC, blue circles denote EADCs from Walden's 2007 survey, while dark blue circles represent high-performance EADCs developed post-2007. Dashed lines indicate constant aperture jitter values, with annotations specifying the jitter levels and the years they were achieved [39]. It also shows the improvement in ENOB that can be obtained by adopting PADCs. In general, this plot highlights technological advancements in PADCs and the relationship between ENOB, input frequency, and

jitter.

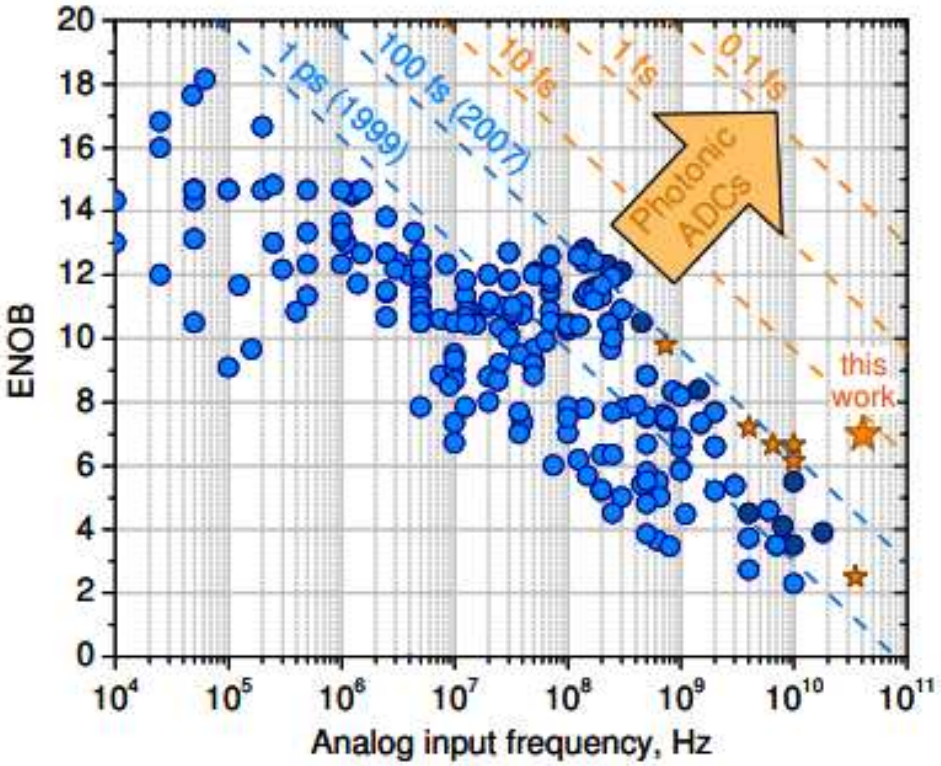

Figure 1.11: The Walden plot, illustrating ENOB of EADCs as a function of analog input frequency. Also the high-performance that can be obtained by adopting PADCs is indicated [39].

Photonics components' compatibility with CMOS technology is a significant advancement in integrating optical and electronic systems [31]. CMOS technology is the foundation of most modern electronic circuits due to its cost efficiency, scalability, and widespread use in microelectronics [40]. CMOS-compatible photonics facilitates high-speed data conversion and transmission and efficient signal processing, addressing challenges in areas such as optical communication, data centers, and high-performance computing. Moreover, it enables the development of compact, energy-

efficient photonic systems, crucial for next-generation technologies like artificial intelligence and quantum computing [31, 41–43].

1.4.1 Classes of PADCs

Based on the detailed work done in [44], PADCs are categorized into 4 classes, that is:

1. photonic-sampled ADC;
2. photonic-quantized ADC;
3. photonic-sampled and quantized;
4. photonic-assisted ADCs

These are shown pictorially in Fig. 1.12.

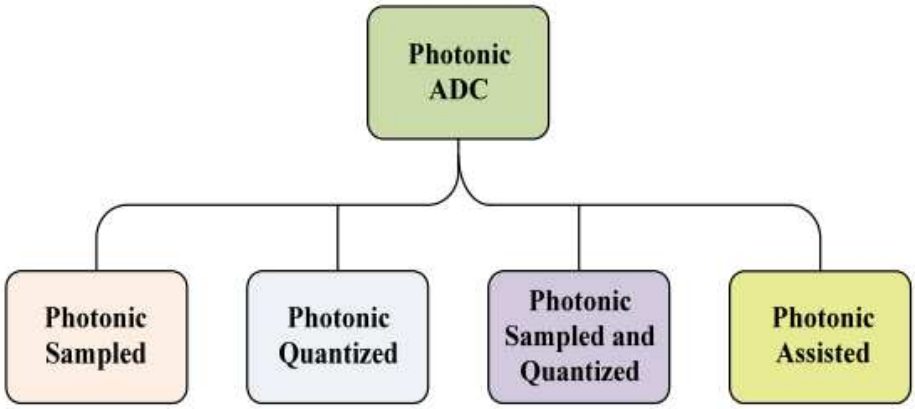

Figure 1.12: The four classes of PADCs. [45].

Based on [45], the four classes of PADCs can be briefly explained as follows.

1. **Photonic-sampled ADCs** perform signal sampling in the optical domain, while the quantization step is executed in the electronic domain.

2. **Photonic-quantized ADCs** perform quantization in the optical domain while the sampling is done in the electronic domain.

3. **Photonic-sampled and quantized ADCs** execute both the sampling and quantization processes within the optical domain.

4. **Photonic-assisted ADCs** leverage photonic technologies to enhance the performance limitations of EADCs, while both the sampling and quantization processes are carried out in the electronic domain.

Apart from photonic-assisted ADCs, that utilize a mode-locked laser as a clock source for an electronic ADC, all other PADC classes incorporate an analog optical link connecting the RF input to the digital output. Technically, the term photonic ADC would describe a device that takes an analog optical signal as input, and outputs a digital optical signal, such as a camera digitizing light for optical transmission. However, such devices are rare. Instead, photonic ADC typically refers to systems with an analog RF electronic input and a digital electronic output, where photonics plays a key role in the digitization process. Detailed discussion on the four classes of PADCs can be found in [44].

1.5 PADC architecture

Photonic ADCs have been demonstrated using various concepts [8, 12, 44]. Two of the main architectures are time-interleaved and the frequency-interleaved/spectrally-sliced ones. In time-domain approaches, all sub PADCs in a time-interleaving architecture asynchronously sample the same input signal with uniformly shifted clocks [46–48]. Conversely, in frequency-interleaving architectures, the input is mixed with local oscillators (LOs) at evenly spaced center frequencies per channel. These baseband signals are then synchronously sampled using a common clock [46, 49].

1.5.1 Time-Interleaving Architecture

Fig. 1.13 shows the schematic of the time-interleaving (TI) architecture, where a mode-locked laser (MLL) generates a pulse train with a repetition period T_r. This train of pulses is split using a coarse wavelength division demultiplexer into N pulse trains, each centered at distinct frequencies, but retaining the original repetition rate. The trains are delayed incrementally by T_r/N and recombined, forming interleaved pulses at different center frequencies, spaced by T_r/N. After signal modulation, the pulses are separated by a WDM-demux and directed to N photodetectors (PD) and EADCs, each operating at $1/N$ of the total sampling rate [8]. Basically, each sub EADC samples and begins to convert the input signal into bits at different time intervals [50]. Table 1.5 shows the activities at the sub EADCs in the TI architecture.

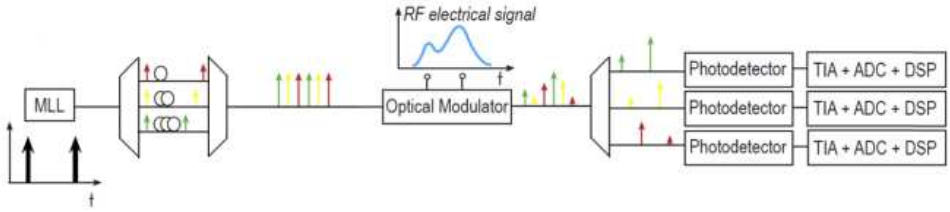

Figure 1.13: The TI Architecture [8].

Table 1.5: TI operation at the sub EADCs, with $M =$ number of sub EADCs and $T_s =$ delay.

EADC No.	**Samples and begins to convert into bit at time** ($t_0 + delay$)
1	$V_{in}(t_0)$
2	$V_{in}(t_0 + T_s)$
3	$V_{in}(t_0 + 2T_s)$
M	$V_{in}(t_0 + (M-1)T_s)$
Next cycle M+1	$V_{in}(t_0 + MT_s)$

In this thesis, the focus is on spectrally sliced optically enabled ADCs based on frequency-interleaving. Detailed discussion on TI PADC implemented on silicon nitride platform can be found in [51].

1.5.2 Frequency-Interleaving/Spectrally sliced architecture

Fig. 1.14 provides the schematic of the Frequency-Interleaving (FI) architecture. An electric signal is amplitude-modulated onto a continuous-wave (CW) carrier, producing a wideband optical signal. This signal is then divided into *N* channels using optical passband filters. Each channel is analyzed by mixing it with a specific reference tone derived from a MLL comb line. After photodetection by *N* PDs and subsequent digitization by *N* sub EADCs, a digital signal processor (DSP) combines the spectral slices to reconstruct the original signal [8].

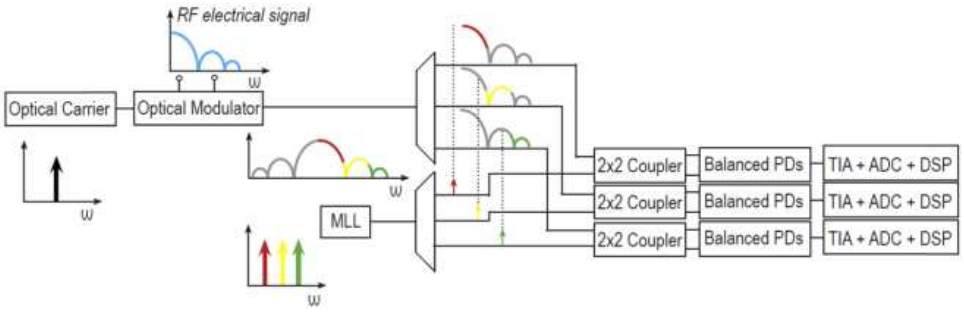

Figure 1.14: The FI Architecture [8].

Several PADCs have been implemented using either TI or FI concept and a number of results have been achieved in terms of bandwidth, ENOB, sampling rate, SNR, Free Spectral Range (FSR), signal to noise and distortion ratio (SNDR), Carrier to Noise Ratio (CNR), power consumption, etc.

For instance, [52] presents an ultra-broadband photonic-electronic ADC leveraging an integrated Kerr soliton frequency comb for spectral multiplexing in the optical domain. The approach employs a high-speed electro-optic (EO) modulator to convert the analog electrical waveform into an optical signal. This signal is spectrally decomposed into tributaries, which are then coherently detected using phase-locked tones

from the Kerr comb as local oscillators (LOs). Fig. 1.15 provides a schematic of the proposed architecture. Detailed schematic and description is provided in [52].

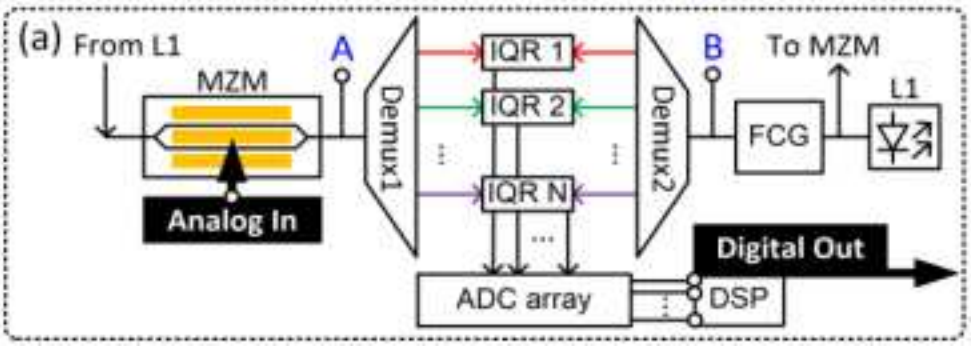

Figure 1.15: Ultra-broadband photonic-electronic ADC proposed in [52].

In [53] a review on optically enabled time- and frequency-interleaved ADCs is provided, along with their monolithic integration into electronic-photonic integrated circuits. For signal frequencies up to 65 GHz, an optoelectronic track-and-hold amplifier using a source-emitter-follower architecture demonstrates power-efficient performance in optically enabled BiCMOS technology. For higher frequencies, integrated photonic filters facilitate signal slicing in the frequency domain, enabling further scaling of conversion bandwidth. Notably, the reconstruction of a 140 GHz optical signal highlights the potential of this approach for ultra-high-speed signal processing. Fig. 1.16 displays the schematic of the track and hold amplifier proposed. Detailed description of the operation of this scheme is provided in [53].

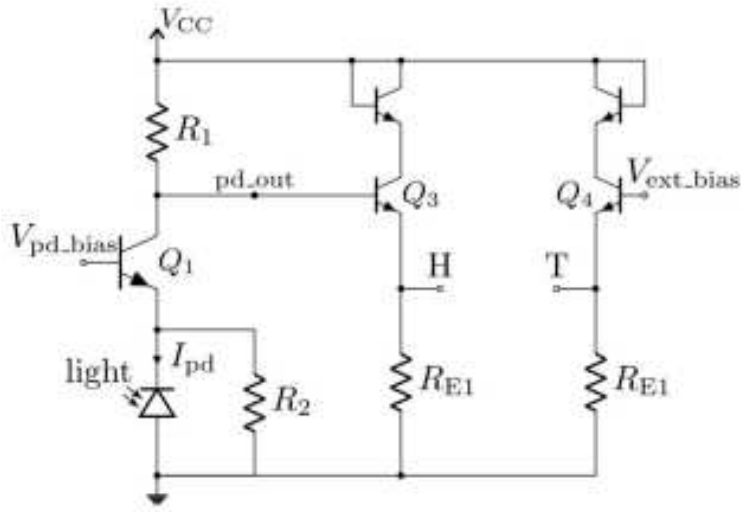

Figure 1.16: The track and hold amplifier proposed in [53].

Again, [51] presents the design and experimental evaluation of a silicon nitride (SiN) pulse interleaver, utilizing coupled resonator optical waveguide (CROW) filters. To achieve an FSR of 1.44 THz, and given the low optical confinement of the silicon nitride platform, tapered waveguides are incorporated into the individual ring resonator design. The interleaver's potential application in time-interleaved photonically assisted ADCs is explored by integrating experimental results from the photonic integrated circuit with a comprehensive model of the complete PADC system. Fig. 1.17 provides the schematic of the proposed architecture. Detailed description is reported in [51].

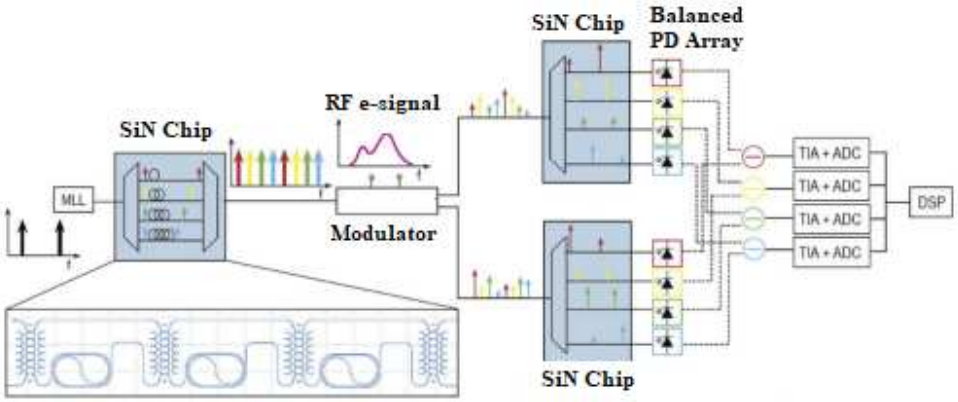

Figure 1.17: The SiN pulse interleaver proposed in [51].

A 4-channel time-wavelength optical pulse interleaver integrated on a silicon chip is presented also in [54]. The device generates a sequence of pulses with periodically varying wavelengths by demultiplexing an input pulse train into multiple wavelength components, introducing relative delays among them, and then recombining them into a single output. The design employs microring resonator arrays for wavelength multiplexing and demultiplexing, along with extended silicon waveguides that serve as delay lines, achieving efficient integration within a compact silicon photonic platform. Fig. 1.18 shows the schematic of the time-wavelength architecture proposed. Detaile explanation of this architecture is found in [54].

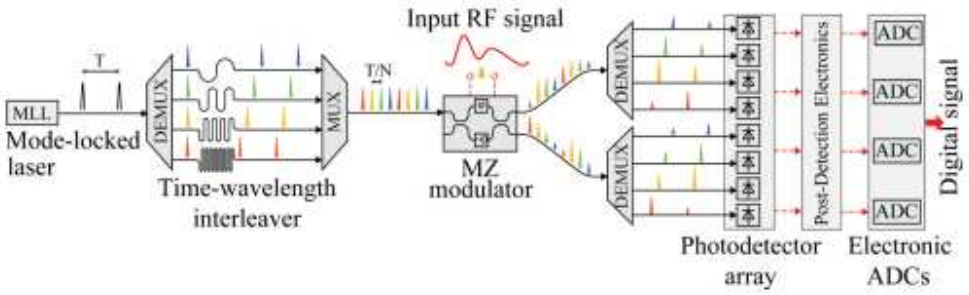

Figure 1.18: The time-wavelength architecture proposed in [54].

Lastly, in [31], an investigation is done on optical sub-Nyquist orthogonal sampling

using sinc-pulse sequences to time-interleave high-bandwidth input signals into parallel low-bandwidth sub-signals during an initial sampling stage. These sub-signals are subsequently detected and processed in parallel branches using low-bandwidth EADC devices in a second sampling stage. Fig.1.19 shows the proposed time-interleaved PADC architecture. Details of the decription is found in [31].

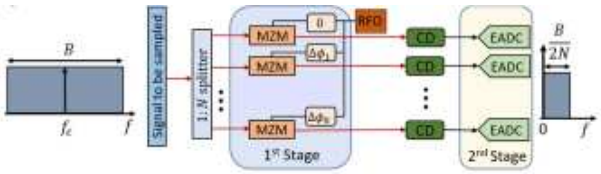

Figure 1.19: The time-interleaved PADC architecture proposed in [31]. MZM: Mach–Zehnder modulator, RFO: Radio-frequency oscillator, CD: Coherent detection.

Table 1.6 provides a list of selected PADCs and their performance based on the above-mentioned metrics. Comparing the performance of EADCs listed in Table 1.3 with that of PADCs in Table 1.6, clearly, PADCs have much higher sample rate (which imply higher bandwidth in bits/s) than that of the EADCs. One may argue that, from the table, some EADCs are having higher resolution. Fig. 1.7 reveals that greater number of EADCs have resolution $\leq$ 10 bits. Also from [44], a PADC with moderate resolution ($\leq$10 bits) and higher bandwidth is preferred to ADC with higher resolution (>10 bits) and low bandwidth.

Table 1.6: Performance of selected PADCs (both TI and FI)

Metric	[52]	[53]	[31]	[30] Target values
Resolution	-	-	-	6-10 bits
Sample rate	-	400 GS/s	126 GS/s	34 to >130 GSa/s
ENOB	2.3 bits	-	6.92 bits	5.5 to > 8.5 bits
Bandwidth	320 GHz	140 GHz	62.5 GHz	>44 GHz
3-dB Bandwidth	-	33 GHz	-	-
SNR	-	18.3 dB	-	-
SNDR	15.7 dB	-	-	-
FSR	40.25 GHz	-	-	-
CNR	22.6 dB	-	-	-
mod. scheme	QPSK 16 QAM 32 QAM	16 QAM	-	-
Foot print	-	-	-	$\leq$ 25x25 mm
Insertion loss	-	-	-	-
Power consumption	-	100 mW	-	<1 pJ/cs ?

1.6 Effect of timing jitter on PADCs

This section focuses on the effect of timing jitter on the performance of PADCs, specifically optically enabled spectrally sliced ADCs, following the analysis from [8]. Fig. 1.20 provides a detailed schematic of the proposed architecture to demonstrate a spectrally sliced, optically enabled ADC integrated into a silicon electronic-photonic integrated circuit (ePIC). The RF input signal is modulated onto a single-frequency laser, then spectrally divided into multiple channels via 3rd-order CROW filters configured for drop operation. Each channel undergoes heterodyne detection using coherent receivers, with distinct MLL lines serving as reference tones. Functionalities implemented within the ePIC are highlighted in the green area of the diagram.

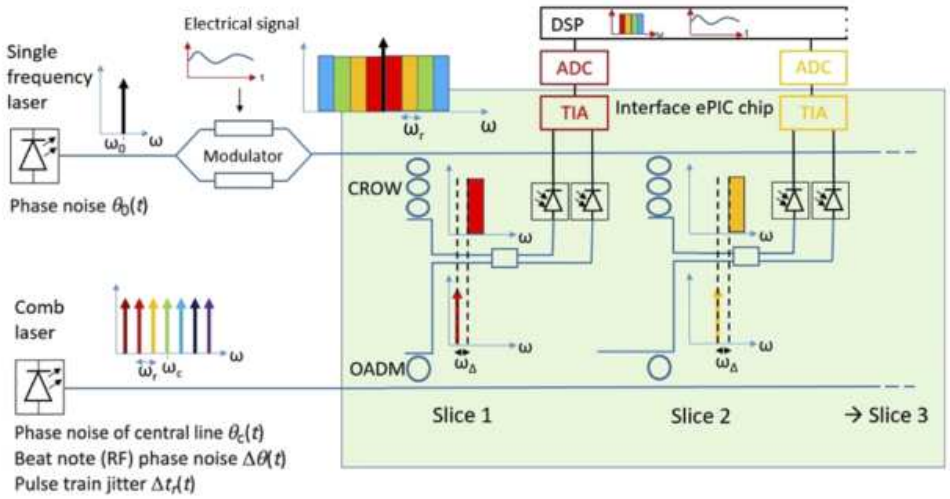

Figure 1.20: Detailed schematic of proposed FI Architecture [8].

In the system performance analysis, three sources of noise were considered:

1. phase noise from the optical carrier sent through the electro-optic modulator;
2. phase noise from the central MLL comb line;
3. RF phase noise from the pulse train generated by the MLL.

Phase noise from the single-frequency laser arises due to the inherent phase instability of the single-frequency laser acting as the optical carrier. It impacts the modulated optical signal directly. Phase noise from the central reference is specific to the central line of the MLL comb, which serves as a critical reference tone for coherent detection. Phase noise from the pulse train corresponds to the RF phase noise resulting from the timing jitter or phase fluctuations in the pulse train generated by the MLL, affecting all comb lines used as reference tones. For each noise source considered, a sinusoidal RF signal with a frequency of 100 GHz is passed through the system while the other two noise sources, as well as noise from electronic digitization, are turned off. As simulation times increase, the sampled signal further deteriorates, as anticipated in the case of phase noise from the pulse train generated by the MLL, revealing a different behavior compared to the previously investigated noise sources that maintained a bounded standard deviation regardless of the simulation time. This indicates that jitter from the MLL is the dominant limiting factor in the performance of the designed PADC. The timing jitter from the MLL $\Delta t_r(t)$ is derived as

$$\Delta t_r(t) = \frac{1}{\omega_r}\sqrt{\Delta\omega_r t}, \tag{1.6}$$

where ω_r is the angular MLL FSR, $\Delta\omega_r$ is the angular MLL linewidth, and t is time. By rounding down the RF signal frequency to the next lower integer number of slices, the jitter of the MLL pulse train $\Delta t_r(t)$ applied to the sampling performed by the PADC is then rescaled as $(m\omega_r/\omega_{RF})\Delta t_r(t)$, being m the index of slice and ω_{RF} the angular input frequency. Typically, the SNR of an EADC is constrained by aperture jitter Δt and the angular frequency ω of the input signal, as expressed by:

$$SNR = 20\log_{10}\left[\frac{1}{\omega\Delta t}\right]. \tag{1.7}$$

By factoring the rescaled MLL jitter, equation 1.7 becomes

$$SNR = 20\log_{10}\left[\frac{1}{(m\omega_r)\Delta t_r(t)}\right]. \tag{1.8}$$

This is the *SNR* limited by the MLL jitter only.

In a similar manner, the electric oscillator jitter $\Delta t_e(t)$ is derived as:

$$\Delta t_e(t) = \frac{1}{\omega_e}\sqrt{\Delta\omega_e t}, \tag{1.9}$$

where ω_e is the angular oscillator frequency and $\Delta\omega_e$ is the angular oscillator linewidth. In the design of the FI PADC, the total signal frequency is substituted by the down-converted frequency which the EADC sees. With this notion in mind, equation 1.8 is generalized to take into account the electrical jitter and the *SNR* becomes

$$SNR = 20\log_{10}\left[\frac{1}{\sqrt{[(m\omega_r)\Delta t_r(t)]^2 + [(\omega_{RF} - m\omega_r)\Delta t_e(t)]^2}}\right]. \tag{1.10}$$

This is the *SNR* when both optical and electrical jitters are considered.

1.6.1 Analytical results

Three conditions were considered in the calculations done using the model proposed in [8]:

1. the only source of noise is the electric jitter;
2. the only source of noise is the optical jitter;
3. both electric and optical jitter are considered.

The inverse of the SNRs, that is the noise to signal ratio NSR, was calculated for the various conditions. Table 1.7 shows the parameters that were set for the calculations.

Table 1.7: Parameters for calculations done using the model in [8]

Parameter	Symbol	Value
MLL FSR	f_r	30 GHz
Oscillator frequency	f_e	75 GHz
Slice index	m	
MLL linewidth	Δf_r	3 kHz
offset	f_Δ	2 GHz
Oscillator linewidth	Δf_e	180 kHz
Input frequency	f_{RF}	0-120 GHz

Fig. 1.21 shows the plot of the NSR versus input frequency when the only source of noise is the electric jitter. The yellow curve indicates fully EADC and the blue curve indicates when slicing is implemented, with the only source of noise being electrical jitter. It can be observed that the noise exhibits an abrupt decrease for every optical sidebands transition to the next higher spectral slice, as the contribution $(\omega_{RF} - m\omega_r)$ suddenly reduces by ω_r. These transitions occur slightly before the input signal frequency ω_{RF} aligns with an integer multiple of the slice width, due to the presence of a guard band ω_Δ. The guard band ensures the design avoids requiring a 90-degree optical hybrid, as well as dual balanced photodetectors and differential transimpedance amplifiers for each channel. The technique used relies on coherent detection and the details of coherent detection in optical receivers are found in [9]

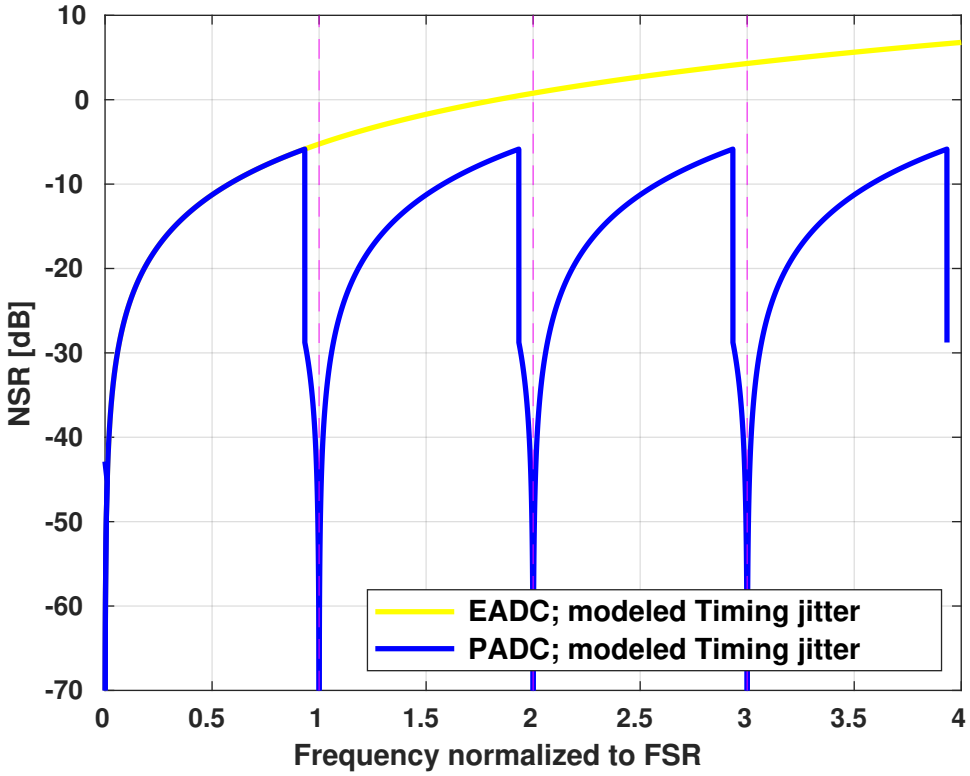

Figure 1.21: NSR obtained when the only source of noise is the electric jitter and slicing is implemented, with $m = 0,1,2,3$, $\Delta t_r(t) = 0$ ps, $\Delta t_e(t) = 2.9$ ps. Yellow curve indicates the modeled timing jitter in equation 1.7 whilst blue curve indicates the modeled timing jitter in equation 1.10

Fig. 1.22 shows the plot of the NSR versus input frequency in the presence of electric jitter and optical one. Here too, the yellow curve is referring to the full EADC and is obtained using equation 1.7. Red and blue curves are obtained using equation 1.10. Blue curve indicates when the only source of noise is optical jitter and red indicates when both optical and electrical jitters are present. Clearly, the red curve shows the performance improvement that can be obtained when implementing slicing with PADC.

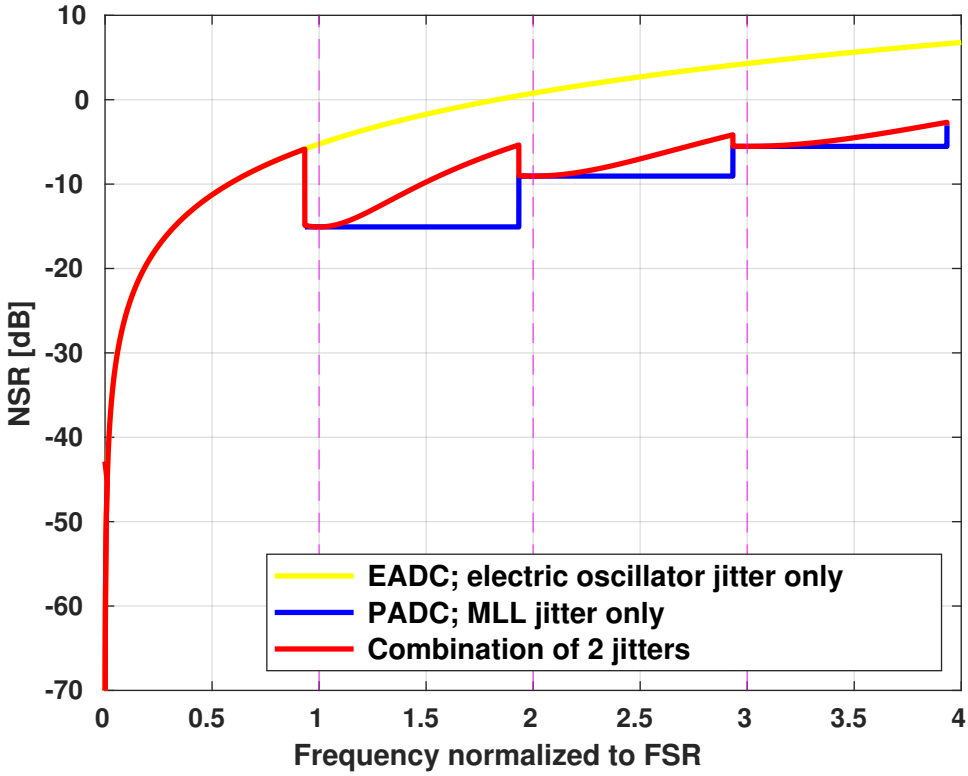

Figure 1.22: NSR obtained when both electric and optical jitter are present and slicing is implemented, with $m = 0,1,2,3$, $\Delta t_r(t) = 0.94$ ps, $\Delta t_e(t) = 2.9$ ps.

1.6.2 Performance analysis based on ENOB

Another significant metric used to evaluate the performance of PADC is ENOB, defined as:

$$ENOB = \frac{SNR[dB] - 1.76}{6.02}, \tag{1.11}$$

where 1.76 is a factor that comes from quantization error of an ideal ADC and 6.02 is the ratio between decibels and bits (i.e., $20log_{10}2 \approx 6.02$) [17]. A new set of values for the optical and electrical jitters were obtained by integrating the phase noise from 100 Hz to 10 MHZ to get $\Delta t_r(t) = 870$ as for the Er-doped fiber MLL and $\Delta t_e(t) = 6.4$ fs for the electric oscillator. These values were used to obtain the results for the ENOB

as a function of input frequency by implementing 4, 6, 8 and 12 slices. Also, the new values are used to calculate the NSR as a function of input frequency for the different number of slices. Figs. 1.23, 1.24, 1.25 and 1.26 show the results for the NSR, as well as the ENOB for 4, 6, 8 and 12 slices respectively, calculated in this thesis work. The number of slices is increased to evaluate the achievable performance improvement. In these plots it is revealed that, as the number of slices increases, the performance of the system approaches that of the Er-doped fiber laser limit. Also, ENOB increases as the number of slices becomes higher.

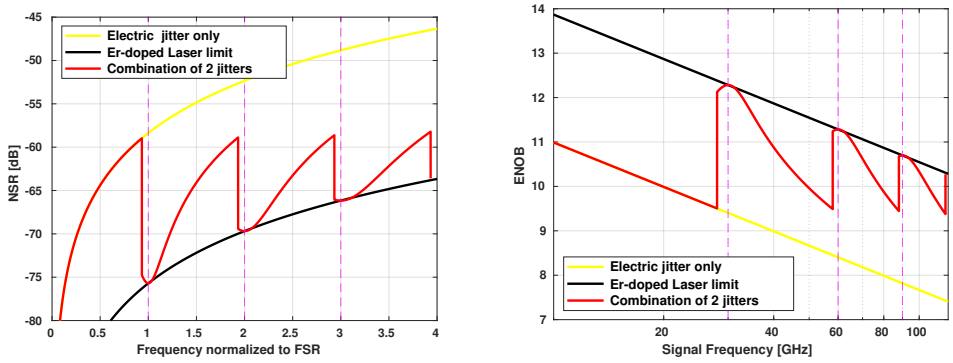

(a) (b)

Figure 1.23: (a) NSR vs frequency normalized to FSR, and (b) ENOB vs signal frequency for $\Delta t_r(t) = 870$ as and $\Delta t_e(t) = 6.4$ fs jitter values and 4 slices.

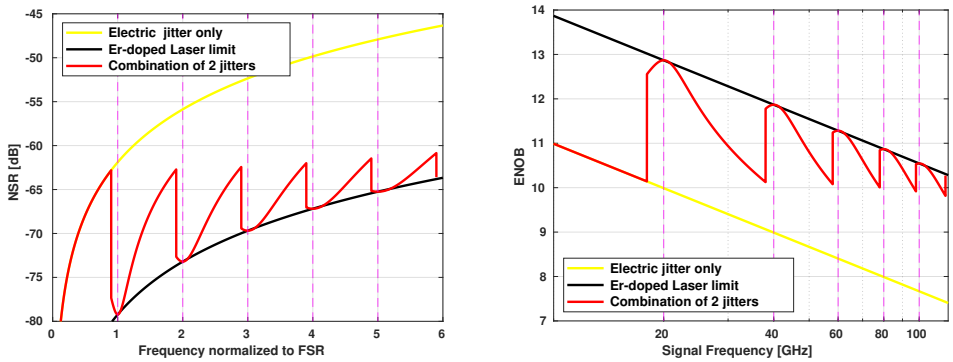

(a) (b)

Figure 1.24: (a) NSR vs frequency normalized to FSR, and (b) ENOB vs signal frequency for $\Delta t_r(t) = 870$ as and $\Delta t_e(t) = 6.4$ fs jitter values and 6 slices.

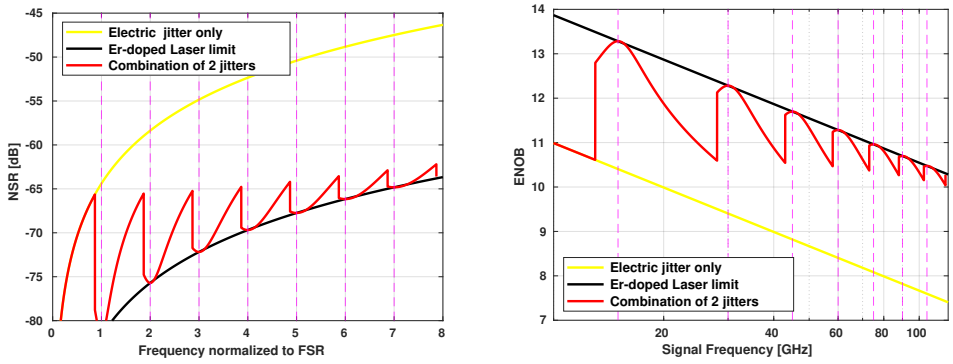

(a) (b)

Figure 1.25: (a) NSR vs frequency normalized to FSR, and (b) ENOB vs signal frequency for $\Delta t_r(t) = 870$ as and $\Delta t_e(t) = 6.4$ fs jitter values and 8 slices.

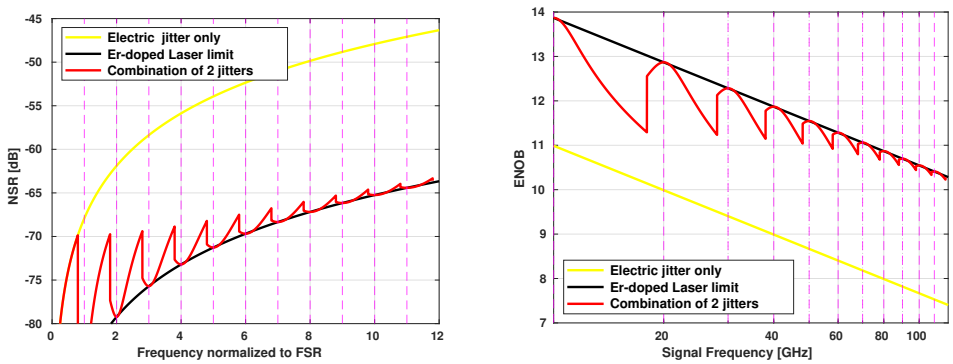

(a) (b)

Figure 1.26: (a) NSR vs frequency normalized to FSR, and (b) ENOB vs signal frequency for $\Delta t_r(t) = 870$ as and $\Delta t_e(t) = 6.4$ fs jitter values and 12 slices.

Table 1.8 shows the values of ENOB for the designed PADC as the number of slices increase. Notice that there is an improvement of 2 effective bits for implementing 4 slices relative to fully electrical ADC. As the number of slices increases, there is a corresponding improvement in the effective bits. However, increasing the number of slices comes with a higher system complexity and also suitable filters for such higher number of slices are difficult to fabricate.

Table 1.8: ENOB values for the designed PADC as number of slice increases

No. of slices	**FSR (GHz)**	**ENOB (bits)**
Electronic	-	7.4
4	30	9.4
6	20	≈ 9.8
8	15	≈ 10
12	10	≈ 10.3

1.7 Limits of energy efficiency in PADCs

Power dissipation and efficiency are pivotal in assessing ADC performance, particularly for communication systems aiming to minimize energy consumption or cost per transmitted bit [10, 55, 56]. Evaluating these parameters is crucial to understand if the high-speed and resolution capabilities of photonic ADCs can deliver practical benefits. This kind of analysis ensures that these devices can enhance network capacity and energy efficiency, especially in applications where power sensitivity and sustainability are key considerations [2, 10]. In analyzing power consumption, a generalized model incorporating the essential active components of a PADC is utilized [39, 57, 58], as shown in Fig. 1.27. This model was developed by the Authors of [10]. In this figure the components considered in the model are reported which include a pulsed laser, as the optical source, an electro-optic modulator, to encode the input signal onto the optical pulse train, and an array of N channels. Each channel consists of a photoreceiver and a sub EADC to process parallel signal subsets at reduced sampling rates. Finally, the signal is reconstructed in the digital signal processing (DSP) domain [10, 52, 58].

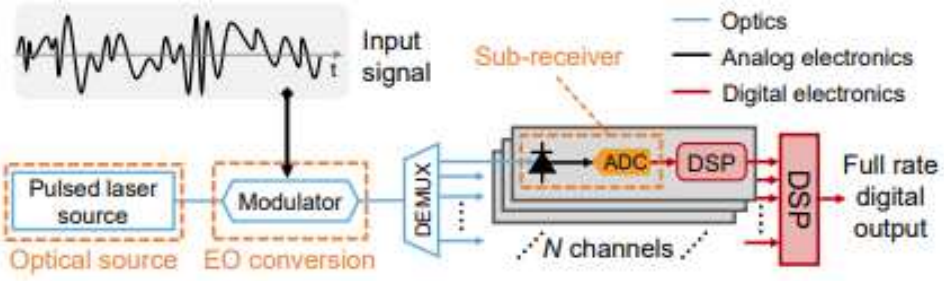

Figure 1.27: General PADC model in the context of power consumption [10]

Based on the active components depicted in Fig. 1.27, the energy per sample $\frac{P}{f_s}$ for a PADC digitizing an input signal characterized solely by its peak-to-average power ratio PAPR is given by:

$$\frac{P}{f_s} = \frac{P_{opt}}{f_s}\left[\underbrace{\frac{4\pi^2 R V_{bias}}{PAPR}}_{\text{Sub-EADCs}} + \underbrace{\frac{1}{\eta_{WPE}}}_{\text{Laser source}}\right] + \underbrace{\frac{f_s V_{\Delta f}^2}{4 Z_0 PAPR}}_{\text{Modulator}}, \tag{1.12}$$

where P_{opt} is the optical power required, f_s is the sampling rate, R is the photodiode responsivity, V_{bias} is the bias voltage, η_{WPE} is the wall plug efficiency, $V_{\Delta f}$ is the modulator V_π per Hz bandwidth, Δf is the bandwidth, Z_0 is the input impedance [10]. Notice that $f_s = 2\Delta f$ and $\Delta f V_{\Delta f}$ is the bandwidth voltage ratio usually specified by manufacturers [12]. In equation 1.12 the contributions related to the different components, such as sub-EADCs, laser source and modulator, are indicated with an under-brace. P_{opt} is also expressed as:

$$\frac{P_{opt}}{f_s} = \frac{PAPR}{4\pi^2}\left[\underbrace{\frac{h\nu}{2} SNR}_{\text{Shot noise}} + \underbrace{R\sqrt{8 C_{RX} k_B T SNR}}_{\text{Thermal noise}}\right], \tag{1.13}$$

where the contributions of shot and thermal noise are indicated with an under-brace. The required optical source power P_{opt} is determined by the power necessary to achieve a target SNR, taking into account the noise limitations imposed by shot noise at the optical frequency ν, being h the Planck's constant, and by thermal noise, where C_{RX} is the receiver capacitance, k_B is the Boltzmann constant, and T is the temperature in kelvin [10]. The most efficient PADCs are designed to operate under jitter-limited conditions, where the SNR adheres to the established upper limit of $SNR = \frac{1}{(2\pi\sigma f_{in})^2}$, with σ representing the root-mean-square jitter and f_{in} the input frequency [10, 12].

1.7.1 Results on PADC energy efficiency

Following the analysis from [10], the parameters that were set for the calculations are: $PAPR = 3$ dB, $f_s = (10^6 : 10^{12})$ Hz, $Z_0 = 50\ \Omega$, $V_{bias} = 3$ V, $R = 1$ A/W, $\nu = 192$ THz, $SNR = (10 : 80)$ dB and $T = 300$ K.

Fig. 1.28 shows the modulator limited energy per sample as a function of sampling rate for different bandwidth/voltage ratio values. Here, it is revealed that higher values of the bandwidth/voltage ratio can reduce the energy consumption.

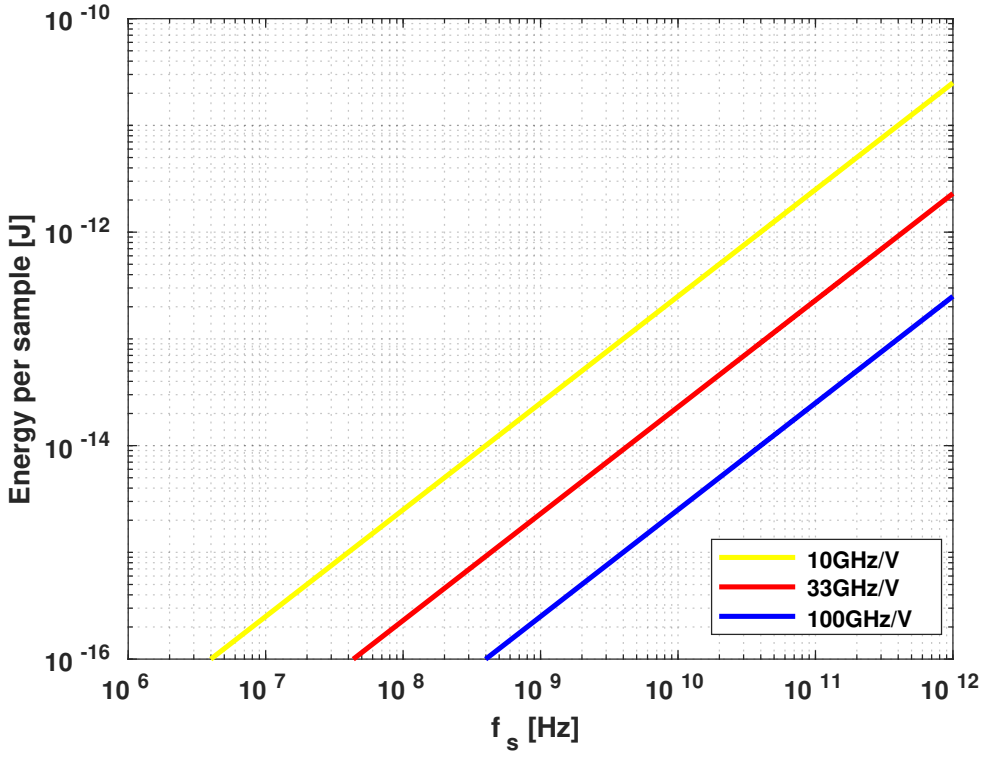

Figure 1.28: Modulator limited energy per sample as a function of sampling rate for different bandwidth/voltage ratio.

Fig. 1.29 shows the jitter limited energy per sample as a function of sampling rate for different values of the jitter. It can be seen that for a fixed jitter value, the energy per sample decreases as the sampling rate increases. Also, improvement in the jitter gives rise to high values of the energy per sample. This is because high-speed sub EADCs are required to detect higher SNR signals.

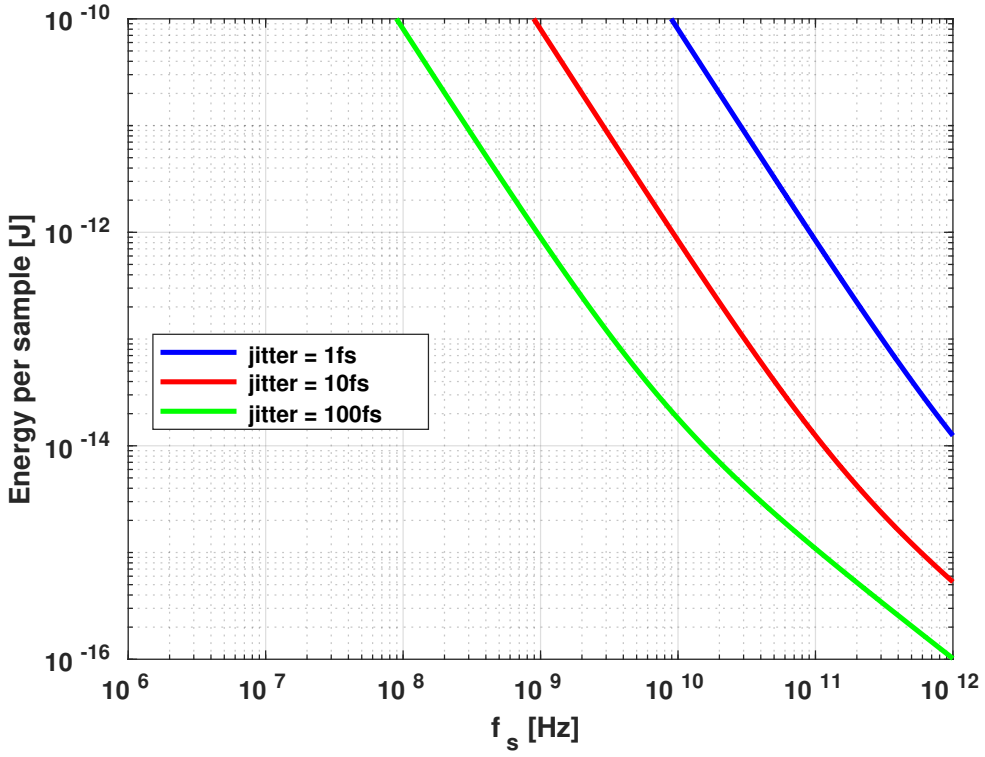

Figure 1.29: Jitter limited energy per sample as a function of sampling rate for different values of jitter.

Fig. 1.30 shows the optical power limited energy per sample as a function of SNR for different values of C_{RX} and η_{WPE}. It reveals that shot noise and thermal noise represent the primary constraints on energy per sample, with shot noise dominating at higher SNR levels and thermal noise taking precedence at lower ones.

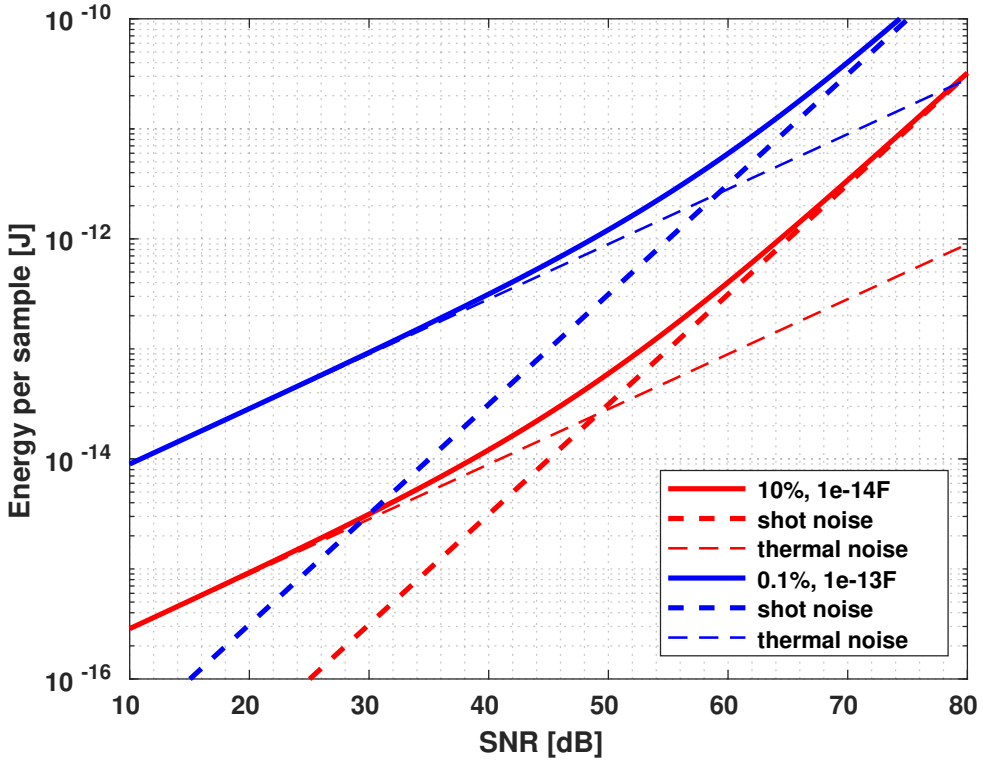

Figure 1.30: Energy per sample as a function of SNR for optical power limited scenario for different values of C_{RX} and η_{WPE}.

1.7.2 Power consumption of PADCs in selected literature

In [12] the FOM_s for four specific PADCs was estimated based on their reported frequency/SNR performance and calculated power consumption of the components used. Table 1.9 lists the parameters for these calculations for three of the references in [12], using actual data from the sources, when available, and reasonable estimates (italicized) otherwise. These studies were selected for showcasing interesting photonic ADC performance—surpassing electronic ADCs in jitter and SNR at target frequencies—and their diverse architectures, including photonic time-stretch, mode-locked laser sampling, and frequency interleaving techniques, using single and dual

frequency combs. In [12], it is explained that, as the published PADC results were likely not optimized for power consumption, the maximum potential FOM_s has been estimated using the minimum power required to achieve the reported performance. This value is denoted as 'FOM_s (potential)' in Table 1.9. Although the estimated FOM_s of PADCs, even under optimal conditions, do not surpass the best electronic ADC results for sampling rates below 10^8 Hz, analytical studies have shown that PADCs may outperform their electronic counterparts at higher frequencies. This advantage is primarily due to the exceptional jitter performance of PADCs at high frequencies.

Table 1.9: Power consumption estimates for reported PADC experiments [12]

Parameter	Ref. No. 32 from [12]	Ref. No. 8 from [12]	Ref. No. 34 from [12]
V_π	3 V	4.2 V	-
Modulation index	0.7	0.23	-
RMS drive voltage	1.48 V	0.68 V	0.59 V
input drive power	44 mW	9.3 mW	456 mW
Laser output power	10 mW	10 mW	10 mW
Wall Plug Efficiency	1%	0.81%	1%
Laser power consumption	1 W	1.23 W	1 W
Total amplifier output power	200 mW	100 mW	800 mW
EDFA Wall Plug Efficiency	10%	10%	10%
Amplifier power consumption	2 W	1 W	8 W
R	1 A/W	0.6 A/W	0.5 A/W
V_{bias}	3 V	2.25 V	2 V
Optical power per receiver	-3 dB	-8.8 dB	10 dBm
Channels	2	157	4
Receiver power consumption	3 mW	27 mW	40 mW
Sub-EADC bandwidth	5 GHz	524 MHz	80 GHz
Sub-EADC power consumption	23.6 mW	3.98 mW	249 mW
No. of Sub-EADCs	2	157	4
Total Sub-EADC power	47.1 mW	625 mW	996 mW
Total power consumption	3.1 W	2.89 W	10.5 W
SNR	45.1 dB	44 dB	15.7 dB
f_s (full bandwidth)	20 GS/s	82 GS/s	640 GS/s
Analog bandwidth	10 GHz	41 GHz	320 GHz
FOM_s	140.1 dB	145.5 dB	120.5 dB
FOM_s (potential)	176.9 dB	175.8 dB	147.3 dB

1.8 Frequency interleaving architecture exploiting Kerr soliton combs

One of the three PADCs in Table 1.9, which is the one proposed in [52], is selected and described in more detail in this thesis because of the high analog bandwidth of 320 GHz reported. This scheme exploits Kerr soliton combs and photonic-electronic spectral stitching to obtain exceptional analog bandwidth. Fig. 1.31 shows the schematic of the proposed architecture.

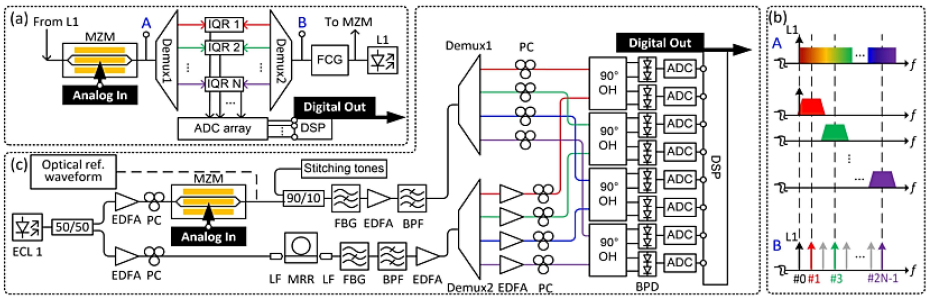

Figure 1.31: Schematic of the PADC and photonic-electronic spectral stitching proposed in [52]

In the portion of Fig. 1.31 labeled a, the ultra-broadband analog electrical signal is initially modulated onto an optical carrier using a high-speed Mach-Zehnder modulator (MZM). Then, an optical demultiplexer (DEMUX1) with a steep roll-off decomposes the broadband optical waveform into a series of spectral slices that slightly overlap, enabling spectral stitching during digital signal processing (DSP). These slices are coherently detected by an array of in-phase/quadrature receivers (IQR), with local oscillator (LO) tones sourced from a chip-scale soliton frequency comb generator (FCG). The FCG is driven by the same laser (L1) that powers the MZM, ensuring strict phase correlation between the optical carrier and all LO tones. The I and Q components of the slices are digitized using a synchronized array of EADCs. During DSP, when the signal is to be reconstructed, the digitized signals are frequency-shifted and stitched together to recreate the digital representation of the ultra-broadband input.

Overlapping spectral information is utilized to estimate the relative phase between neighboring slices, while the frequency-dependent transfer functions of the detection channels are compensated based on calibration with a known optical reference signal. The b portion of Fig. 1.31 illustrates the ultra-broadband optical waveform (A, first row), divided into tributaries (second, third, and fourth rows), along with the multi-wavelength LO comb (B, last row). The slice width corresponds to twice the FSR of the LO comb, and only odd-order tones $(1,3,...,2N-1)$ are used for coherent reception, ensuring continuous signal acquisition from DC to $2*N*FSR$.

Chapter 2

Integrated Waveguide Dispersion Measurement Using Chirped Bragg Gratings

2.1 Introduction

The accurate characterization of group delay in optical resonators is essential for advancing optical communication systems and designing efficient photonic devices. By precisely understanding group delay, engineers can optimize signal timing, reduce distortion, and enhance data transmission rates, leading to more reliable, high-performance communication networks and advanced photonic applications [59–61]. This work introduces an innovative method for measuring the dispersion of reflected light within integrated optical devices, which serves as a significant advancement in this area. By exploiting interference between light reflected from the waveguide's end facet and internal reflection points within the device under test (DUT), this method effectively creates a setup akin to a Michelson interferometer. Here, the spacing of interference fringes in the resulting signal provides a direct indication of the group delay experienced by light in the DUT. This relationship facilitates a fast and reliable means of evaluating waveguide dispersion, as variations in fringe spacing directly

reflect changes in group delay, making the technique highly sensitive to dispersion characteristics. This approach has been validated by applying it to a waveguide with a linearly chirped Bragg grating fabricated on a Silicon-on-Insulator (SOI) platform. The experimental results showed excellent alignment with the design dispersion values, underscoring the accuracy and reliability of this method in capturing the dispersion properties of complex photonic structures. Such precision is essential in fields where waveguide structures, like Bragg gratings, demand exact dispersion control for optimal device performance. This method holds significant promise for characterizing integrated photonic devices, as it provides both speed and precision. The ability to accurately assess the dispersion in complex structures directly impacts the development of advanced optical communication devices, where managing group delay and dispersion is crucial for minimizing signal degradation and maximizing bandwidth. Leveraging the square law and coupling mode theory, amplitudes from coupled wave equations have been extracted [62] to develop an analytical model that predicts the dispersion value of the fabricated device and the result aligns well with the experimental and designed value with a significant reduction in uncertainty which highlights the model's robustness and confirms its potential as a reliable and efficient alternative to traditional methods of measuring dispersion [63, 64].

2.2 Principles behind the experimental measurement

Interferometer setups, like the Michelson and Fabry-Perot configurations, can be achieved using either uniform or chirped Bragg gratings. In these designs, the grating mirrors serve as partial reflectors [65], enabling the interference effects central to the operation of these devices. Uniform gratings offer constant spacing between peaks, while chirped gratings vary in spacing to introduce controlled dispersion, allowing fine adjustment of the interference pattern. These configurations are useful in applications requiring precise optical control, particularly in fields like telecommunications, spectroscopy, and sensor technology, where they improve signal stability and response accuracy [66, 67]. Bragg gratings are optical structures characterized by a periodic variation in the refractive index along a specific axis. This periodicity

enables them to selectively reflect certain wavelengths of light while allowing others to pass through, making them integral to a variety of photonic applications. In photonic waveguides, for instance, this periodic index variation appears in the effective refractive index of the propagating mode. Due to this structured arrangement, Bragg gratings are sometimes referred to as one-dimensional photonic crystals, as they exhibit periodicity in only one dimension, typically along the z-axis [68, 69].

2.2.1 The Michelson Interferometer

The traditional free-space Michelson interferometer is an optical instrument that divides an incoming light beam into two separate paths, allowing for precise measurements through the interference of light waves. At the core of the interferometer is a partially transparent mirror, positioned at a 45° angle relative to the light source. This angled setup enables the mirror to split the incoming light into two beams, designated as Beam A and Beam B in Fig. 2.1. Beam A passes straight through the half-transparent mirror, continuing to a fixed mirror located at the end of its path. In contrast, Beam B is reflected at a right angle, directed toward a second mirror, which can be moved to adjust the length of its optical path [62]

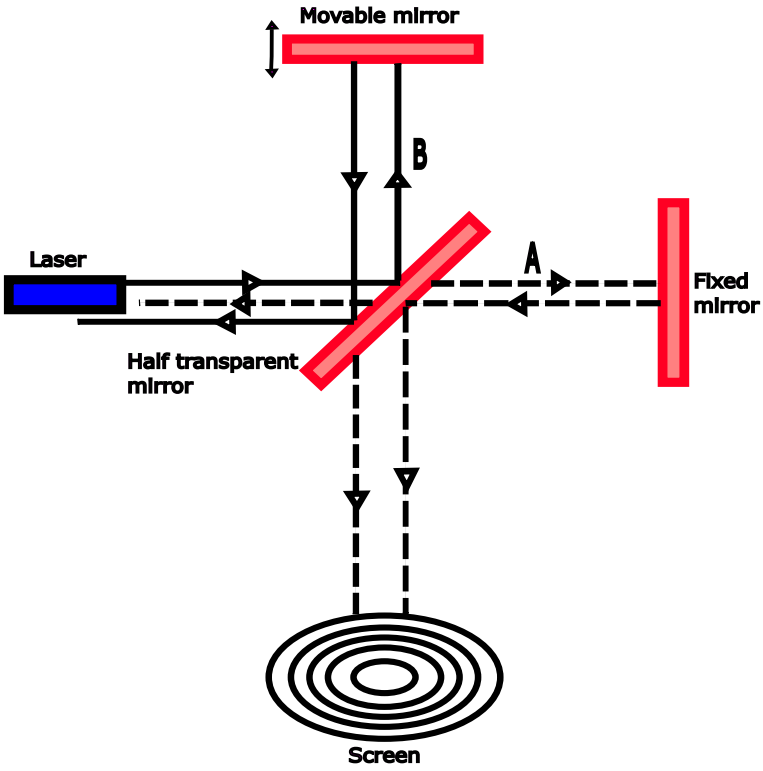

Figure 2.1: The schematic of the Michelson interferometer, showing the paths traveled by Beams A and B. An observer standing at where the screen is located will see the intensity of the combined beam in a form of interference fringes and the spacing between the fringes is determined by the position of the movable mirror

Upon reaching their respective mirrors, both beams are reflected back along their original paths toward the half-transparent mirror. As the beams return, the partially transparent mirror again divides each, allowing portions of the light from both paths to combine and reach a detection screen. The interaction of these beams on the screen produces an interference pattern, where the light waves' constructive and destructive interferences manifest as alternating bright and dark fringes. The visibility and position of these fringes are influenced by the relative path lengths of the two beams. By carefully adjusting the movable mirror, the path length of Beam B can be altered, resulting in shifts in the interference pattern. These shifts are essential for precise mea-

surements, as they correlate directly with changes in optical path length, which can be translated into distance or wavelength differences. The Michelson interferometer is valuable in various scientific applications due to this sensitivity to path differences. It can be used for measuring wavelengths, identifying changes in refractive index, and detecting minuscule displacements. In addition, this interferometer is instrumental in fields like spectroscopy, where it aids in analyzing the spectral composition of light, and in precision metrology, where it can measure distances at extremely fine scales [62, 65, 70, 71].

2.2.2 The Bragg grating structure

A Bragg grating generally consists of alternating regions with different refractive indices, creating a repetitive refractive pattern along a single direction. This structured design has the unique effect of forming photonic bandgaps—frequency ranges where light within certain wavelength bands cannot propagate through the grating [68]. As incident light interacts with this periodic structure, only wavelengths that match specific criteria related to the grating's period are reflected, while others are transmitted or allowed to propagate. This phenomenon arises due to the constructive and destructive interference of light waves as they encounter the alternating index regions, which, in turn, enables precise wavelength filtering [72–74]. The formation of photonic bandgaps in Bragg gratings is crucial for many applications, including optical filtering, wavelength stabilization, and dispersion management in optical communication systems [75]. For example, by tailoring the grating's period or the refractive index contrast between regions, designers can control the wavelength range that will be reflected, allowing for highly specific filtering capabilities. This selective reflection property of Bragg gratings is not only useful in telecommunications but also in creating distributed feedback lasers, sensors, and other integrated photonic devices [76–78]. In general, fiber Bragg gratings (FBG) are typically created by inducing a periodic variation in the refractive index along the length of an optical fiber. whilst waveguide Bragg gratings (WBG) are typically created in planar waveguides and the periodic structure is typically created through variations in the width or height of the waveguide [79, 80]. Fig. 2.2 shows a simple schematic diagram of the waveguide

Bragg gratings, with the reflections from the edge and inside indicated. Also, the grating period (Λ) is indicated.

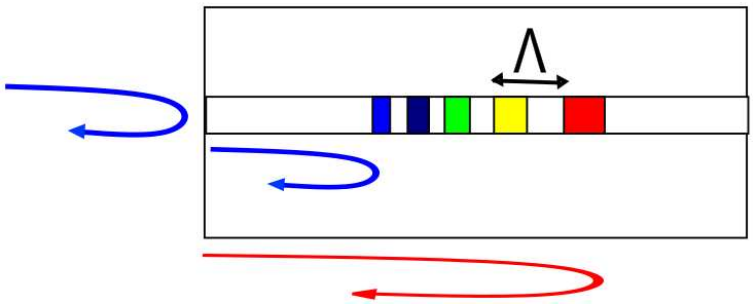

Figure 2.2: Schematic of the Waveguide Bragg gratings where the reflections from the edge and inside, as well as the grating period are indicated

The grating period of a waveguide, denoted as (Λ) is the distance over which the refractive index pattern within the waveguide repeats itself [81]. This periodic structure is fundamental in waveguide Bragg gratings, where it enables selective reflection of specific wavelengths of light. The grating period is precisely engineered to match the wavelength of interest, allowing the grating to reflect light at that wavelength while transmitting others. This property is particularly useful not only in dispersion management but also in optical filtering, wavelength division multiplexing, and other photonic applications [81, 82].

The relationship between the grating period and the reflected wavelength (λ), is given by the Bragg condition: $\lambda_B = 2n_{eff}\Lambda$. Where n_{eff} is the effective refractive index of the waveguide propagating mode [65, 79]. By carefully adjusting the grating period, designers can control the specific wavelength that is reflected. Shorter grating periods reflect shorter wavelengths, and longer periods reflect longer wavelengths [83, 84]. In advanced designs, chirped gratings—where the period varies along the length of the waveguide—can be used to reflect a broader range of wavelengths or to introduce group delay dispersion, impacting how different frequency components travel through the device [85]. This tunable feature is crucial in applications like dispersion management and compensation in high-speed optical communications [85, 86]. For

a Bragg grating waveguide of length lg, the period of the gratings; $\Lambda(z)$ (where z is the position along the length of the waveguide.) varies along the length of the waveguide causing the Bragg wavelength to change along the gratings. This is known as chirp and the Bragg condition for waveguide Bragg grating is: $\lambda_B(z) = 2n_{eff}(z)\Lambda(z)$. For a linearly periodic chirped waveguide Bragg grating, the relationship between the refractive index modulation period and the axial position along the WBG can be described as $\Lambda(z) = \Lambda_o + \frac{\Lambda_{lg}-\Lambda_o}{lg}z$. Where Λ_o is the starting period, Λ_{lg} is the ending period [65].

2.3 The Silicon On Insulator (SOI) Platform

Silicon on insulator (SOI) is a widely utilized platform for fabricating photonic waveguides, particularly those incorporating chirped Bragg gratings (CBGs) [87]. This approach leverages the high refractive index contrast between silicon and the underlying silicon dioxide layer, enabling efficient light confinement and guiding within submicron scale waveguides [88]. The SOI platform also allows for precise control over waveguide geometry, facilitating the integration of complex photonic structures like CBGs, which are essential for applications that require dispersion management and wavelength-selective filtering. The SOI platform is particularly well-suited for fabricating CBGs due to its compatibility with complementary metal-oxide-semiconductor (CMOS) processes. This compatibility enables scalable production of photonic devices with high repeatability, cost-effectiveness, and integration with electronic components [88–90]. Techniques such as electron-beam lithography or deep-ultraviolet lithography are used to define the CBG patterns on the silicon layer, and subsequent etching processes transfer these patterns to create the grating structures [91, 92]. The ability to design waveguides with customizable dispersion characteristics and spectral profiles on SOI is pivotal for advancing optical devices in areas such as high-speed optical communications, signal processing, and sensing [93–95]. In this thesis, the dispersion of a linearly chirped Bragg grating device fabricated on an SOI platform was measured experimentally, and a model was developed to predict the device's dispersion.

2.4 Details of Experimental Measurements

In this section, I introduce a novel method for measuring the dispersion of light reflected in integrated optical devices. This technique takes advantage of the interference between light reflected from the end facet of an integrated waveguide and light reflected from specific points within the device under test (DUT). This configuration essentially forms a Michelson interferometer [62, 65], where the resulting interferometric signal exhibits fringes whose spacing is directly related to the group delay within the DUT. This direct relationship enables a rapid and straightforward measurement of waveguide dispersion. I applied this method to a waveguide incorporating linearly chirped Bragg gratings, which were fabricated to be used to implement Optical Fourier Transform on a chip. I visited the lab where this work was being done, and I used this waveguide for my measurements. The name of the university where I visited is Technical University of Denmark (DTU), Department of Electrical and Photonics Engineering, high speed optical communications (HSOC) laboratory. The laboratory manager, Professor Michael Galili was my supervisor at DTU. The DUT was designed by Lars Emil Gutt, and he was using a different method to measure the dispersion of the device. We (Professor Michael Galili, Dr Peter Girouard and I) formulated the new method for measuring the dispersion of the device. By analyzing the spacing between the fringes, I accurately determined the dispersion properties of the waveguide. The experimental results showed a strong correlation with the theoretical design, confirming the reliability of the technique. This approach simplifies the process of dispersion measurement in integrated photonic devices, offering a practical and efficient tool for characterizing complex structures such as chirped Bragg gratings.

2.4.1 Description of the device under test

During the experimental measurement, the available DUTs were all fabricated on SOI platform. Due to its compatibility with the already existing Complementary Metal Oxide Semiconductor technology, the Silicon-on-Insulator platform benefits significantly from the well-established silicon semiconductor industry [96, 97]. This

advantage translates to exceptional fabrication precision, as it leverages decades of industrial expertise and advanced manufacturing techniques. Unlike newer photonic platforms that often face challenges with scalability and cost, SOI photonics benefits from the established infrastructure of a mature semiconductor industry. This advantage enables SOI photonics to achieve higher fabrication precision compared to less developed platforms. It can allow the production of photonic circuits with feature sizes as small as 10 nm at a relatively low cost, leveraging the extensive experience and technology of the existing silicon industry. This is made possible through the use of cutting-edge lithography and etching technologies that have been perfected in the silicon microelectronics sector [98]. Furthermore, the widespread adoption of silicon technology enables economies of scale, which reduce production costs. Consequently, SOI photonic circuits can be fabricated at a relatively low cost while maintaining high-quality standards. This combination of precision, cost-effectiveness, and scalability positions SOI as a superior platform for developing integrated photonic circuits, making it a preferred choice for both research and commercial applications. This technological edge facilitates the creation of complex photonic devices and systems with reliable performance and reduced fabrication overhead, fostering innovation in fields like telecommunications, data processing, and sensing. In Silicon-on-Insulator platforms, the refractive index of silica (SiO_2) is approximately 1.45 at a wavelength of 1550nm, while silicon (Si) has a significantly higher refractive index of about 3.5. This substantial contrast in refractive indices results in a strong confinement of light within the silicon waveguide core. As a result, it is feasible to fabricate extremely narrow waveguides that support high-density integration of photonic circuits. These narrow waveguides enable the design of circuits with tight bending radii, allowing for compact layouts and densely packed photonic components without incurring significant optical losses. This capability is crucial for creating efficient, high-performance photonic integrated circuits (PICs) in applications like telecommunications and data processing [99]. Bragg gratings (BGs) require significant length to achieve substantial dispersion effects. To accommodate this on a chip, the grating must be folded efficiently. This is especially critical during electron-beam lithography. Typically 500x500 μm^2 for this device under test (DUT). Consequently, a long

waveguide must be intricately folded to fit within these spatial constraints. For Bragg gratings, maintaining a uniform refractive index is crucial to prevent abrupt changes, which could arise from variations in the waveguide's curvature. Any sudden shifts could degrade the performance of the grating. To address this, the fabricated chirped Bragg grating was designed with a spiral configuration. This layout not only ensures the waveguide fits within the chip's dimensions but also avoids abrupt refractive index changes, thereby preserving the grating's optical properties and enhancing its effectiveness in dispersion management. The standard silicon height for SOI circuits is typically 220 nm. However, for the specific application of the DUT, a chip was designed on a Si wafer polished to a reduced height of 100 nm. This adjustment was made to optimize the performance for generating dispersion necessary for implementing Optical Fourier Transform (OFT) on-chip. A waveguide with a height of 100 nm and a width of 800 nm showed significantly lower optical loss, approximately 0.5dB/cm. In contrast, the standard configuration with a 220 nm height and 500 nm width exhibited a higher loss of 2.2 dB/cm. The reduction in silicon height thus enhances performance by minimizing losses, which is crucial for the intended application. This demonstrates how tailoring the physical dimensions of waveguides can lead to better device efficiency in specialized photonic applications. Fig. 2.3 shows the cross-section of the structure of the waveguide used for the measurement, where the width and the thickness are clearly indicated.

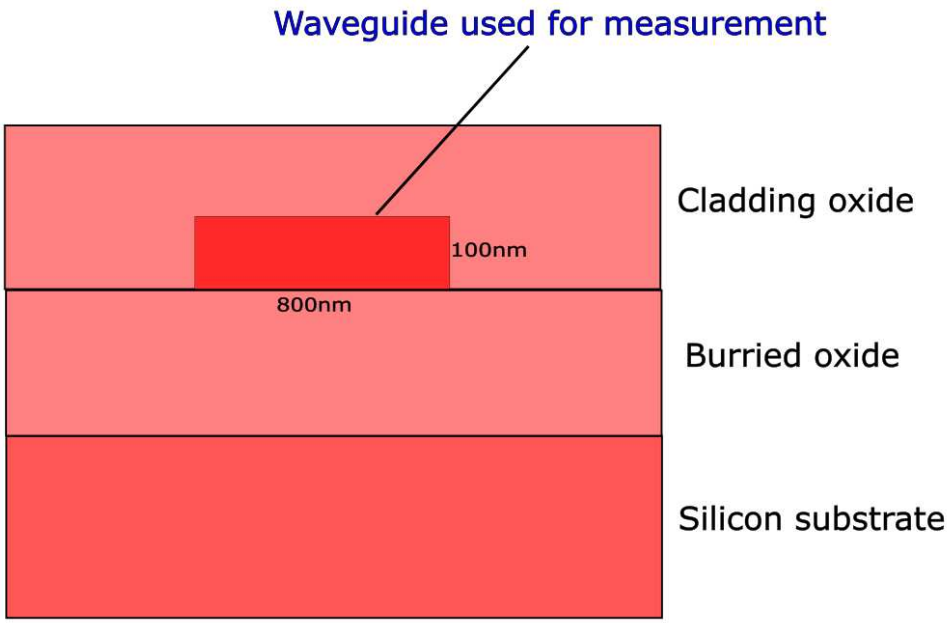

Figure 2.3: Cross-sectional view of the waveguide structure used for the measurement, with the dimensions clearly indicated. Inside the waveguide are the chirped Bragg gratings.

Other parameters of the DUT are; operating wavelength range = 1530 nm-1550 nm, length of DUT = 5248μm, design wavelength (λ_D) = 1546 nm and chirping rate = 7.5 [100]. Fig. 2.4a shows the schematic of the spiral Bragg grating waveguide which portrays how the DUT is folded. Fig. 2.4b also shows the fabricated DUT on a chip. In this figure, there are 3 chips on a wafer and each chip comprises of several spiral Bragg grating waveguide.

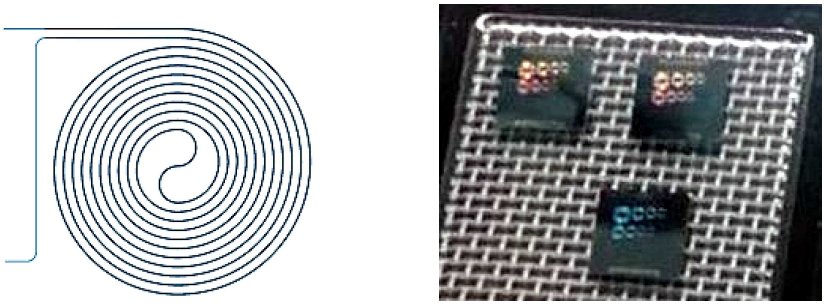

(a) (b)

Figure 2.4: (a) Schematic of the spiral Bragg grating waveguide showing how the DUT is folded. (b) A wafer on which 3 chips are mounted with each chip containing several spiral-shaped Bragg grating waveguides.

2.4.2 Experimental Measurement setup

An experimental setup was designed to measure the reflected spectrum from the DUT. This setup is shown in Fig. 2.5a. In this configuration, light is introduced into the device under test via a circulator, with the reflected light being captured by a power meter. Concurrently, a portion of the light is directed into a free-space cavity with a free spectral range of 100 MHz. The light transmitted through this cavity is detected by a photodetector. As the laser wavelength is swept, the reflected light from the DUT and the transmitted light through the cavity are simultaneously recorded on an oscilloscope. The transmission through the cavity serves as a frequency reference, utilizing its well-known resonance frequency spacing. This reference is crucial for correcting any inaccuracies in the tunable laser's wavelength sweep. The known frequency intervals from the cavity are aligned with corresponding peaks or features in the laser's output signal, ensuring precise frequency calibration and enhancing measurement accuracy. Fig. 2.5b also shows the plot of the reflected spectrum as a function of frequency from the DUT.

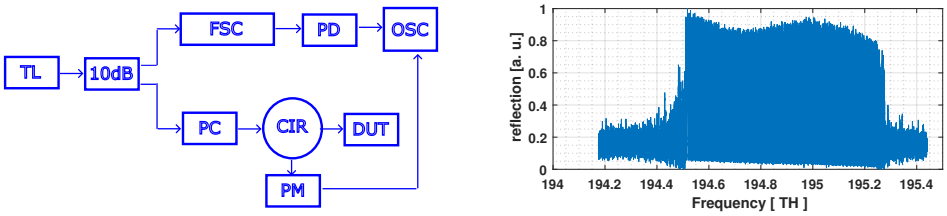

(a) (b)

Figure 2.5: (a) Experimental setup to measure the reflected spectrum. TL: Tunable Laser, 10dB: 10 dB coupler, FSC: Free Space Cavity, PD: Photo Detector, PC: Polarization Controller, CIR: Circulator, PM: Power meter, OSC: Oscilloscope, DUT: Device under test. (b) Reflected spectrum as a function of frequency [THz], obtained from the device under analysis.

Since the reflected spectrum is the combined spectrum from the edge of the DUT and points inside it, the combined power of the reflected spectrum is given as:

$$P = |E_1 \exp[i(kz + \omega t + \phi_1)] + E_2 \exp[i(kz + \omega t + \phi_2)]|^2 \tag{2.1}$$

Here, ω represents the angular frequency, $k = 2\pi/\lambda$ represents the wavenumber, λ represents the wavelength, ϕ_n represents the grating chirp and is a function of position (z) and time (t). E_1 and E_2 are the amplitudes of the two beams [62]. If we view the system as an optical resonator with a free spectral range of Δf, the group delay τ, for one round trip is inversely proportional to Δf [101]. Thus;

$$\tau = \frac{1}{\Delta f} \tag{2.2}$$

This means that by analyzing the spacing between the interference fringes, the group delay of the device under test can be accurately determined using equation (2.2)

2.5 Data Processing

The effectiveness of this model is heavily reliant on the use of the Savitzky-Golay filter (SGF), which is specifically designed to preserve peaks in data. This filter operates through discrete convolution with a fixed impulse response and was initially

developed to smooth noisy data generated from chemical spectrum analyzers. It has been shown that least squares smoothing can effectively reduce noise while preserving both the shape and amplitude of waveforms. One of the primary limitations of the SGF relates to the constraints of polynomial fitting, expressed by the inequality: $2M+1 > N+1$. where M represents the half-length of the impulse response (or window size) and N is the order of the polynomial [102]. By carefully selecting appropriate values for M and N the SGF can effectively eliminate noise while retaining the essential features of the spectral data. This capability is crucial for accurately identifying the spacing between peaks in the spectrum, allowing for better analysis and interpretation of the underlying patterns present in the measured spectra. The application of the SGF in the model demonstrates its significance in ensuring robustness and reliability in the analysis of spectral data, making it a vital tool in the field of data processing and signal analysis. Fig. 2.6a shows the zoomed-in plot of the reflected spectrum when no filter is applied. Fig. 2.6b also shows the reflected spectrum after applying the SGF.

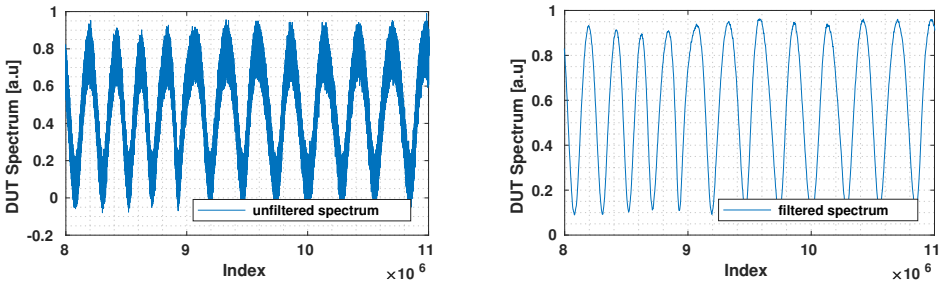

(a) (b)

Figure 2.6: (a) The unfiltered reflected spectrum. (b) The reflected spectrum after applying the SGF.

As a double-check to ensure there is no periodicity within the noise that has been filtered out, I zoomed in on a very small range of the unfiltered spectrum to verify if any periodicity remains apart from the one already identified. However, no additional periodicity was observed except for the one previously identified. Fig. 2.7 shows this.

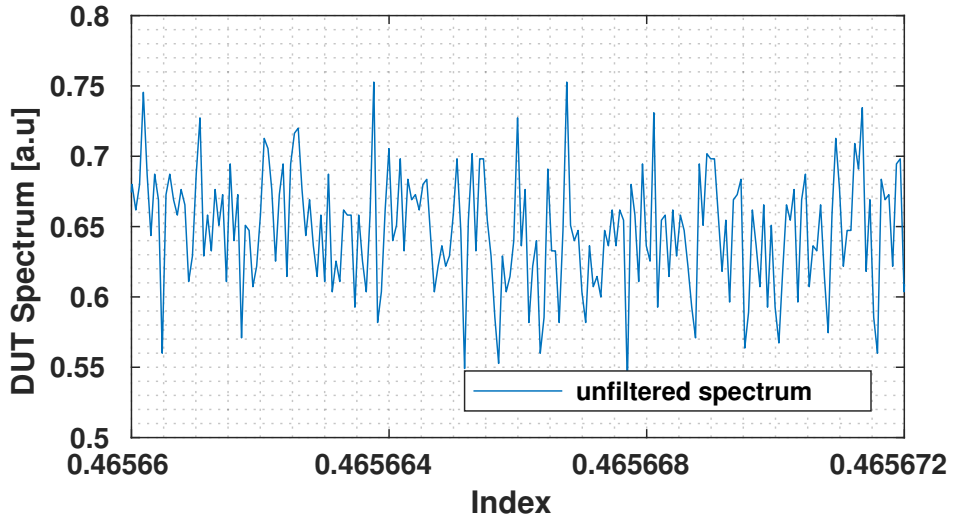

Figure 2.7: A very small range zoomed-in plot of the unfiltered spectrum showing no periodicity except the one already identified.

The instability of the tunable laser can lead to deviations in its frequency sweep, causing the recorded spectrum to inaccurately reflect the true reflection characteristics of the device under test. To address this issue, an FSC is employed. The FSC is mounted on an optical table to minimize environmental vibrations, which could otherwise alter the free space length. Additionally, the cavity's length is designed to be sufficiently long, reducing the FSR and thereby enhancing the precision of the frequency reference. The simplicity of a free-space cavity—requiring only two mirrors mounted on a table and an enclosure to block ambient light—makes it a practical choice over a fiber cavity. Fiber cavities are more prone to temperature-induced variations and require compensation for dispersion, making them less suitable for this application. In the FSC, the spacing between resonance frequencies, known as the FSR, is 100 MHz. This known FSR allows for accurate alignment of the measured frequencies with the true frequencies, correcting for any imperfections in the laser's wavelength sweep. To achieve this alignment, the peaks in the FSC spectrum must first be identified. Once located, their positions are adjusted to ensure that the spacing between them is uniform, effectively compensating for any deviations caused by the

tunable laser's instability. This process ensures that the recorded spectrum accurately reflects the device's true reflection characteristics, enhancing measurement precision. For an FSR of 100 MHz in the frequency domain, the corresponding value in wavelength domain is ~800fm at 1550nm. The length of the sweep, or the sweep width is obtained from the difference between maximum and minimum input wavelengths. This means that the number of peaks within the FSC spectrum can be calculated as: **sweep width/FSR in wavelength**. During the wavelength sweep, the laser generated a trigger signal recorded on the oscilloscope, and this marks the start and end of the sweep for precise timing. Hence, the expected peak spacing within the FSC spectrum is: **number of points within the sweep/number of peaks**. After calculating the expected peak spacing in the FSC, I used this value to verify the accuracy of the identified peaks in the FSC spectrum. By comparing the expected spacing with the measured values, I expected the differences aligned closely with the zero line, confirming the correct identification of peaks. This is depicted in Fig. 2.8a, where the peaks are correctly identified with only 3 outliers out of over $28,000$ peaks that were detected. Fig. 2.8b also shows the zoom-in plot of a portion of the first plot in Fig. 2.8a, where the peaks have been identified correctly.

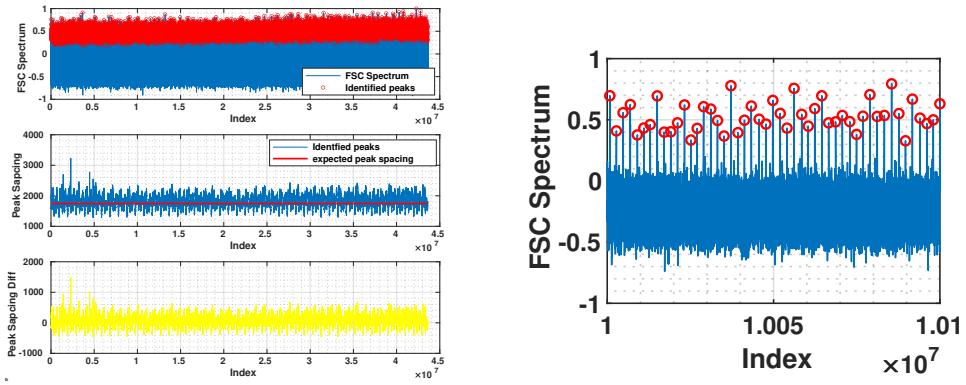

(a) (b)

Figure 2.8: (a) First plot at the top shows the FSC spectrum in blue and the identified peaks in red. Second plot in the middle shows the spacing between the peaks I identified in blue and the expected peak spacing in red. Last plot at the bottom shows the difference between the peak spacing I identified and the expected peak spacing, which is around the 0 value, suggesting that the peaks were correctly identified. (b) zoom-in on the first plot at the top in Figure 2.8a. It clearly shows the identified peaks.

After accurately identifying the peaks, the frequency axis calibration algorithm is outlined as follows:

1. Find the peaks in the FSC spectrum and their corresponding indices **(index1)**.
2. Assuming first peak is start of the wavelength sweeping, then peak frequencies **(F)** are; **0 to n*FSR**, in steps of **FSR**. Where **n= number of identified peaks**
3. Let indices of DUT spectrum **(index2) = 1 to m**, in steps of **1**, **m= length of DUT spectrum**
4. **Calibrated frequency axis = spline(index1, F, index2)**

Here, the spline function uses the third order (cubic) spline interpolation.

Fig. 2.9a presents a zoomed-in view of the FSC spectrum at various points along the frequency axis before applying frequency calibration. The plot clearly highlights the variations in peak spacing, which are attributed to the instability of the tunable laser. Figure 2.9b also displays a zoomed-in view of the FSC spectrum after frequency

calibration at various points along the frequency axis. The plot clearly demonstrates uniform peak spacing, indicating that the calibration successfully eliminated variations caused by the tunable laser's instability.

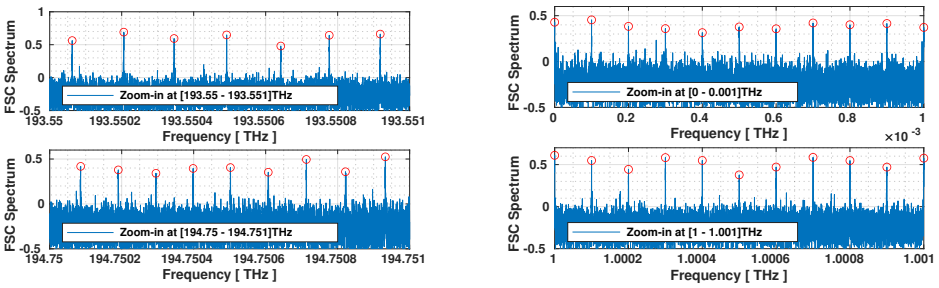

(a) (b)

Figure 2.9: (a) Zoomed-in plot of the FSC spectrum before the frequency calibration. It can be seen that the spacing between peaks in the portion of the plot at the top differs from the spacing between peaks in the portion of the plot at bottom. (b) Zoomed-in plot of the FSC spectrum after calibration, which reveals no variation in peak spacing

The zoomed-in plot of the unfiltered spectrum from the DUT is displayed in Figure 2.10a. It reveals that the rising and falling edges of the spectrum exhibit relatively low noise. While interference fringes are clearly visible, the plot also shows additional noise. Upon closer inspection, no periodicity is observed aside from the expected pattern and this is revealed in Fig. 2.7. This indicates that there are no reflections from other cavities, and the additional noise likely originates from other sources, such as the detector. Figure 2.10b also shows a zoomed-in view of the filtered DUT spectrum. A threshold was established to intersect the rising and falling edges of the spectrum. By identifying the points where these edges intersect the threshold, I calculated the midpoints between these intersections to determine the frequency positions of the peaks. This method was chosen because, despite filtering, residual features may still obscure peak detection. By measuring the spacing between the frequency positions of the identified peaks, the group delay can subsequently be calculated by

taking the inverse of the peak spacing.

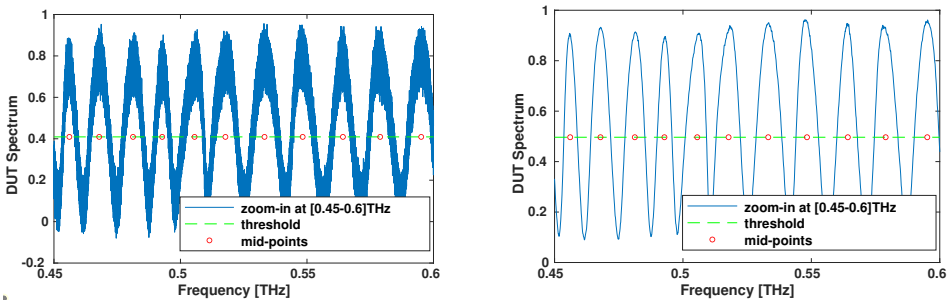

(a) (b)

Figure 2.10: (a) Zoomed-in plot of the unfiltered DUT spectrum, the threshold and the identified midpoints. (b) Zoomed-in plot of the filtered DUT spectrum, the threshold and the identified midpoints. It can be observed that peak spacing increases as frequency increases

2.6 Results of experimental measurements

Using the collected data, the aforementioned analysis procedures were employed to determine the group delay for the device. A total of seven different measurements were conducted with the experimental setup, by varying parameters such as input power, sample points, sweeping time, and scanning speed. One of the calculated group delays from the DUT is illustrated in Fig. 2.11a, where for the parameters that were set, nine different measurements were taken and plotted together on the same graph. The parameter settings used to generate Fig. 2.11a include: wavelength range = (1530–1550) nm, input power = -57 dBm, sample points = 50 MS, sweep time = 2 s, and scan speed = 11.1 nm/s. The group delay, which varies with frequency or wavelength, exhibits a linear relationship alongside additional oscillations. Typically, these fluctuations in group delay, often referred to as group delay ripple, are observed in experimental measurements [103, 104], and in the specific context of chirped Bragg gratings, the presence of perturbations in the effective index plays a significant role

in the resulting performance. This effect can be mitigated by reducing the width of the corrugations and by implementing careful apodization techniques [105]. Based on the experimental results, it was observed that the group delay exhibited significant noise at low frequencies, as anticipated. Consequently, only the linear segment of the group delay was analyzed, which corresponds to the operational range of the device where it is expected to deliver linear dispersion within a photonic integrated circuit. A curve-fitting technique was employed to apply a linear fit to this linear region of the group delay curve. For each of the seven measurements, the slope of the group delay—representing the dispersion of the device [85]—was calculated. Fig. 2.11b illustrates the plot of the linear region of the group delay along with the applied linear fit.

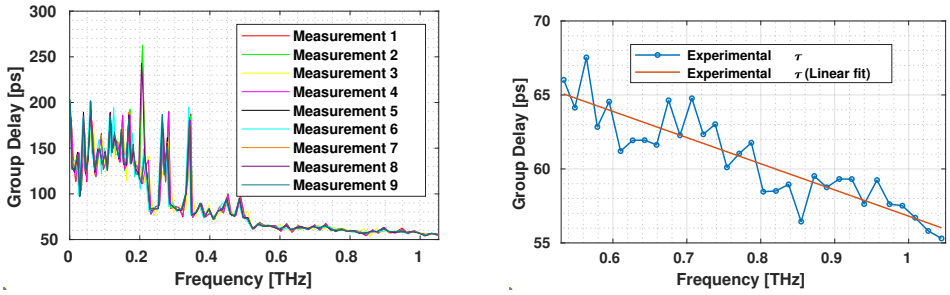

(a) (b)

Figure 2.11: (a) Calculated group delay for the DUT plotted on the frequency scale relative to the starting frequency. A total of 9 different measurements were taken on the same device and all 9 measurements plotted. (b) Linear curve fit at the linear region of Figure 2.11a

Table 2.1 presents the experimentally measured dispersion for all seven measurements taken. The Device Under Test (DUT), a linearly chirped Bragg grating, was designed to generate a dispersion of -45.9ps^2. The experimental data indicates that the dispersion of the DUT, fabricated on a silicon-on-insulator (SOI) platform, is approximately -45.5$\pm$12ps^2, closely matching the designed value. This demonstrates consistency between the experimental results and the intended design parameters.

Table 2.1: Showing the experimentally measured dispersion for all measurements taken as well as the measurement parameters that were set

Measure	Input power $[dBm]$	Input wavelength $[nm]$	Sample point $[MS]$	Sweep time $[s]$	Scan speed $[nm/s]$	Dispersion $[ps^2]$
1st	-43	1530-1550	10	5	4.4	-59.45
2nd	-57	1530-1550	10	5	4.4	-41.15
3rd	-56	1530-1550	10	5	4.4	-35.14
4th	-58	1530-1550	10	5	4.4	-35.49
5th	-55	1530-1550	10	5	4.4	-40.95
6th	-57	1530-1550	25	5	4.4	-65.79
7th	-57	1530-1550	50	2	11.1	-40.53

2.7 Analytical model for dispersion measurement

This section presents an analytical model for determining the dispersion of the Device Under Test (DUT), utilizing the Michelson interferometry effects inherent to it due to the chirped Bragg gratings. Building on the previous experimental findings, a theoretical framework was developed to simulate the group delay and calculate the corresponding dispersion value from the DUT's reflected spectrum. This model provides a comprehensive understanding of the DUT's dispersion characteristics, aligning theoretical predictions with experimental observations.

2.7.1 The theoretical model

From Equation 2.1, the combined power from the two mirrors of the Michelson interferometer is given. Using coupling mode theory (CMT), a quantitative measure of the spectral dependence on the Bragg gratings can be obtained [79]. With this notion in mind, I try to scratch the surface of CMT to derive the amplitudes E_1 and E_2. I follow closely the derivations from [79, 106] in deriving the equations for the

amplitudes. Usually, Bragg gratings in fiber is achieved through the exposure of the core of the fiber to periodic pattern of intense ultra violet light [79]. In the case of waveguides, this can be achieved by modifying the width or height of the waveguide. For simplicity, this results in a perturbation in the effective index (n_{eff}) of the mode under consideration and this perturbation is given by:

$$\delta n_{eff}(z) = \overline{\delta n}_{eff}(z)\left[1 + v\cos\left(\frac{2\pi}{\Lambda}z + \phi(z)\right)\right] \tag{2.3}$$

Λ represents the nominal grating period, v represents the fringe visibility, and $\overline{\delta n}_{eff}(z)$ represents the local detuning index change spatially averaged over a grating period. δ is known as the detuning [79, 107]. For an ideal mode approximation to CMT, it can be assumed that the transverse component of the electric field $\overrightarrow{E}_t(x,y,z)$ is written as a superposition of the ideal modes labeled j. Hence;

$$\begin{aligned}\overrightarrow{E}_t(x,y,z) = \Sigma_j\left[A_j(z)\exp(i\beta_j(z)) + B_j(z)\exp(-i\beta_j(z))\right] \\ \overrightarrow{U}_{jt}(x,y)\exp(-i\omega t)\end{aligned} \tag{2.4}$$

A_j and B_j are the slowly varying counter propagating amplitudes for the j^{th} mode and $\overrightarrow{U}_{jt}(x,y)$ is the transverse mode field. In the ideal mode regime, the modes are orthogonal and so there is no exchange of energy. However, the presence of dielectric perturbation will mean that the modes can couple such that the amplitudes A_j and B_j for the j^{th} mode will evolve along the z-axis as:

$$\begin{aligned}\frac{dA_j}{dz} = i\Sigma_k A_k\left(K^{\text{t}}_{\text{kj}} + K^{\text{z}}_{\text{kj}}\right)\exp[i(\beta_k - \beta_j)z] + \\ i\Sigma_k B_k\left(K^{\text{t}}_{\text{kj}} - K^{\text{z}}_{\text{kj}}\right)\exp[-i(\beta_k + \beta_j)z]\end{aligned} \tag{2.5}$$

$$\begin{aligned}\frac{dB_j}{dz} = -i\Sigma_k A_k\left(K^{\text{t}}_{\text{kj}} - K^{\text{z}}_{\text{kj}}\right)\exp[i(\beta_k + \beta_j)z] + \\ i\Sigma_k B_k\left(K^{\text{t}}_{\text{kj}} + K^{\text{z}}_{\text{kj}}\right)\exp[-i(\beta_k - \beta_j)z]\end{aligned} \tag{2.6}$$

In (2.5) and (2.6), K^{t}_{kj} represents the transverse coupling coefficient and is given as:

$$K^{\text{t}}_{\text{kj}} = \frac{\omega}{4}\int\int_{\infty} dxdy\Delta\varepsilon(x,y,z)\overrightarrow{U}_{jt}(x,y)\overrightarrow{U}^{*}_{jt}(x,y) \tag{2.7}$$

Where $\Delta\varepsilon$ represents the perturbation to the permittivity. K^{z}_{kj} represents the longitudinal coupling coefficient. Usually, $K^{z}_{kj} << K^{t}_{kj}$ and is neglected. Assuming the induced index change $\delta n(x,y,z)$ is uniform across the core and negligible outside the core, then the core index can be described by an expression similar to (2.3). Where $\overline{\delta n}_{eff}(z)$ is replaced with $\overline{\delta n}_{core}(z)$. We can therefore define two new coefficients:

$$\sigma_{kj}(z) = \frac{\omega n_{core}}{2}\overline{\delta n}_{core}(z)\int\int_{\infty} dxdy\Delta\varepsilon(x,y,z)\overrightarrow{U}_{kt}(x,y)\overrightarrow{U}^{*}_{jt}(x,y) \tag{2.8}$$

and

$$q_{kj}(z) = \frac{v}{2}\sigma_{kj}(z) \tag{2.9}$$

$\sigma_{kj}(z)$ represents the "DC" coupling coefficient and $q_{kj}(z)$ represents the "AC" coupling coefficient. The DC coupling coefficient is the self-coupling coefficient, which is also called local detuning. The AC coupling coefficient is also the local grating strength [107]. From these two new coefficients, the general coupling coefficient becomes:

$$K^{t}_{kj}(z) = \sigma_{kj}(z) + 2q_{kj}(z)\left[\cos\left(\frac{2\pi}{\Lambda}z + \phi(z)\right)\right] \tag{2.10}$$

In Bragg gratings, the dominant interactions occur around wavelength for which there is reflection of a mode of amplitude $A(z)$ into identical counter propagating mode of amplitude $B(z)$. The evolution of A_j and B_j along the z-axis can therefore be simplified by retaining only the terms involved in the interactions with the amplitudes of the particular mode [79]. The resulting equations are written as:

$$\frac{dE_1}{dz} = i\hat{\sigma}E_1(z) + iqE_2(z) \tag{2.11}$$

and

$$\frac{dE_2}{dz} = -i\hat{\sigma}E_2(z) - iq^{*}E_1(z) \tag{2.12}$$

Here, q represents the "AC" coupling coefficient defined in equation 2.9, q^{*} represents the complex conjugate of q, the amplitudes E_1 and E_2 are defined as:

$$E_1 \equiv A(z)\exp\left(i\delta z - \frac{\phi}{2}\right) \tag{2.13}$$

and

$$E_2 \equiv B(z)\exp\left(-i\delta z + \frac{\phi}{2}\right) \tag{2.14}$$

$\hat{\sigma}$ is the general "dc" self-coupling coefficient $\equiv \delta + \sigma - \frac{1}{2}\frac{d\phi}{dz}$ and

$$\delta \equiv \beta - \frac{\pi}{\Lambda} = 2\pi n_{eff}\left(\frac{1}{\lambda} - \frac{1}{\lambda_D}\right) \tag{2.15}$$

λ_D represents the design wavelength. Having obtained the expressions for E_1 and E_2, equations 2.13 and 2.14 are substituted into equation 2.1 and the analytical reflected spectrum induced by the chirped Bragg gratings can be generated. This is a simple model which has first been derived for describing the amplitude of the spectrum. Here, it is assumed that the longitudinal component of the coupling coefficient is significantly smaller than that of the transverse component. In fibers, this assumption can safely be made; however, from [108] it is not always true for integrated waveguides with rectangular profiles and high refractive index contrast between the core and cladding. This simplification, however, allows for the development of an intuitive model that also agrees well with the experimental results. Parameters used to obtain the analytical spectrum are shown in Table 2.2.

Table 2.2: showing parameters for simulation

Parameter	Value	Remarks
L	5248μm	Length used to fabricate DUT
ϕ	7.5	grating chirp used to fabricate DUT
n_{eff}	2.8	
λ	1530 nm-1550 nm	Wavelength sweeping range during experiment
λ_D	1550 nm	Design wavelength for DUT
z	$L-200$ nm	Total length for Gratings

2.8 Numerical Model Results

Using the parameters in Table 2.2, the analytical reflected spectrum is generated and Fig. 2.12a shows the plots of both the experimental and analytical spectra in the unfiltered case. Fig. 2.12b also shows the plots of the experimental and analytical spectra after the SGF is applied.

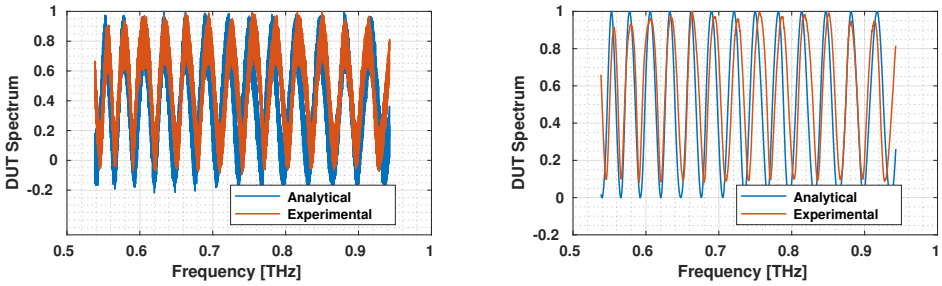

(a) (b)

Figure 2.12: (a) The unfiltered experimental and analytical spectra on the same plot. (b) The filtered experimental and analytical spectra on the same plot

The analytical group delay is calculated using Equation (2.2), and the dispersion calculated by finding the slope for the linear fit curve. The experimental and analytical group delays are plotted on the same graph, as well as their respective linear fits and this is shown in Fig. 2.13. The slope on the analytical group delay curve, which represents the dispersion of the DUT for the analytical approach is found to be -45.6$\pm$0.7ps^2, which is also in very good agreement with the design value of the DUT.

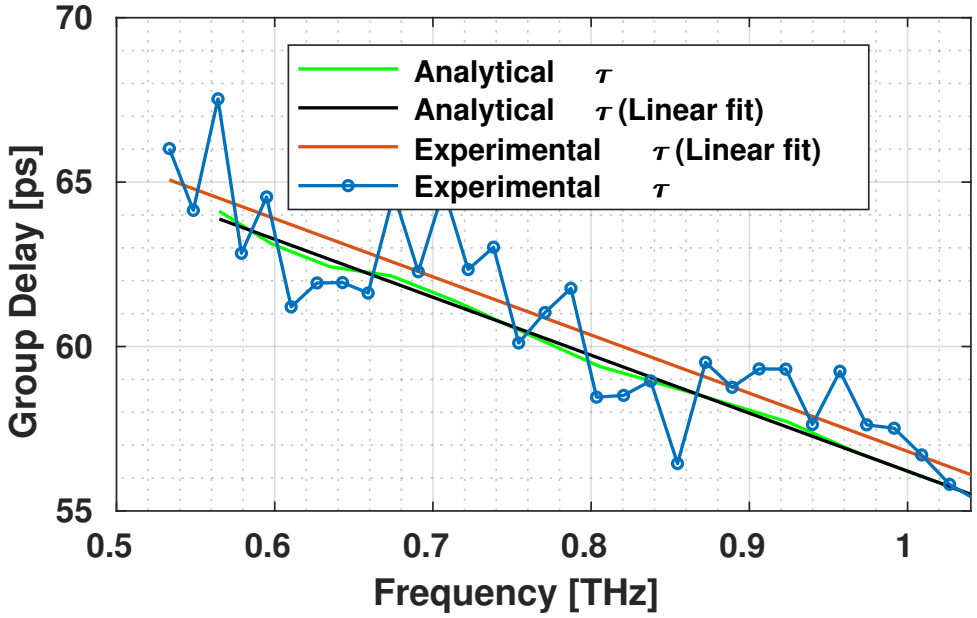

Figure 2.13: Calculated experimental and analytical group delay

Table 2.3: showing the calculated experimental and analytical group delays as well as the design value of the DUT

Design Value	Experimental Value	Analytical Value
-45.9[ps^2]	-45.5$\pm$12[ps^2]	-45.6$\pm$0.7[ps^2]

This method of calculating waveguide dispersion is fast, and from the results in Table: 2.3, the approach is accurate and reliable. It is fast because, the established method of calculating dispersion that is employed in [64] uses programmable optical filter, whose example is the waveshapers from Finisar. Based on the datasheet in [109], the waveshapers have a settling time of 500 ms, (this means that each data point will take a minimum of 500 ms to record) and the minimum step size is 8 pm. In the specific method that is being referred to for the OFT, at least 4 filter shapes need to be applied. The wavelength range is 1530 nm–1550 nm = 20 nm. So total point is (20 nm/8 pm)

× 4 and the total time is (20 nm/8 pm) × 4 × 0.5 s = 5000 s. Which is approximately 1 hour 23 minutes. For my measurement technique, the sweeping time is 5 s, hence, the method is significantly faster than the established method. The method is also reliable because of the step-by-step data processing procedures adopted. Finally, even though simplifications were made for the derivation of the analytical model, the result is in a very good agreement with the design value and hence the approach is accurate.

2.9 Application Area

The temporal spreading of a pulse in a dispersive medium is analogous to the spatial diffraction of a beam or wave passing through an aperture. In both cases, the spreading effect arises from the varying phase velocities encountered within the medium for temporal dispersion or across the aperture in spatial diffraction. This leads to broadening over time or space as different components propagate at distinct velocities, resulting in the separation of frequencies or spatial components, respectively. The spreading due to dispersion can be particularly impactful in optical communication systems, where a temporally broad pulse can lead to signal overlap and interference, limiting data transmission rates and accuracy. Conversely, temporal compression of a pulse by a Quadratic Phase Modulator parallels the spatial focusing of a beam by a lens. A lens converges light rays to a focal point by introducing a phase shift across its surface, with varying phase delay that causes all rays to converge. Similarly, a Quadratic Phase Modulator compresses a pulse by applying a quadratic phase profile, which accelerates or decelerates different frequency components of the pulse. This phase manipulation aligns the frequency components in such a way that they arrive at the same point in time, effectively focusing the pulse temporally. In optical systems, this pulse compression technique is essential for high-speed signal processing, where brief, high-energy pulses are required for tasks such as sampling, data acquisition, and communication in both fiber-optic and photonic circuits. Thus, these parallel concepts of spreading and focusing are fundamental to managing temporal and spatial characteristics in optical systems. [110]. This concept of Space-Time duality is being applied in integrated optics, for the implementation of an Optical

Fourier Transform on a chip. This duality allows time-domain signals to be manipulated in a manner similar to spatial-domain signals, leveraging dispersive properties to transform pulse profiles and analyze frequency components. For this application, a dispersive medium, such as the DUT, is essential for generating the necessary temporal dispersion, which enables the Fourier transform by altering the phase and group velocity of different frequency components. Using this model, the dispersion of the DUT can be calculated effectively because the medium reflects a sufficient portion of the optical spectrum, creating a broad enough range of reflected spectral components to enable straightforward analysis. By observing the spectrum of this reflected light, the dispersion characteristics, including group delay, can be calculated quickly and accurately. However, if the DUT or other medium permits too much optical power to pass without reflection, the reflected spectrum will be limited. In such cases, the reduced amount of spectral data limits the ability to analyze group delay, as there is insufficient reflected power to facilitate an accurate dispersion calculation. This limitation underscores the need for a carefully designed dispersive medium in on-chip Fourier transform applications. Thankfully, chirped Bragg gratings usually have enough reflection to use this measurement technique.

Chapter 3

Modeling of photonic devices

3.1 Introduction

This chapter focuses on the numerical modeling of integrated optical devices using the finite element method (FEM). Silicon photonics (SiPh) platform is chosen because it utilizes mature CMOS fabrication techniques, reducing production costs and enabling scalability. It also combines photonic components (e.g., waveguides, modulators) with electronic circuits on a single chip, reducing size and complexity. Again, it enables ultra-fast data transmission over long distances, making it ideal for data centers and telecommunication networks. SiPh platform also has the advantage of high index contrast between core and cladding. Lastly, the main device used for the measurement of dispersion in this thesis was fabricated on SiPh platform.

3.2 Strip and rib Waveguides

Almost any transparent material with a refractive index higher than that of glass can be deposited onto an oxidized silicon substrate and configured as a waveguide. However, to maintain compatibility with CMOS processing, certain geometries have become standard. Among these, high-confinement waveguides created from the active device layer of a silicon on insulator (SOI) wafer are the most prevalent, offering

efficient light confinement and integration potential [111]. In silicon photonics, several waveguide types are used to manage different functionalities. The two primary types are the strip and the rib waveguide. The strip waveguide is favored for routing light because it enables tight bend radii, making it suitable for compact designs. On the other hand, the rib waveguide is often used in electro-optic devices, such as modulators, because it allows for easier integration of electrical connections to the waveguide, facilitating efficient modulation and interaction with electronic components. Each waveguide type thus offers specific advantages tailored to its role within photonic circuits [111, 112]. Fig. 3.1 shows the cross-sectional view of the strip and rib waveguides on an SOI wafer.

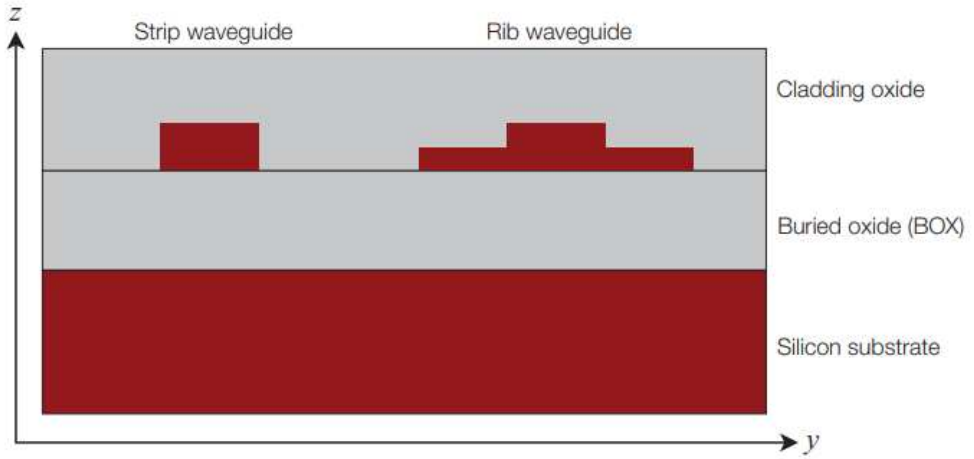

Figure 3.1: Two main waveguides used in SiPh. On the left is the strip and on the right is the rib waveguide. [111]

Using COMSOL Multiphysics software and following the simulation procedures from [111], the effective index n_{eff}, the group index n_g and the dispersion parameter D of the mode propagating through these waveguides, as functions of the wavelength and the waveguide width have been investigated as a starting point of my PhD activities.

3.2.1 Effective index analysis

In optical waveguides, a guided mode with a certain wavelength travels at a slightly different speed due to the effective index n_{eff}. Due to the way different waveguide dimensions influence the confinement of the optical mode within the core, the effective index of a waveguide depends significantly on the waveguide width as well. Simulations are done to analyze these aspects, with **waveguide dimension of 220×550 nm** for strip waveguide, and for rib waveguide with a **90 nm slab thickness**. In the simulation, the value of the silicon refractive index inside the core was made to vary accordingly with wavelength, using the Lorentz model. The index is given as:

$$nSiliconL = \sqrt{\varepsilon + \frac{\varepsilon_{Lorentz}\omega_0^2}{\omega_0^2 - 2i\delta_0 2\pi c/\lambda - (\frac{2\pi c}{\lambda})^2}} \tag{3.1}$$

$\varepsilon = 7.9874$, $\varepsilon_{Lorentz} = 3.688$, $\omega_0^2 = 3.9328e15$ and $\delta = 0$. The value of the refractive index inside the cladding was set to 1.444, which is the value silica exhibits at a wavelength of 1550 nm [111]. Detailed explanation of the expression for the Lorentz model and the choice of coefficients can be found in [111]. Fig.3.2a shows the cross-section of the strip waveguide where the field distribution is confined inside the core. Fig.3.2b also shows the cross-section of the rib waveguide with field distribution confined in the core.

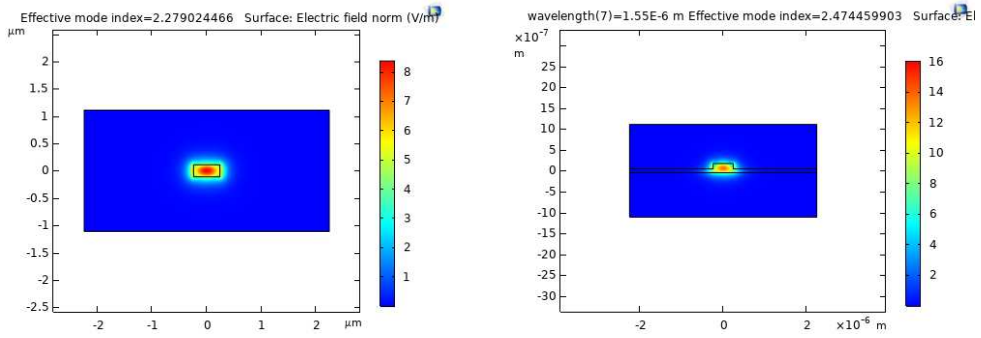

(a) (b)

Figure 3.2: (a) Cross-section of the strip waveguide with field distribution inside the core (b) Cross-section of the rib waveguide with field distribution inside the core

Fig. 3.3a shows the effective index of the fundamental mode against wavelength for strip waveguide, whilst Fig. 3.3b shows that of the rib one. From the two figures, it can be observed that the rib waveguide gives relatively higher confinement and also, as the waveguide width increases, more power is confined in the core.

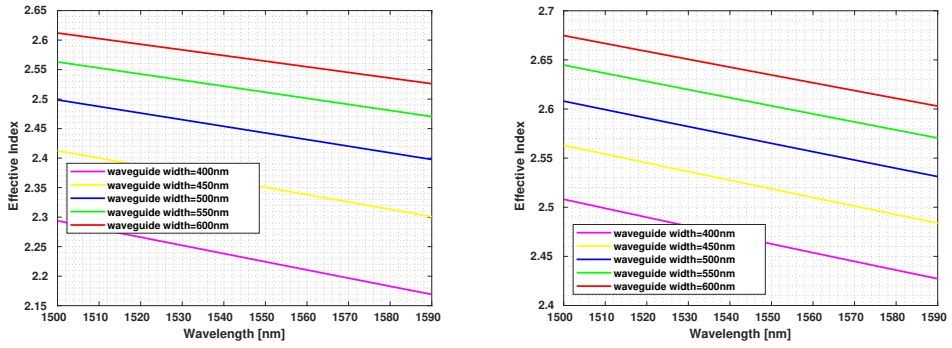

(a) (b)

Figure 3.3: Effective index vs wavelength for different waveguide widths for (a) the strip and (b) for the rib waveguide

Fig. 3.4a shows the plot of the effective index against the waveguide width at a fixed

wavelength of 1550 nm for the strip waveguide. This can aid in determining the single-mode condition for the waveguide. Here, the refractive index inside the core was set to 3.4734 (thus, the refractive index of silicon using the Lorentz model at λ =1550 nm) whilst that of the cladding was set to 1.444. From Fig. 3.4a it can be observed that only the modes with effective index higher than the cut-off value of 1.444 are guided. Again, to obtain a single mode with TE polarization at 1550 nm, a strip waveguide with a silicon thickness of 220 nm and width of 440 nm is required. In this case, the waveguide supports one TE and one TM mode. For wider waveguide that is with width >480 nm, a second TE mode is present, and above 660 nm, the width of a second TM mode appears. Also, when the waveguide width is approximately 660 nm, there is a mode crossing; that is the first TM mode is no longer the second supported mode of the waveguide, since there is a higher order mode of the TE appearing. Fig. 3.4b also shows the plot of the effective index against the waveguide width at a fixed wavelength of 1310 nm for the strip waveguide.

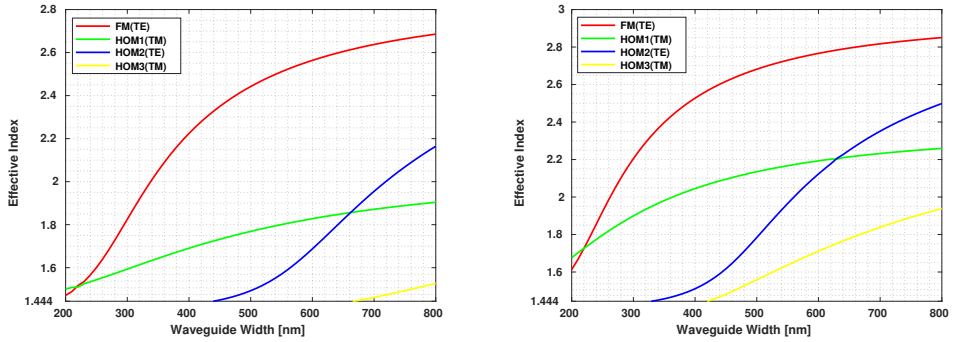

(a) (b)

Figure 3.4: Effective index vs width for modes (a) at 1550 nm and (b) at 1310 nm

3.2.2 Group index analysis

The speed at which the energy or the modulation of an optical pulse propagates through an optical component is referred to as the group velocity v_g [113]. This velocity differs from v_p, as it pertains to the envelope of the pulse, which carries

the information being transmitted. The group velocity is determined by the factor called the group index n_g, which is defined as $n_g(\lambda) = n_{\text{eff}}(\lambda) - \lambda \frac{dn_{\text{eff}}(\lambda)}{d(\lambda)}$. Thus $v_g(\lambda) = \frac{c}{n_{\text{g}}(\lambda)}$ [111].

With the same parameters for the strip and rib waveguides, simulations are done to understand the dependence of the group index on the wavelength. Fig. 3.5a shows the plot of the group index against the wavelength for the strip waveguide, which reveals that generally, the group index in strip waveguides tends to remain relatively stable across the wavelength range because strip waveguides typically exhibit strong confinement of the optical mode. This confinement means that changes in wavelength produce less significant variation in the effective index and, consequently, in the group index. Thus, an almost constant group index across wavelengths for each waveguide width is expected. Fig. 3.5b also shows the plot of the group index against the wavelength for the rib waveguide. It can be observed that rib waveguides usually show greater sensitivity in their group index to changes in wavelength. As the wavelength increases, the effective index tends to decrease due to reduced mode confinement. This reduced confinement allows the optical mode to extend further into the cladding, which results in a gradual decrease in the group index as wavelength increases. This effect is more pronounced in rib waveguides compared to strip waveguides, given the rib structure's partially confined nature.

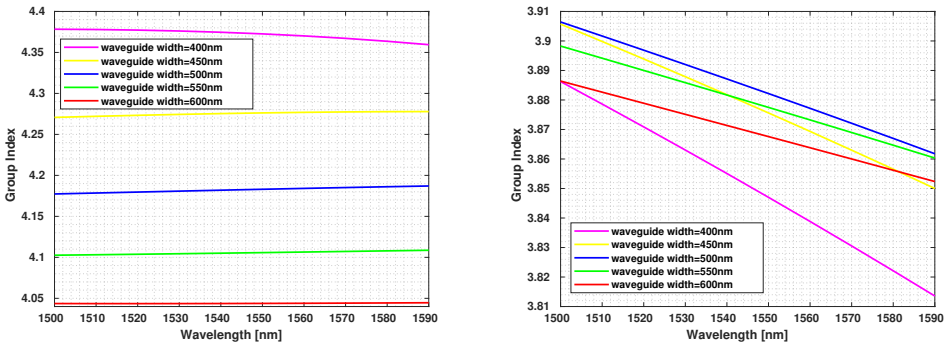

(a) (b)

Figure 3.5: Group index vs wavelength for (a) the strip waveguide and (b) the rib waveguide as a function of the wavelength for different waveguide widths.

3.2.3 Dispersion parameter analysis

In dispersive materials, the effective index varies with wavelength. This means that different wavelength components of the pulse travel at different phase velocities, leading to what is known as group velocity dispersion GVD, or the second-order dispersion β_2. Dispersion causes pulse broadening as shorter and longer wavelengths spread apart over distance, a process that influences pulse stability in optical communication and is managed through careful design of waveguides and materials in photonic circuits. β_2 is an important parameter in understanding the spreading of optical pulses traveling down a waveguide, and it can be obtained through a factor related to the effective index. This factor is known as the dispersion parameter D and its defined as: $D(\lambda) = -\frac{\lambda}{C}\frac{d^2 n_{\text{eff}}}{d\lambda^2}$. Thus $\beta_2 = \frac{\lambda^2}{2\pi C}D(\lambda)$. Simulations are done to understand the behaviour of the dispersion paramater as a function of the wavelength. The refractive index of the cladding, made of silica was calculated using the Sellmeier equation. The index is given as:

$$nSilica = \sqrt{1 + \frac{0.6961663\lambda^2}{\lambda^2 - (0.0684043)^2} + \frac{0.4079426\lambda^2}{\lambda^2 - (0.1162414)^2} + \frac{0.8974749\lambda^2}{\lambda^2 - (9.896161)^2}} \tag{3.2}$$

A detailed explanation of the Sellmeier equation can be found in [114]. The refractive index of the core, made of silicon was calculated using equation 3.1
Fig. 3.6a shows the plot of the dispersion parameter against wavelength for different waveguide widths. It can be observed that for strip waveguide, narrower widths lead to high slope of the dispersion parameter curve as wavelength changes. As waveguide width increases, the dispersion gradually becomes constant. Fig. 3.6b also shows the plot of the dispersion parameter against wavelength for the rib waveguide. The plot reveals that rib waveguide gives more stabilized dispersion curves across the entire wavelength range. Also, the rib waveguide gives dispersion in the anomalous region, where higher frequency components travel at a faster speed [113].

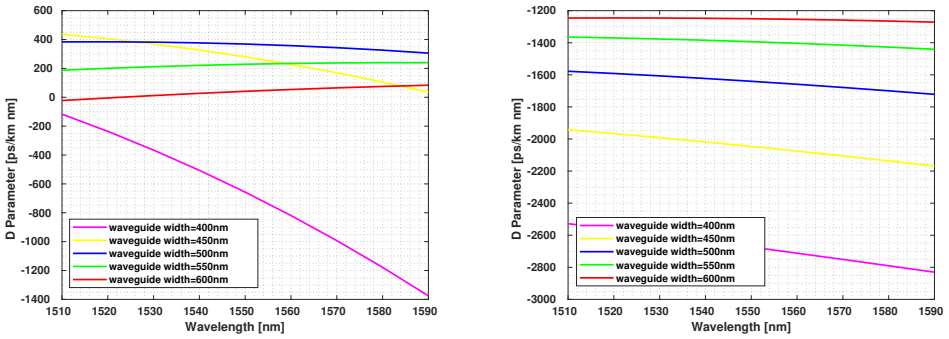

Figure 3.6: Dispersion parameter vs wavelength for the (a) strip and (b) the rib waveguide.

3.3 Directional couplers

The concept of the evanescent field is central to understanding coupling between waveguides in integrated photonic circuits. When light propagates through a waveguide, most of the optical energy is confined within the core, but a small portion of the electromagnetic field, known as the evanescent field, extends into the surrounding cladding [115]. This evanescent field decays exponentially away from the waveguide, but it can still extend a short distance beyond the core boundary [116]. When

two waveguides are brought close enough—typically within a few hundred nanometers—these evanescent fields can overlap. This overlap allows light to couple from one waveguide to the other because the optical mode in one waveguide can "see" the other waveguide through the evanescent field. Thanks to this interaction, energy can transfer between the two waveguides in a process known as evanescent coupling [115]. This principle is usually exploited in directional couplers.

At the functional level, couplers can also be seen as power dividers, where an input power P_{in} can be split into two outputs. Assuming P_{in} is 100%, and if x amount of power is coupled into the first waveguide, then the fraction of power to the other waveguide is: $(1 - \frac{x}{100})P_{in}$ [117]. Fig. 3.7 shows the structure of the directional coupler. It is a key component in photonic systems used to combine or split (if it is used as a power divider) optical signals. It consists of two waveguides placed in close proximity, allowing their evanescent fields to overlap and enabling light to couple between them [111]. The region marked with the red rectangle is called the coupling region. The length of the coupling region is called coupling length L_c. The gap between the waveguides within the coupling region is called the coupler gap G_c. When a guided mode reaches the coupling region, the distance that it travels before coupling from one waveguide to the other is called the cross over length L_x. The amount of light that couples from one waveguide to the other depends on L_c, G_c, and the index contrast [118]. Coupled mode theory (CMT) can be used to analyze and understand how the amplitude of light in each waveguide evolves along the coupling length. Assuming lossless coupler, the behaviour of power transferred from one waveguide to the other can be represented as: $\sin^2(k_c L_c)$ whilst the proportion of power remaining in the original waveguide is represented as: $\cos^2(k_c L_c)$, where k_c is the coupling coefficient which depends on L_c and G_c [111, 119]. The value of k_c can be determined through "supermode" analysis, which involves numerically calculating the effective indices, n_{eff1} and n_{eff2}, of the two primary eigenmodes of the coupled waveguides. These two modes are known as even mode and odd mode.

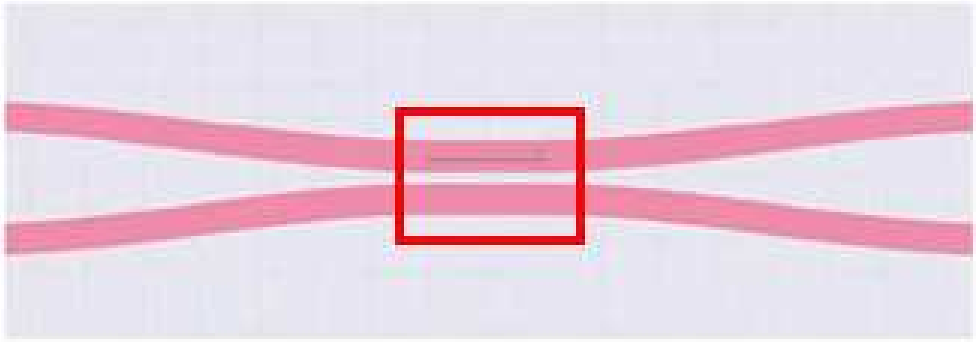

Figure 3.7: The directional coupler

3.3.1 Supermode Analysis

Using COMSOL Multiphysics, a directional coupler made of two rib waveguides with same dimension as previous one, and a coupling gap G_c of 200 nm, was analyzed to calculate numerically the effective indices, n_{eff1} and n_{eff2}, of the two primary eigenmodes of the coupled waveguides at 1550 nm. Fig.3.8 shows the cross-sectional view of the directional coupler used in the simulation, where the core area is marked in blue and the cladding area is the grey region.

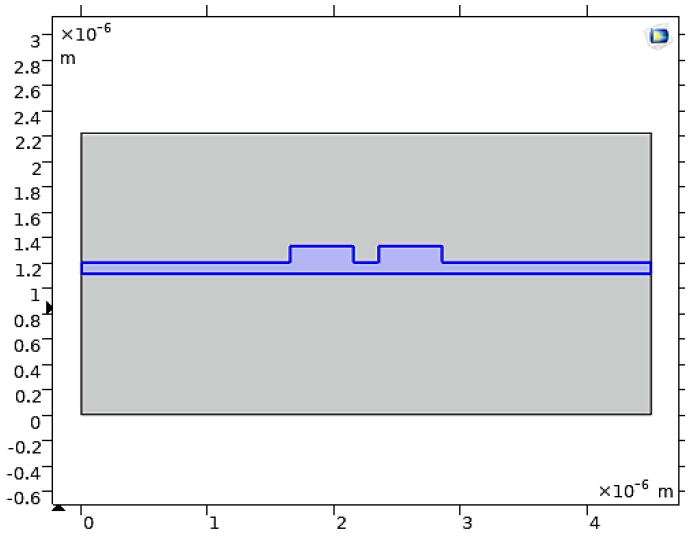

Figure 3.8: Cross-section of the directional coupler used for simulation

Fig. 3.9a shows the modulus of the electric field distribution of the even mode. It can be observed that the field distribution across the waveguides is overlapping and it is evenly distributed inside the two waveguides, this is in conformity with the reference book [111]. The even supermode is as a result of the phase match between the modes in the two waveguides. Fig. 3.9b also shows the modulus of the electric field distribution of the odd mode, where it can be observed that the field distribution in the two waveguides are not overlapping. Odd supermode is as a result of the phase mismatch between the modes in the two waveguides.

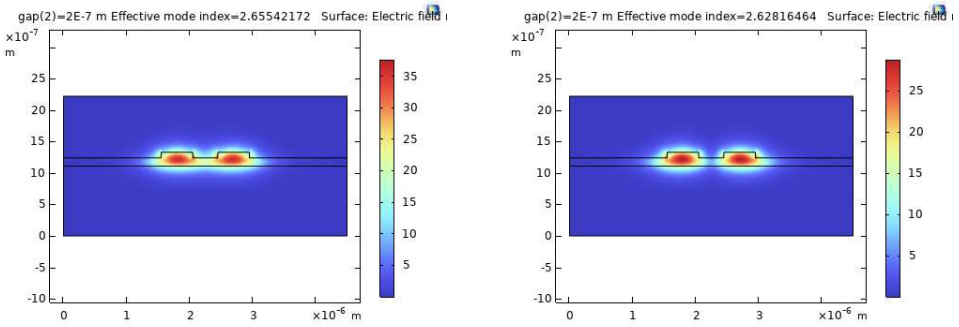

(a) (b)

Figure 3.9: Electric field modulus distribution of (a) even and (b) odd supermode at 1550 nm when the gap between the waveguides is 200 nm

Fig. 3.10 shows the plot of the effective index of even and odd modes as a function of the coupler gap. It reveals that, as the coupler gap increases, the difference between the effective index of the supermodes becomes smaller, indicating that the two waveguides uncouple for larger gap values.

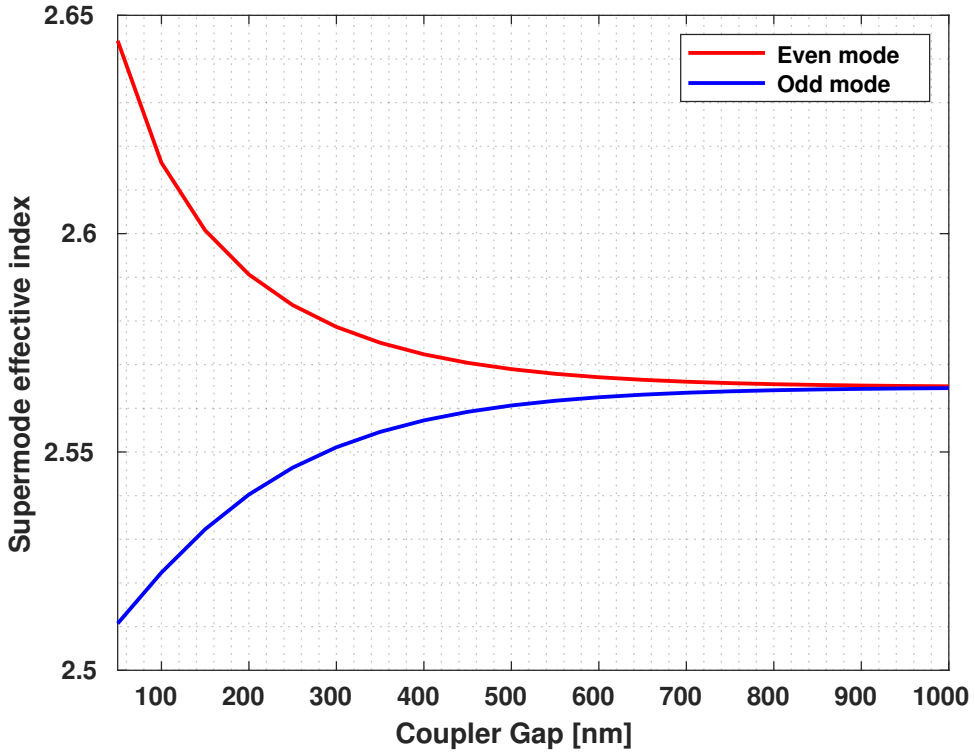

Figure 3.10: Effective index of even and odd mode at 1550 nm as a function of the coupler gap.

Fig. 3.11 also shows the plot of the effective index of even and odd modes as a function of wavelength when the gap width is 200 nm, clearly revealing that effective index value of the even mode is higher than that of the odd mode.

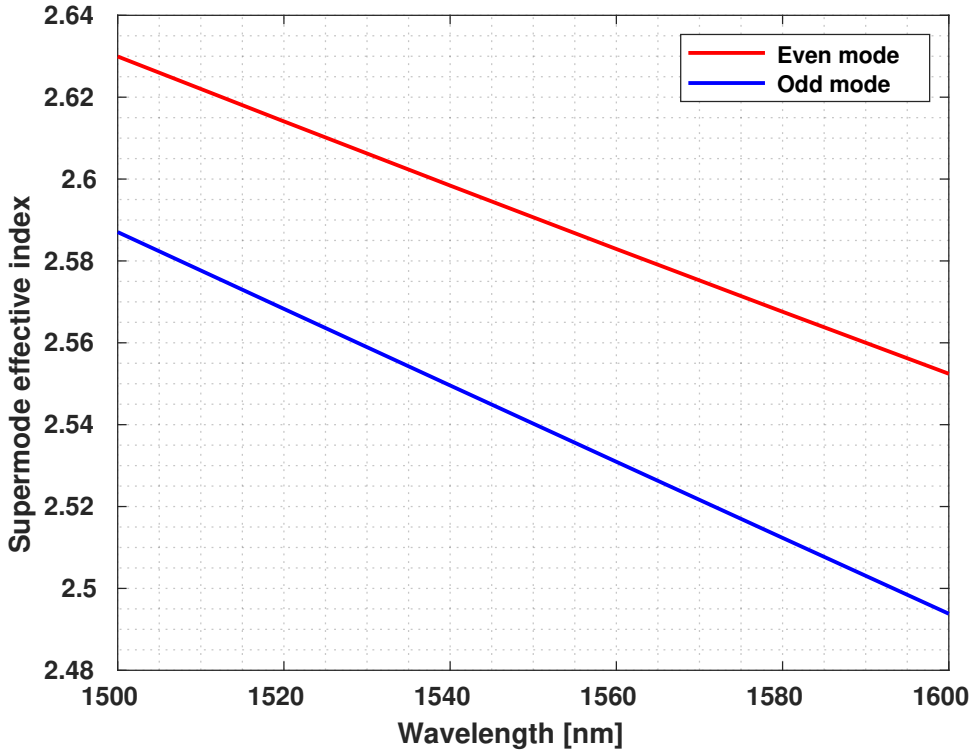

Figure 3.11: Effective index of the even and odd mode as a function of wavelength for a coupler gap of 200 nm.

Based on the two supermodes, the coupling coefficient is given by: $k_c = \frac{\pi \Delta n}{\lambda}$, where $\Delta n = n_{eff1} - n_{eff2}$ [111, 117]. The phase shift experienced by a wave with a propagation constant β, as it travels through a length L is given by; $\phi = \beta L$. As the modes propagate, the field intensity oscillates between the two waveguides. When the modes are in phase, the power is concentrated in the first waveguide. After a phase shift of π between the modes, the power shifts to the second waveguide. This transfer of power occurs over a distance L_x [111]. Assuming that the two modes are propagating with propagation constants $\beta_1 = \frac{2\pi n_{eff1}}{\lambda}$ and $\beta_2 = \frac{2\pi n_{eff2}}{\lambda}$ then $\beta_1 L_x - \beta_2 L_x = \pi$. Hence $L_x = \frac{\lambda}{2\Delta n}$.

Fig. 3.12 represents the behaviour of the cross-over length against wavelength for

different value of the coupler gap. It shows that, as the coupler gap increases, a mode with a certain wavelength needs to travel longer distance before it can be coupled from one waveguide to the other.

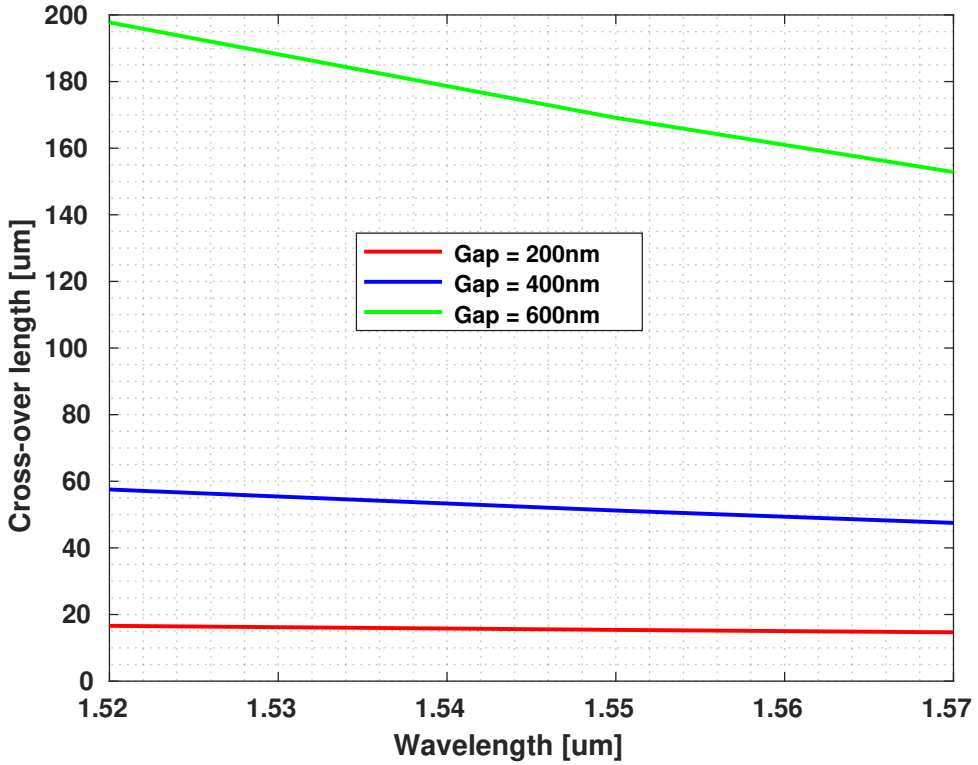

Figure 3.12: The cross-over length as a function of wavelength for three different coupler gap values.

For a 500 x 220 nm waveguide with a slab thickness of 90 nm, a curve-fit of the cross-over length data yields $L_x = 10^{(0.0026084.G_c[nm]+0.657094)}$ [111]. This expresses L_x as a function of the coupler gap. Fig. 3.13 shows the cross-over length as a function of the coupler gap for three different values of the wavelength on a linear scale,while the same parameter is shown in Fig. 3.14 on a logarithmic scale.

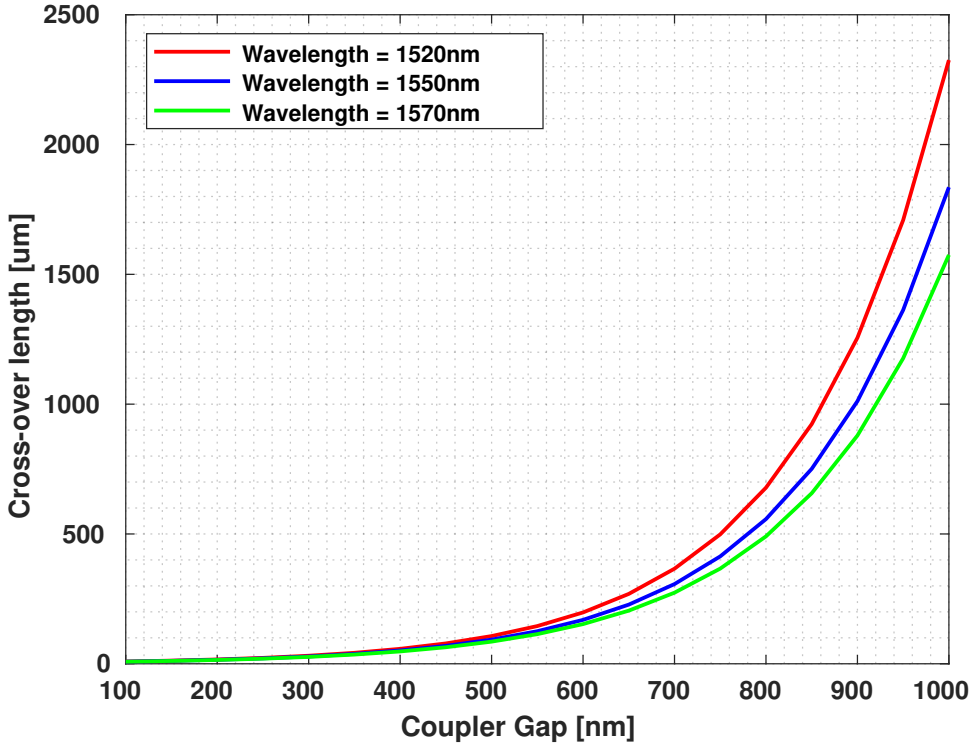

Figure 3.13: The cross-over length as a function of coupler gap for fixed wavelength in linear scale.

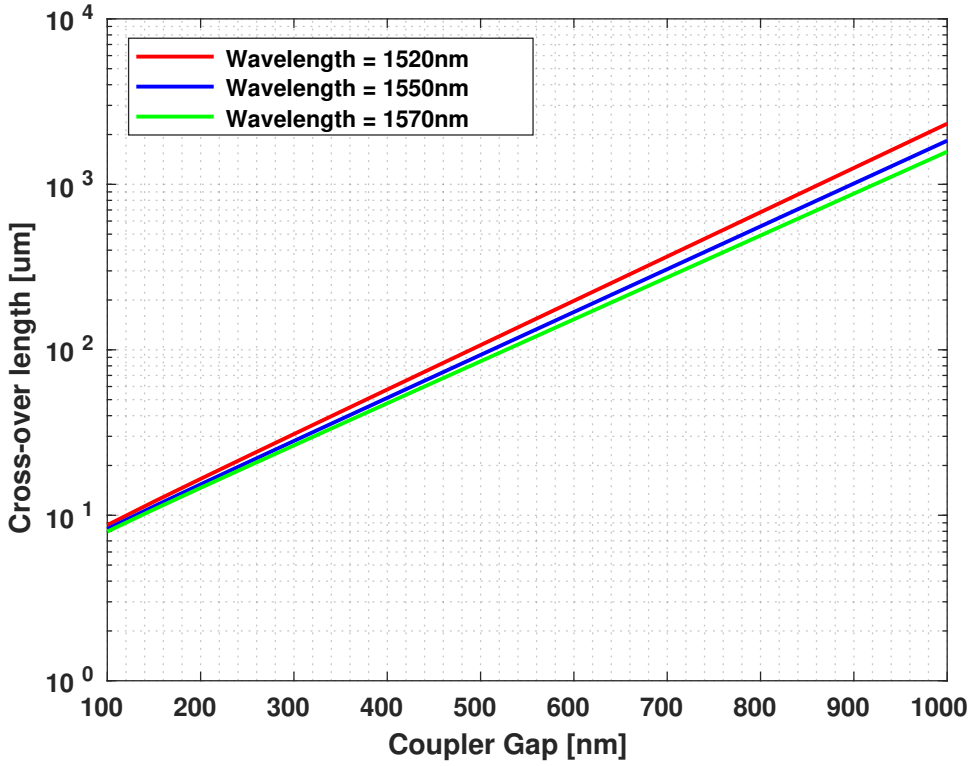

Figure 3.14: The cross-over length as a function of coupler gap for fixed wavelength in logarithmic scale.

3.3.2 Analysis with transfer matrix method

The transfer matrix method (TMM) is a method that can be used for the analysis of the wave propagation [120]. In particular, it is employed to relate the field amplitude of the input waveguide to one of the output waveguides [117, 121]. Fig. 3.15 displays the conceptual view of an optical component having two input and two output ports, where the TMM is used to relate the amplitude of the input waveguide's fundamental modes A_{in} and B_{in} to the output waveguide's fundamental modes A_{out} and B_{out}. T_{11} and T_{22} are called the direct terms because they connect the input to the output of the same waveguide. T_{21} and T_{12} are called the cross terms because they connect the

input of one waveguide to the output of another [117].

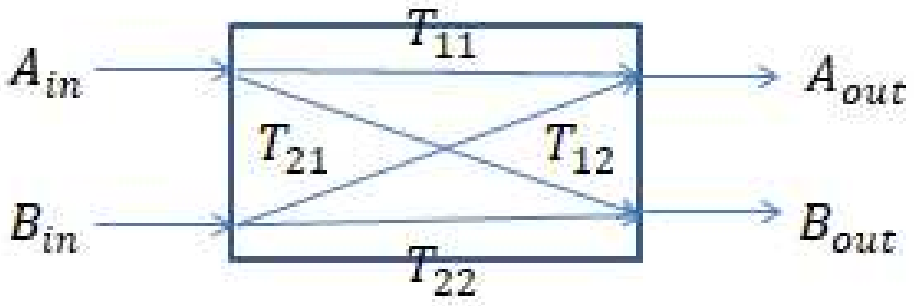

Figure 3.15: Conceptual view of an optical device with two input and two output waveguideS. [117].

Following the derivations from [117], and looking at Fig. 3.15, it is possible to write:

$$\begin{bmatrix} A_{out} \\ B_{out} \end{bmatrix} = \begin{bmatrix} T_{11} & T_{12} \\ T_{21} & T_{22} \end{bmatrix} \begin{bmatrix} A_{in} \\ B_{in} \end{bmatrix}$$

Assuming only one input waveguide is excited, that is $A_{in} = 1$ and $B_{in} = 0$, then $A_{out} = T_{11}A_{in}$ and $B_{out} = T_{21}A_{in}$. With rigorous analysis, the expressions for T_{11} and T_{21} for the directional coupler are $T_{11} = \frac{1}{2}(1+e^{j\Delta\beta L_c})e^{-j\beta_1 L_c}$, and $T_{21} = \frac{1}{2}(1-e^{j\Delta\beta L_c})e^{-j\beta_1 L_c}$, where $\Delta\beta = \beta_1 - \beta_2$ of the two supermodes. Expressions for T_{12} and T_{22} can be obtained in similar manner by exciting the other input waveguide, that is with $B_{in} = 1$ and $A_{in} = 0$. With further assumptions,

$$A_{out} = A_{in}\cos\left(\pi\frac{\Delta n}{\lambda}L_c\right)e^{-j\phi_c},$$

$$B_{out} = -jA_{in}\sin\left(\pi\frac{\Delta n}{\lambda}L_c\right)e^{-j\phi_c},$$

being $\phi_c = \phi_i + \phi_o + \beta_m L_c$, where ϕ_i is the phase shift from the input waveguide, ϕ_o is the phase shift from the output waveguide and $\beta_m = \dfrac{\beta_1+\beta_2}{2}$. In the context of the power contained in the mode propagating through the output waveguide,

$$P_a = |A_{out}|^2 = P_{in}\cos^2\left(\pi\frac{\Delta n}{\lambda}L_c\right),$$

$$P_b = |B_{out}|^2 = P_{in} \sin^2 \left(\pi \frac{\Delta n}{\lambda} L_c \right),$$

where the input power is $P_{in} = |A_{in}|^2$.
When $L_c = \frac{L_x}{2}$, $P_a = |A_{out}|^2 = P_{in} \cos^2 \left(\pi \frac{\Delta n}{\lambda} \frac{\lambda}{2\Delta n} \frac{1}{2} \right) = P_{in} \cos^2 \left(\frac{\pi}{4} \right)$
Similarly, $P_b = |B_{out}|^2 = P_{in} \sin^2 \left(\pi \frac{\Delta n}{\lambda} \frac{\lambda}{2\Delta n} \frac{1}{2} \right) = P_{in} \sin^2 \left(\frac{\pi}{4} \right)$. Hence when $L_c = \frac{L_x}{2}$, $P_a = P_b = \frac{P_{in}}{2}$ and the device behaves as a 3-dB coupler.
In the calculations of the output power for the special case when only one input waveguide is excited, three wavelengths have been considered in the C-band: 1520 nm, 1550 nm and 1570 nm, for three different coupling gaps, that is 200 nm, 400 nm and 600 nm. Fig. 3.16, Fig. 3.17 and Fig. 3.18 show the plots of the output power profiles at the various propagation wavelengths for 200 nm, 400 nm and 600 nm waveguide separations respectively. For each plot, the coupler length to achieve the 3-dB condition is indicated with dash black vertical line and it can be observed that for each gap width, as the propagation wavelength increases, the coupler length required reduces. Table 3.1 shows the recorded coupler lengths from the graph for the various wavelengths and the gap widths.

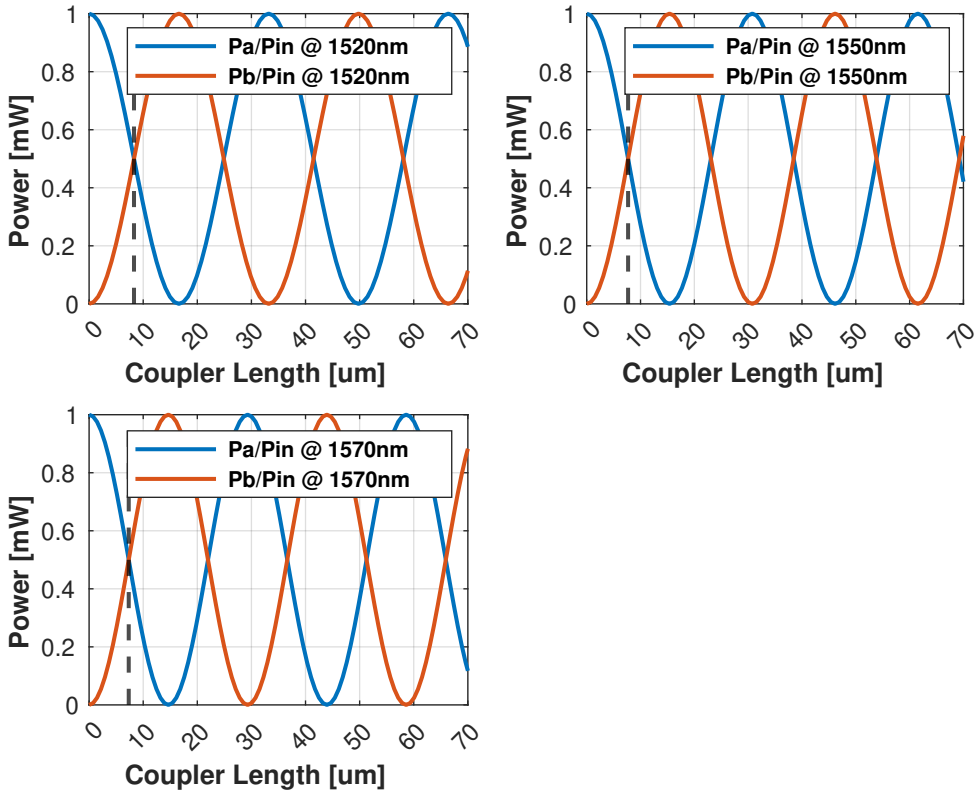

Figure 3.16: Output power profiles for the case when the coupling gap is 200 nm, where the coupler length required for 3-dB condition is marked.

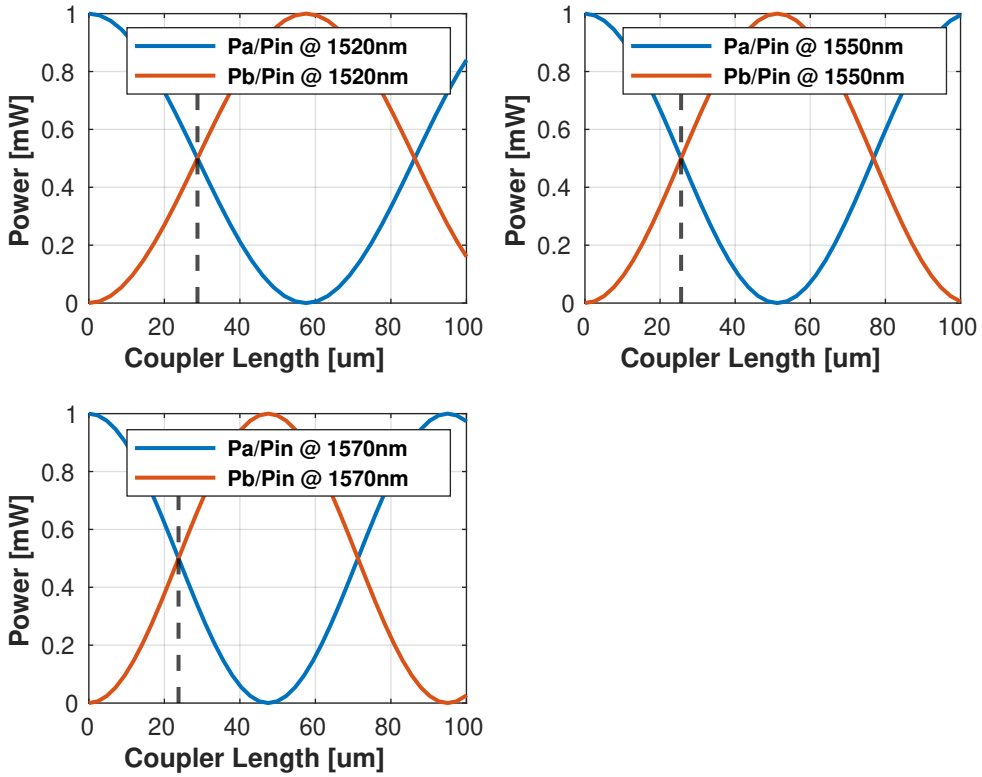

Figure 3.17: Output power profiles for the case when the coupling gap is 400 nm, where the coupler length required for 3-dB condition is marked.

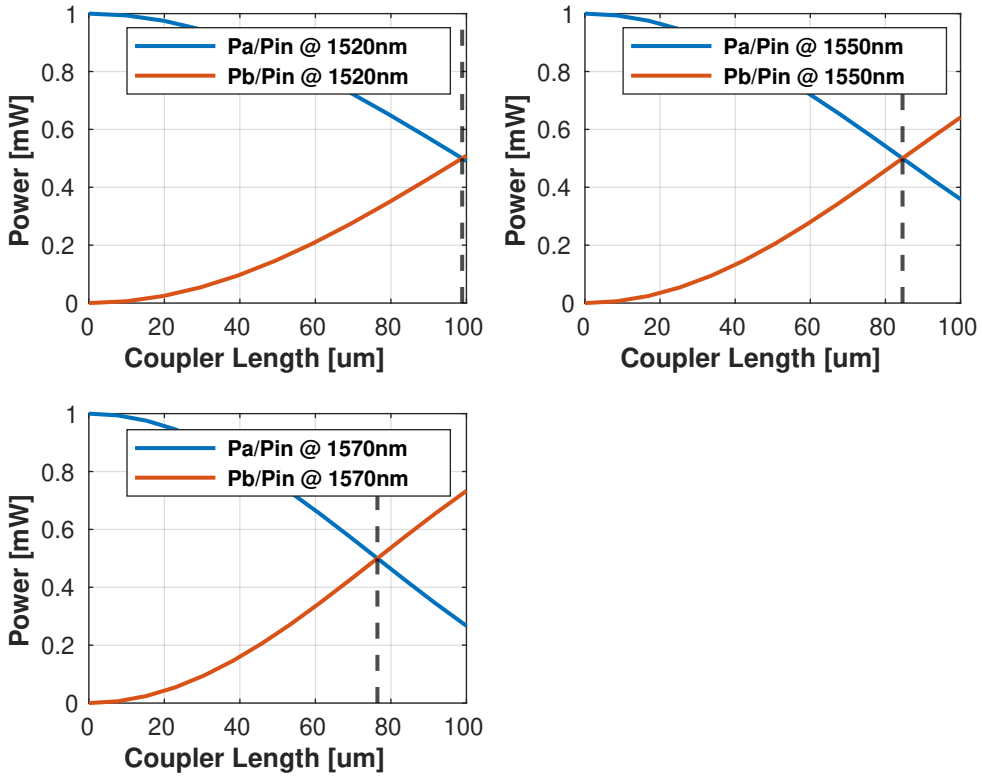

Figure 3.18: Output power profiles for the case when the coupling gap is 600 nm, where the coupler length required for 3-dB condition is marked.

Table 3.1: Coupler length required to achieve 3-dB condition for various propagation wavelengths and gap widths

Gap widths	**1520 nm**	**1550 nm**	**1570 nm**
200 nm	8.30 μm	7.69 μm	7.33 μm
400 nm	28.77 μm	25.61 μm	23.75 μm
600 nm	98.87 μm	84.56 μm	76.42 μm

Conclusions

This thesis has explored the pivotal role of photonic technologies in addressing the demands of next-generation high-speed data applications, emphasizing the connections between physical impairments, photonic device performance, and innovative solutions to overcome these challenges. By integrating experimental and analytical approaches, this work contributes to the advancement of photonic systems capable of meeting the stringent requirements of modern technologies.

Chapter 1 addressed the limitations of electronic analog-to-digital converters in meeting the growing demands of high bandwidth and sampling rates for applications such as autonomous driving, Internet of Things (IoT), online gaming, and other data-intensive technologies. Despite their established role in digital signal processing, EADCs face bottlenecks in sampling rate and bandwidth, necessitating a shift towards photonic ADCs (PADCs). By leveraging the inherent advantages of optical systems, such as higher sampling rates and broader bandwidths, as well as ultra low pulse jitters, PADCs emerged as a viable solution to overcome these constraints. Among the PADCs proposed in literature, spectrally sliced systems, also known as frequency interleaved architectures, were highlighted for their potential to enhance bandwidth. The discussion in chapter 1 focused on a study presented in literature that identified the fundamental performance limits imposed by timing jitter from mode-locked lasers in spectrally-sliced PADCs. By following the calculations in [8], it has been demonstrated how implementing optical slicing mitigates the combined effects of electric and optical jitter, thus improving system performance. These findings underscore the relevance of spectrally sliced PADCs in pushing the boundaries of ADC

performance, particularly in environments characterized by high jitter levels.
The first chapter of this thesis not only emphasized the advantages of PADCs, but also provided a critical perspective on their limitations. The interplay between electric and optical noise sources poses significant challenges, yet the strategic integration of slicing techniques offers a pathway to enhanced performance. The energy per bit consumption of these devices have also been studied by following a model proposed in [10]. The modulator limited energy per sample as a function of sample rate is calculated, which reveals that state of the art bandwidth/voltage trade-off can improve performance. Optical power limited energy per sample in the presence of jitter, as a function of sample rate is also studied and it reveals that energy per sample increases with improved jitter. The optical power limited energy per sample as a function of SNR is also studied, showing that at low SNRs, thermal noise is dominant and at high SNRs, shot noise dominates.
In chapter 2 a novel approach to measuring the dispersion of a device containing chirped Bragg gratings is described. Dispersion, a key physical impairment, affects various aspects of optical system performance, including pulse spreading and timing jitter. The proposed method, which Professor Michael Galili, Dr Peter David Girouard and I formulated during my stay at the Technical University of Denmark, leverages interferometric fringe analysis to provide a rapid, reliable, and accurate means of characterizing dispersion. This represents a significant improvement over established methods, both in terms of speed and precision.
Experimental results obtained using the proposed method were compared with those derived from traditional techniques. While the established methods required over an hour to record data, the proposed one achieved the same objective within five seconds. Moreover, the analytical model developed as part of this work demonstrated excellent agreement with both experimental measurements and design values. This validates the accuracy and reliability of the proposed approach, highlighting its potential for widespread adoption in photonic device characterization. Beyond its immediate application, the analytical framework described in this thesis holds promise for various advanced fields, including optical Fourier transform (OFT), true-time delays for phased-array antennas, optical time lenses for temporal imaging, and ultrafast sig-

nal processing. By enabling a precise and efficient dispersion measurement method, this work supports the development of sophisticated photonic systems tailored to the demands of modern technologies. The second chapter of the thesis also emphasized the broader implications of this work. Accurate dispersion characterization is critical for optimizing device performance in applications ranging from telecommunications to biomedical imaging. By offering a dependable method for predicting dispersion in complex photonic systems, this thesis contributes to the development of high-performance optical devices capable of meeting the precision and reliability demands of next-generation applications.

In chapter 3 I summarized my numerical simulation activities on silicon photonic waveguides and couplers, with an emphasis on their dispersion properties. Through numerical simulations based on the FEM, I explored how waveguide dimensions and operating wavelength influence the dispersion properties in different kinds of waveguides. Results revealed distinct dispersion behaviors for these waveguides, highlighting the importance of design considerations in silicon photonic devices. Simulations described in this chapter provide insights also into the factors that influence the behaviour of directional couplers, showing that FEM is a powerful numerical method for the design of different types of integrated optical devices. The supermode analysis demonstrated how design parameters such as waveguide separation and refractive index contrast influence the behaviour of directional couplers.

In the future directions, the insights gained from this thesis have significant implications for the advancement of photonic technologies. By proposing a method of measuring dispersion that is fast, reliable and accurate, this work provides a foundation for developing high-performance optical systems capable of meeting the demands of modern applications. The proposed methodologies and analytical frameworks not only enhance our understanding of photonic device behavior but also offer practical solutions for overcoming existing limitations in TDM and WDM based networks. This can be realized through the use of the proposed method of measuring dispersion of devices which will be used to implement OFT, to leverage the advantages in both TDM and WDM systems to improve performance. Future research will build upon the findings of this thesis by exploring new avenues for improving photonic device

performance. For instance, refining the analytical model for dispersion measurement to accommodate a broader range of devices and operating conditions could further enhance its applicability. By addressing these challenges, future efforts aim to ensure that photonic systems remain at the forefront of innovation in high-speed data processing and communication.

In the nutshell, this thesis has made significant contributions to the fields of photonic, specifically in the area of dispersion measurement. By integrating theoretical insights with practical methodologies, it provides a comprehensive framework for advancing photonic technologies. As the field of photonics continues to evolve, the findings and methodologies presented in this thesis will serve as a valuable resource for researchers and engineers striving to push the boundaries of optical technology.

Bibliography

[1] Giuseppe Rizzelli. “Advances in Optical Fiber Communications”. In: *Applied Sciences* 12.10 (2022). MDPI, p. 4818.

[2] Rodney S Tucker. “Green optical communications—Part I: Energy limitations in transport”. In: *IEEE Journal of selected topics in quantum electronics* 17.2 (2010). publisher: IEEE, pp. 245–260.

[3] Muhammad A Butt et al. “Strategic Insights into Integrated Photonics: Core Concepts, Practical Deployments, and Future Outlook”. In: *Applied Sciences* 14.14 (2024). publisher: MDPI, p. 6365.

[4] Zhiping Zhou et al. “Lowering the energy consumption in silicon photonic devices and systems”. In: *Photonics Research* 3.5 (2015). publisher: Optica Publishing Group, B28–B46.

[5] Jonathan Klamkin et al. “Indium phosphide photonic integrated circuits: Technology and applications”. In: *2018 IEEE BiCMOS and Compound Semiconductor Integrated Circuits and Technology Symposium (BCICTS)*. IEEE. 2018, pp. 8–13.

[6] Tushar Gaur et al. “Comparative analysis of lithium niobate and barium titanate material platforms for implementing electro-optically tunable general-purpose photonic processors”. In: *Optical Materials Express* 13.11 (2023). publisher: Optica Publishing Group, pp. 3217–3231.

[7] Erik Agrell et al. “Roadmap on optical communications”. In: *Journal of Optics* 26.9 (2024). IOP Publishing, p. 093001.

[8] Andrea Zazzi et al. “Fundamental limitations of spectrally-sliced optically enabled data converters arising from MLL timing jitter”. In: *Optics Express* 28.13 (2020). Optica Publishing Group, pp. 18790–18813.

[9] Ezra Ip et al. “Coherent detection in optical fiber systems”. In: *Optics Express* 16.2 (2008). Optica Publishing Group, pp. 753–791.

[10] Callum Deakin et al. “Power dissipation bounds for photonic analog to digital converters”. In: *2023 Optical Fiber Communication Conference (OFC)*. San Diego, CA, USA: Optica Publishing Group, 2023, pp. 1–3. DOI: 10.1364/OFC.2023.M1J.2.

[11] Govind P Agrawal. *Fiber-optic communication systems*. John Wiley & Sons, 2012.

[12] Callum Deakin et al. “Energy Efficiency Bounds for Photonic Analog to Digital Converters”. In: *Journal of Lightwave Technology* 42.6 (2024). Optica Publishing Group, pp. 1819–1828. DOI: 10.1109/JLT.2023.3328317.

[13] Robert H Walden. “Analog-to-digital converter survey and analysis”. In: *IEEE Journal on selected areas in communications* 17.4 (1999). IEEE, pp. 539–550.

[14] Takao Waho. *Introduction to Analog-to-Digital Converters*. 1st. River Publishers, 2019. DOI: 10.1201/9781003338680. URL: https://doi.org/10.1201/9781003338680.

[15] Jyoti et al. “Different Analog to Digital Converters Architectures”. In: *International Journal of Innovative Technology and Exploring Engineering* 9.4 (2020). Blue Eyes Intelligence Engineering and Sciences Engineering and Sciences Publication (BEIESP), pp. 1256–1263. DOI: 10.35940/ijitee.d1641.029420.

[16] Emiel Por et al. *Nyquist–Shannon sampling theorem*. Lecture Notes AOT 2019, Exercise 13. Leiden University, 2019, pp. 1–2. URL: https://home.strw.leidenuniv.nl/~por/AOT2019/docs/AOT_2019_Ex13_NyquistTheorem.pdf.

[17] George C Valley. "Photonic analog-to-digital converters: A tutorial". In: *2009 Conference on Optical Fiber Communication*. IEEE. Optica Publishing Group, 2009, pp. 1–48.

[18] A. Bruce Carlson. *Communication Systems: An Introduction to Signals and Noise in Electrical Communication*. 5th ed. Previous editions published in 2002, 1986, and 1975. New York, NY: McGraw-Hill, 2010.

[19] Mary Y Lanzerotti et al. "Quantization error for weak RF simultaneous signal estimation". In: *EURASIP Journal on Advances in Signal Processing* 2023.1 (2023). Springer, p. 89.

[20] Jiann-Jong Chen et al. "A low-noise fast-transient-response delta-sigma-modulation buck converter with hysteresis-voltage-controlled techniques". In: *IEEE Access* 10 (2022). IEEE, pp. 63063–63072.

[21] B Widrow et al. "Spectrum of quantization noise and conditions of whiteness". In: *Quantization Noise: Roundoff Error in Digital Computation, Signal Processing, Control, and Communications* 539 (2008). Cambridge University Press, p. 560.

[22] V. Lalitha et al. "A Review of Manchester, Miller, and FM0 Encoding Techniques". In: *Smart Computing. Review.* 4.6 (2014), pp. 481–490. URL: https://api.semanticscholar.org/CorpusID:9811618.

[23] Piero Angeletti et al. "Evolution of analog to digital conversion technology for wideband space applications". In: *Proceedings of the 23rd AIAA International Communications Satellite Systems Conference (ICSSC 2005), Rome, Italy*. 2005, pp. 25–28.

[24] Robert H Walden. "Analog-to-digital converter technology comparison". In: *Proceedings of 1994 IEEE GaAs IC Symposium*. IEEE. 1994, pp. 217–219.

[25] Bin Le et al. "Analog-to-digital converters". In: *IEEE Signal Processing Magazine* 22.6 (2005). IEEE, pp. 69–77.

[26] Benedikt Geiger et al. “Record 2.29 Tb/s GS-256QAM transmission using a single receiver”. In: *European Conference and Exhibition on Optical Communication*. Optica Publishing Group. 2022, We3D–3.

[27] Yongsang Yoo et al. “Readout circuits for capacitive sensors”. In: *Micromachines* 12.8 (2021). MDPI, p. 960.

[28] Hemlata Dalmia et al. “Analog to digital converters (ADC): A literature review”. In: *E3S Web of Conferences*. Vol. 184. EDP Sciences. 2020, p. 01025.

[29] Robert H Walden. “Analog-to-Digital Conversion in the Early Twenty-First Century”. In: *Wiley Encyclopedia of Computer Science and Engineering* (2007). Wiley Online Library, pp. 1–14.

[30] Tomislav Drenski et al. “ADC & DAC-technology trends and steps to overcome current limitations”. In: *Optical Fiber Communication Conference*. Optica Publishing Group. 2018, pp. M2C–1.

[31] Younus Mandalawi et al. “Analysis of bandwidth reduction and resolution improvement for photonics-assisted ADC”. In: *Journal of Lightwave Technology* 41.19 (2023). IEEE, pp. 6225–6234.

[32] Ian F Akyildiz et al. “Terahertz band communication: An old problem revisited and research directions for the next decade”. In: *IEEE Transactions on Communications* 70.6 (2022). IEEE, pp. 4250–4285.

[33] Fernando P Guiomar et al. “Coherent free-space optical communications: Opportunities and challenges”. In: *Journal of Lightwave Technology* 40.10 (2022). IEEE, pp. 3173–3186.

[34] Wei Shi et al. “Scaling capacity of fiber-optic transmission systems via silicon photonics”. In: *Nanophotonics* 9.16 (2020). De Gruyter, pp. 4629–4663.

[35] Christian Schmidt et al. “Data converter interleaving: Current trends and future perspectives”. In: *IEEE Communications Magazine* 58.5 (2020). IEEE, pp. 19–25.

[36] Siddharth Varughese et al. “Frequency dependent ENoB requirements for 400G/600G/800G optical links”. In: *Journal of Lightwave Technology* 38.18 (2020). IEEE, pp. 5008–5016.

[37] Siddharth Varughese et al. “Frequency dependent ENoB requirements for M-QAM optical links: An analysis using an improved digital to analog converter model”. In: *Journal of Lightwave Technology* 36.18 (2018). IEEE, pp. 4082–4089.

[38] Donghe Tu et al. “Photonic sampled and quantized analog-to-digital converters on thin-film lithium niobate platform”. In: *Optics Express* 31.2 (2023). Optica Publishing Group, pp. 1931–1942.

[39] Anatol Khilo et al. “Photonic ADC: overcoming the bottleneck of electronic jitter”. In: *Optics Express* 20.4 (2012). Optica Publishing Group, pp. 4454–4469.

[40] Karim Abbas. *Handbook of Digital CMOS Technology, Circuits, and Systems*. Springer Nature, 2020.

[41] John Heck et al. “CMOS-compatible fabrication, micromachining, and bonding strategies for silicon photonics”. In: *Advanced Fabrication Technologies for Micro/Nano Optics and Photonics IV*. Vol. 7927. SPIE. 2011, pp. 167–173.

[42] S Wang et al. “CMOS-compatible photonic integrated circuits on thin-film ScAlN”. In: *APL Photonics* 9.6 (2024). AIP Publishing.

[43] Chunle Xiong et al. “CMOS-compatible photonic devices for single-photon generation”. In: *Nanophotonics* 5.3 (2016). De Gruyter, pp. 427–439.

[44] George C Valley. “Photonic analog-to-digital converters”. In: *Optics Express* 15.5 (2007). Optica Publishing Group, pp. 1955–1982.

[45] Sheel Aditya et al. “Photonic analog-to-digital conversion and photonic microwave signal generation”. PhD thesis. Nanyang Technological University, Singapore, 2012.

[46] Jinpeng Song et al. “Time-and frequency-interleaving: Distinctions and connections”. In: *IEEE Transactions on Signal Processing* 69 (2021). IEEE, pp. 2555–2568.

[47] Scott R Velazquez et al. “Design of hybrid filter banks for analog/digital conversion”. In: *IEEE transactions on signal processing* 46.4 (1998). IEEE, pp. 956–967.

[48] Thomas Moon et al. “Wideband sparse signal acquisition with dual-rate time-interleaved undersampling hardware and multicoset signal reconstruction algorithms”. In: *IEEE Transactions on Signal Processing* 63.24 (2015). IEEE, pp. 6486–6497.

[49] Jinpeng Song et al. “Digital estimation and compensation of analog errors in frequency-interleaved ADCs”. In: *Journal of Circuits, Systems and Computers* 28.08 (2019). World Scientific, p. 1950134.

[50] Gabriele Manganaro et al. “Interleaving ADCs: Unraveling the Mysteries”. In: *Analog Dialogue* 49.7 (2015). Analog Devices, Inc.

[51] Andrea Zazzi et al. “Wideband SiN pulse interleaver for optically-enabled analog-to-digital conversion: a device-to-system analysis with cyclic equalization”. In: *Optics Express* 30.3 (2022). Optica Publishing Group, pp. 4444–4466.

[52] Dengyang Fang et al. “320 GHz analog-to-digital converter exploiting Kerr soliton combs and photonic-electronic spectral stitching”. In: *2021 European Conference on Optical Communication (ECOC)*. IEEE. 2021, pp. 1–4.

[53] Andrea Zazzi et al. “Optically enabled ADCs and application to optical communications”. In: *IEEE Open Journal of the Solid-State Circuits Society* 1 (2021). IEEE, pp. 209–221.

[54] Hayk Gevorgyan et al. “Silicon photonic time-wavelength pulse interleaver for photonic analog-to-digital converters”. In: *Optics Express* 24.12 (2016). Optica Publishing Group, pp. 13489–13499.

[55] Boris Murmann. “A/D converter trends: Power dissipation, scaling and digitally assisted architectures”. In: *2008 IEEE Custom Integrated Circuits Conference*. IEEE. 2008, pp. 105–112.

[56] Behzad Razavi. “Design considerations for interleaved ADCs”. In: *IEEE Journal of Solid-State Circuits* 48.8 (2013). IEEE, pp. 1806–1817.

[57] Callum Deakin et al. “Frequency interleaving dual comb photonic ADC with 7 bits ENOB up to 40 GHz”. In: *2022 Conference on Lasers and Electro-Optics (CLEO)*. IEEE. 2022, pp. 1–2.

[58] Shalabh Gupta et al. “Time-warp correction and calibration in photonic time-stretch analog-to-digital converter”. In: *Optics Letters* 33.22 (2008). Optica Publishing Group, pp. 2674–2676.

[59] Rajesh M Hegde et al. “Significance of the modified group delay feature in speech recognition”. In: *IEEE Transactions on Audio, Speech, and Language Processing* 15.1 (2006). IEEE, pp. 190–202.

[60] Hema A Murthy et al. “Group delay functions and its applications in speech technology”. In: *Sadhana* 36 (2011). Springer, pp. 745–782.

[61] B Yegnanarayana et al. “Significance of group delay functions in signal reconstruction from spectral magnitude or phase”. In: *IEEE Transactions on Acoustics, Speech, and Signal Processing* 32.3 (1984). IEEE, pp. 610–623.

[62] John F Ready. *Industrial applications of lasers*. Elsevier, 1997.

[63] Bruno Costa et al. “Phase shift technique for the measurement of chromatic dispersion in optical fibers using LED’s”. In: *IEEE Transactions on Microwave Theory and Techniques* 30.10 (1982). IEEE, pp. 1497–1503.

[64] Kyle RH Bottrill et al. “Spectral Difference Interferometry for the Characterization of Optical Media”. In: *Laser & Photonics Reviews* 13.10 (2019). Wiley Online Library, p. 1900007.

[65] Chi Shing Cheung. *An investigation of chirped fibre Bragg gratings Fabry-pérot interferometer for sensing applications*. Cranfield University, 2005.

[66] Andreas Othonos et al. “Fibre bragg gratings”. In: *Wavelength Filters in Fibre Optics* (2006). Springer, pp. 189–269.

[67] Fouad El-Diasty et al. “Analysis of fiber Bragg gratings by a side-diffraction interference technique”. In: *Applied Optics* 40.6 (2001). Optica Publishing Group, pp. 890–896.

[68] J Čtyrokỳ et al. “Bragg waveguide grating as a 1D photonic band gap structure: COST 268 modelling task”. In: *Optical and Quantum Electronics* 34 (2002). Springer, pp. 455–470.

[69] Dario Gerace et al. “Wide-band transmittance of one-dimensional photonic crystals carved in Si3N4/ SiO2 channel waveguides”. In: *Applied Physics Letters* 87.21 (2005). AIP Publishing.

[70] John Lawall et al. “Michelson interferometry with 10 pm accuracy”. In: *Review of Scientific Instruments* 71.7 (2000). American Institute of Physics, pp. 2669–2676.

[71] Masroor Ikram et al. “Michelson interferometer for precision angle measurement”. In: *Applied Optics* 38.1 (1999). Optica Publishing Group, pp. 113–120.

[72] Mostafa Khalil et al. “Electrically reconfigurable waveguide Bragg grating filters”. In: *Optics Express* 30.22 (2022). Optica Publishing Group, pp. 39643–39651.

[73] Hamed Saghaei et al. “Sinusoidal and rectangular Bragg grating filters: design, fabrication, and comparative analysis”. In: *Journal of Applied Physics* 132.6 (2022). AIP Publishing.

[74] M Casalboni et al. “Bragg grating optical filters by UV nanoimprinting”. In: *Journal of Nanomaterials* 2012.1 (2012). Wiley Online Library, p. 186429.

[75] M Johri et al. “Photonic band gap materials: Technology, applications and challenges”. In: *Current Science* (2007). JSTOR, pp. 1361–1365.

[76] Muhammad A Butt et al. “Advances in waveguide Bragg grating structures, platforms, and applications: an up-to-date appraisal”. In: *Biosensors* 12.7 (2022). MDPI, p. 497.

[77] Peter GR Smith et al. “UV written waveguide devices—Bragg gratings and Applications in Sensors”. In: *AIP Conference Proceedings*. Vol. 1217. 1. American Institute of Physics. 2010, pp. 153–158.

[78] Zhenyu Zhang et al. “Polymer Waveguide Sensor Based on Evanescent Bragg Grating for Lab-on-a-Chip Applications”. In: *Sensors* 24.4 (2024). MDPI, p. 1234.

[79] Turan Erdogan. “Fiber grating spectra”. In: *Journal of lightwave technology* 15.8 (1997). IEEE, pp. 1277–1294.

[80] Qingtao Chen et al. “Bragg gratings with novel waveguide models fabricated in bulk glass via fs-laser writing and their slow-light effects”. In: *Optics Express* 32.1 (2023). Optica Publishing Group, pp. 188–204.

[81] Turan Erdogan. *The grating equation*. Tech. rep. Plymouth Grating Laboratory. 5 Commerce Way, Carver, MA 02330, 2022. URL: `https://plymouthgrating.com`.

[82] Evgeny Popov. *GratinGs: theory and numeric applications*. Institut Fresnel, 2012.

[83] Hezhuang Liu et al. “Exploring the efficacy of subwavelength gratings as short-wavelength infrared filters”. In: *Discover Nano* 19.1 (2024). Springer, p. 104.

[84] Junying Wang et al. “Line by line inscribed small period long period grating for wide range refractive index sensing”. In: *Optics Communications* 508 (2022). Elsevier, p. 127821.

[85] José Chesnoy. *Undersea Fiber Communication Systems*. 2nd ed. Cambridge, MA: Academic Press, 2015. ISBN: 978-0-12-804269-4.

[86] James F Brennan III. “Broadband fiber Bragg gratings for dispersion management”. In: *Journal of Optical and Fiber Communications Reports* 2.5 (2005). Springer, pp. 397–434.

[87] Yikai Su et al. “Silicon photonic platform for passive waveguide devices: materials, fabrication, and applications”. In: *Advanced Materials Technologies* 5.8 (2020). Wiley Online Library, p. 1901153.

[88] Roel Baets et al. “Silicon Photonics: silicon nitride versus silicon-on-insulator”. In: *Optical fiber communication conference*. Optica Publishing Group. 2016, Th3J–1.

[89] Muhammad A. Butt. “Integrated Optics: Platforms and Fabrication Methods”. In: *Encyclopedia* 3.3 (2023), pp. 824–838. ISSN: 2673-8392. DOI: 10.3390/encyclopedia3030059. URL: https://www.mdpi.com/2673-8392/3/3/59.

[90] Tai Tsuchizawa et al. “Si photonics platform and its fabrication”. In: *The 5th International Symposium on Advanced Science and Technology of Silicon Materials (JSPS Si Symposium)*. 2008.

[91] Mustafa Hammood et al. “Emulation of deep-ultraviolet lithography using rapid-prototyping, electron-beam lithography for silicon photonics design”. In: *Optics Letters* 48.3 (2023). Optica Publishing Group, pp. 582–585.

[92] Arsenty Kaganskiy et al. “Advanced in-situ electron-beam lithography for deterministic nanophotonic device processing”. In: *Review of Scientific Instruments* 86.7 (2015). AIP Publishing.

[93] Goran Z Mashanovich et al. “Silicon photonic waveguides and devices for near-and mid-IR applications”. In: *IEEE Journal of Selected Topics in Quantum Electronics* 21.4 (2014). IEEE, pp. 407–418.

[94] Johannes Milvich et al. “Surface sensing with integrated optical waveguides: a design guideline”. In: *Optics Express* 26.16 (2018). Optica Publishing Group, pp. 19885–19906.

[95] Xingcun Colin Tong Ph. D et al. “Characterization methodologies of optical waveguides”. In: *Advanced Materials for Integrated Optical Waveguides* (2014). Springer, pp. 53–102.

[96] Jayson Koh et al. “Silicon-on-insulator (SOI) technology–pushing the limits of CMOS”. In: *Electronics Technical–EE Publishers* (2007), pp. 54–56.

[97] Ching-Te Chuang et al. “SOI for digital CMOS VLSI: Design considerations and advances”. In: *Proceedings of the IEEE* 86.4 (1998). IEEE, pp. 689–720.

[98] Thorsten Lill et al. “The cutting edge of plasma etching”. In: *Science* 319.5866 (2008). American Association for the Advancement of Science, pp. 1050–1051.

[99] Shoji Akiyama. “High index contrast platform for silicon photonics”. PhD thesis. Massachusetts Institute of Technology, 2004.

[100] Lars Emil Gutt. “Integrated Optical Time Lenses for Passive Optical Networks for Generation of On-Chip Optical Fourier Transforms”. Technical University of Denmark. PhD thesis. Denmark: DTU Electro, Department of Electrical and Photonics Engineering, 2023.

[101] Otto Schwelb. “Transmission, group delay, and dispersion in single-ring optical resonators and add/drop filters-a tutorial overview”. In: *Journal of Lightwave Technology* 22.5 (2004). IEEE, p. 1380.

[102] Ronald W Schafer. “What is a savitzky-golay filter?[lecture notes]”. In: *IEEE Signal processing magazine* 28.4 (2011). IEEE, pp. 111–117.

[103] OV Belai et al. “Group delay in Bragg grating with linear chirp”. In: *Optics communications* 266.2 (2006). Elsevier, pp. 512–520.

[104] Michael Sumetsky et al. “Theory of group delay ripple generated by chirped fiber gratings”. In: *Optics Express* 10.7 (2002). Optica Publishing Group, pp. 332–340.

[105] Yu Sun et al. “Large group delay in silicon-on-insulator chirped spiral Bragg grating waveguide”. In: *IEEE Photonics Journal* 13.5 (2021). IEEE, pp. 1–5.

[106] Raman Kashyap. *Fiber Bragg Gratings*. 2nd ed. Boston: Academic Press, 2009. ISBN: 9780123725790.

[107] Mohamed B. El-Mashade et al. "Analysis of Weak and Strong Fiber Bragg Grating". In: *Current Journal of Applied Science and Technology* 10.6 (2015), pp. 1–17. DOI: 10.9734/BJAST/2015/18898. URL: https://doi.org/10.9734/BJAST/2015/18898.

[108] Olesya Bondarenko et al. "Design of compact IIIV/Si distributed feedback lasers". In: *2013 IEEE Photonics Conference*. IEEE. 2013, pp. 157–158.

[109] Finisar. *WaveShaper 4000S Multiport Optical Processor*. https://www.xsoptix.com/data/finisar/ds_fnsr_instr_WaveShaper_4000S.pdf. Accessed: 2024-12-14.

[110] Bahaa EA Saleh et al. *Fundamentals of photonics*. john Wiley & sons, 2019.

[111] Lukas Chrostowski et al. *Silicon photonics design: from devices to systems*. Cambridge University Press, 2015.

[112] L Vivien et al. "Comparison between strip and rib SOI microwaveguides for intra-chip light distribution". In: *Optical materials* 27.5 (2005). Elsevier, pp. 756–762.

[113] Goëry Genty et al. *Supercontinuum generation in microstructured fibers and novel optical measurement techniques*. Helsinki University of Technology, 2004.

[114] Nazirah Mohd Razali et al. "Simulation of Self-Image Interference in Single Mode-No-Core-Single Mode Fiber with COMSOL Multiphysics®". In: *Journal of Physics: Conference Series*. Vol. 2411. 1. IOP Publishing. 2022, p. 012019.

[115] Graham T Reed et al. *Silicon photonics: an introduction*. John Wiley & Sons, 2004.

[116] Zhi-Yong Wang et al. "Evanescent Fields inside a Cut-off Waveguide as Near Fields". In: *Optics and Photonics Journal* 3.2 (2013). Scientific Research Publishing, pp. 192–196.

[117] Stefano Selleri et al. *Componenti ottici e fotonici*. Progetto Leonardo-Esculapio, 2012.

[118] Fabio Turri et al. "Wavelength dependence of a vertically coupled resonator-waveguide system". In: *Journal of Lightwave Technology* 34.23 (2016). IEEE, pp. 5385–5390.

[119] Alessandro Tuniz et al. "Coupled mode theory for plasmonic couplers". In: *Applied Physics Reviews* 11.2 (2024). AIP Publishing.

[120] Wei Li. "Generalized free wave transfer matrix method for solving the Schrödinger equation with an arbitrary potential profile". In: *IEEE journal of quantum electronics* 46.6 (2010). IEEE, pp. 970–975.

[121] Pilar Castillo-Tapia. "The Multimodal Transfer Matrix Method: And its application to higher-symmetric periodic structures". PhD thesis. KTH Royal Institute of Technology, 2022.

Acknowledgement

First and foremost, I would like to express my deepest gratitude to my supervisor, Professor Federica Poli, at the University of Parma, Italy, for her unwavering support, guidance, and encouragement throughout my PhD journey. Her expertise and insight have been invaluable in shaping this thesis and advancing my research. I am profoundly grateful to the Nokia Research Group in Vimercate, Italy, for the opportunity to collaborate and research on photonic ADCs. My heartfelt thanks to Paola Galli and Christian De Vita for their mentorship, particularly in guiding me through an extensive literature review and helping me delve deeply into the critical impact of timing jitter on spectrally sliced photonic ADCs. Their expertise and feedback were instrumental in refining my understanding of the field. I also extend my sincere appreciation to Professor Michael Galili, Dr. Peter David Girouard, and Lars Emil Gutt at the Technical University of Denmark, for their remarkable support during my internship. The hands-on experience in their laboratory, conducting measurements and analyzing the reflected spectrum to calculate device dispersion, was a pivotal moment in my PhD work. Their guidance and collaboration enriched my research and made this journey immensely rewarding. Finally, I am thankful to my colleagues, family, and friends, who have provided moral support and encouragement throughout this academic endeavor. This work would not have been possible without the collective contributions and support of these extraordinary individuals and institutions. Thank you all for helping me to achieve this milestone.

La borsa di dottorato è stata cofinanziata con risorse del
Programma Operativo Nazionale Ricerca e Innovazione 2014-2020, risorse FSE REACT-EU
Azione IV.4 “Dottorati e contratti di ricerca su tematiche dell’innovazione”
e Azione IV.5 “Dottorati su tematiche Green”